EXPERIMENTAL CHARACTERIZATION OF CRYSTALLIZATION FOULING IN LIQUID-TO-AIR MEMBRANE ENERGY EXCHANGERS

A Thesis Submitted to the College of

Graduate and Postdoctoral Studies

In Partial Fulfillment of the Requirements

For the Degree of Doctor of Philosophy

In the Department of Mechanical Engineering

University of Saskatchewan

Saskatoon

By

OLUFADE, Adesola Oluwasijibomi

PERMISSION TO USE

In presenting this thesis in partial fulfillment of the requirements for a Postgraduate degree from the University of Saskatchewan, I agree that the Libraries of this University may make it freely available for inspection. I further agree that permission for copying of this thesis in any manner, in whole or in part, for scholarly purposes may be granted by the professor or professors who supervised my thesis work or, in their absence, by the Head of the Department or the Dean of the College in which my thesis work was done. It is understood that any copying or publication or use of this thesis or parts thereof for financial gain shall not be allowed without my written permission. It is also understood that due recognition shall be given to me and to the University of Saskatchewan in any scholarly use which may be made of any material in my thesis.

Requests for permission to copy or to make other uses of materials in this thesis in whole or part should be addressed to:

Head of the Department of Mechanical Engineering
University of Saskatchewan
57 Campus Dr
Saskatoon, Saskatchewan S7N 5A9 Canada

OR

Dean
College of Graduate and Postdoctoral Studies
University of Saskatchewan
116 Thorvaldson Building, 110 Science Place
Saskatoon, Saskatchewan S7N 5C9 Canada

ABSTRACT

Liquid-to-air membrane energy exchangers (LAMEEs) are a recent development with potential for energy savings in heating, ventilating and air-conditioning (HVAC) applications. Unlike conventional heat exchangers that transfer only heat using plates or tubes, LAMEEs use semi-permeable membranes to transfer both heat and moisture between liquid desiccant and air streams, while preventing cross-contamination between the fluids. However, the porous membranes used in LAMEEs are prone to crystallization fouling from liquid desiccants, and this may compromise the performance of LAMEEs.

The research reported in this thesis aims to experimentally characterize crystallization fouling in LAMEEs. Experimental tests are performed to dehydrate $MgCl_2$(aq) solution using two types of membranes. The objectives of the research are to (i) develop and calibrate indirect and non-invasive methods to detect the onset of crystallization fouling in a LAMEE, (ii) identify operating conditions that result in crystallization fouling in LAMEEs, and (iii) identify the evolution of crystallization fouling in membranes.

The objectives are met by using non-invasive and invasive methods. The non-invasive methods consist of indirect and direct methods. Three indirect and non-invasive methods are developed to detect fouling by analyzing two measured parameters (moisture transfer flux and resistance). One direct and non-invasive method is used to directly observe the onset of crystallization fouling in the LAMEE. The invasive methods consist of optical microscopy and scanning electron microscopy which are used to characterize the morphology of deposits on membranes, and energy dispersive X-ray spectroscopy which is used to analyze the composition of the deposits.

The direct and non-invasive method detects the start of fouling earlier than the three indirect and non-invasive methods by a factor of three to eight, and is used to calibrate and thereby augment the sensitivity of the indirect and non-invasive methods. Sensitivity studies indicate that crystallization fouling in the LAMEE is dependent on both the concentration of the desiccant solution and the relative humidity of air. Furthermore, the results show that reducing the moisture transfer rate through the membrane can minimize crystallization fouling in the LAMEE. Finally, the evolution and mechanisms of crystallization fouling in membranes are delineated.

ACKNOWLEDGMENTS

I appreciate the indefatigable patience, guidance, and exceptional leadership of my Supervisor, Prof. C. J. Simonson, towards my professional development and accomplishment of this thesis.

I sincerely appreciate the support and constructive feedback of the committee members: Prof. R. Evitts, Prof. D. Sumner and Prof. D. Torvi. I thank Prof. Besant for his advice and inspiration regarding my research and the pursuit of leading-edge scientific advancements.

I am grateful for the technical support of the departmental assistants in the Department of Mechanical Engineering: Mr. S. Reinink, Dr. M. Fauchoux, and Mr. N. Zhao. The technical assistance of Dr. G. Liu (Department of Biology Core Microscopy Laboratory), Dr. E. Kawamura (Western College of Veterinary Medicine Image Centre), and Dr. X. Wang (Advanced Materials and Renewable Energy Laboratory) is also acknowledged.

Colleagues and staff that have worked in the HVAC Research Group are worthy of many thanks: Dr. G. Ge, Dr. A. Abdel-salam, Dr. M. Abdel-salam, Dr. F. Fathieh, Dr. M. Rafati Nasr, Ms. S. Niroomand, Mr. D. Storle, Mr. P. Navid, Mr. A. Hossain, Mr. E. Nampoothiry, and Mr. B. Xing.

Financial assistance from the following sources is gratefully acknowledged: Fredeen Scholarship in Engineering, Dean's Scholarship, Toyota Automotive Engineering and Safety Scholarship, Robert Falside Stoddart Memorial Scholarship, University of Saskatchewan Graduate Devolved Scholarship, and Natural Sciences and Engineering Research Council of Canada (NSERC).

DEDICATION

I dedicate this thesis to my family members for providing me with a platform for the pursuit of scholastic excellence, and to my grandmother for teaching me about life and the Word of God.

In Him was Life, and that Life was the Light of men.
The Light shines in the darkness, and the darkness has not overpowered it.
John 1:4,5 (Weymouth New Testament)

Surely a spirit is in man, And the breath of the Mighty One Doth cause them to understand.
Job 32:8 (Young's Literal Translation)

TABLE OF CONTENTS

LIST OF TABLES

Table **Page**

LIST OF FIGURES

NOMENCLATURE

Acronyms

EDX	Energy dispersive X-ray spectroscopy
HVAC	Heating, ventilating and air-conditioning
LAMEE	Liquid-to-air membrane energy exchanger
SEM	Scanning electron microscopy

Roman symbols

Adjusted value	Adjusted or corrected value of the settings (confidence interval and scale factor) of the indirect non-invasive analysis methods after calibration
A_{mem}	Membrane surface area (m^2)
B	Systematic uncertainty
C_{sol}	Solution concentration (kg_{salt}/kg_{sol})
C_{sol}^*	Dimensionless solution concentration
$C_{sol,sat}$	Solution saturation concentration (kg_{salt}/kg_{sol})
d	Discrepancy in the standard deviation of moisture transfer flux or moisture transfer resistance between Groups 1 and 2
D	Diameter of the inner pipe of the LAMEE (mm)
Default value	Default or original value of the settings (confidence interval and scale factor) of the indirect non-invasive analysis methods before calibration
df	Degree of freedom
EB	Energy balance (kJ)
EB^*	Normalized energy balance
F	Indirect non-invasive parameter method (refers to moisture transfer flux or moisture transfer resistance)
f_{sl}	Criterion for fouling detection – slope method
f_{st}	Criterion for fouling detection – statistical method
f_u	Criterion for fouling detection – uncertainty method
h	Specific enthalpy (J/kg)
h_{fg}	Latent heat of vaporization (J/kg)

Interval	Interval is the step size that is used for the adjustment of the confidence interval and scale factor of the indirect non-invasive analysis methods
m	Mass (g)
$\dot{m}$	Mass flow rate (kg/s)
M^*	Normalized moisture transfer flux
MB	Moisture balance (g)
MB^*	Normalized moisture balance
$m_{LAMEE,f}$	Mass of the LAMEE after a test (g)
$m_{LAMEE,i}$	Mass of the LAMEE before a test (g)
$\dot{m}''_v$	Moisture transfer flux ($g/(m^2 \cdot h)$)
$\dot{m}''_{v,discrepancy}$	Discrepancy in moisture transfer flux between the start point of the steady-state period of a test and the extrapolation point (%)
$\dot{m}''_{v,o}$	Moisture transfer flux at the start of the steady-state period of a test ($g/(m^2 \cdot h)$)
$\dot{m}''_{v,o'}$	Moisture transfer flux at the extrapolation point of a test ($g/(m^2 \cdot h)$)
n	Number
P	Random uncertainty
q	Energy (kJ)
R	Moisture transfer resistance ($m^2 \cdot s/kg_{air}$)
R^*	Normalized moisture transfer resistance
RH	Relative humidity (%)
R_o	Moisture transfer resistance at the start of the steady-state period of a test ($m^2 \cdot s/kg_{air}$)
SE	Standard Error – standard deviation of the mean
SEE	Standard Error of Estimate
SF	Scale factor
t	Time (s)
t’	Student distribution constant
$t_{df,95\%}$	Critical t-value at the corresponding degree of freedom and 95% confidence interval
t_{1-2}	t-statistic that is used to compare Groups 1 and 2

T_{sol}	Solution temperature (^oC)
U	Total uncertainty at 95% confidence interval
W	Humidity ratio (kg_w/kg_{air})
$W_{sol(i)}$	Solution humidity ratio of the moving point of a test (kg_w/kg_{air})
$\overline{W}_{sol(i:e)}$	Average of the solution humidity ratio between a moving point and the end point of a test (kg_w/kg_{air})
$W_{sol(m)}$	Solution humidity ratio at the maximum point of a test (kg_w/kg_{air})
ΔW_{lm}	Log-mean humidity ratio (kg_w/kg_{air})

Greek symbols

σ	Standard deviation
$\sigma_{W_{sol(i:e)}}$	Standard deviation of the solution humidity ratio between a moving point and the end point of a test (kg_w/kg_{air})
φ	Individual terms of an equation

Subscripts

air	Air
e	End point of a test
Group 1	Control group where there is no fouling
Group 2	Test group where fouling is examined
i	Moving point of a test
in	Inlet of the LAMEE
m	Maximum point of a test
$\dot{m}''_{v,Group\ 1}$	Moisture transfer flux of Group 1
$\dot{m}''_{v,Group\ 2}$	Moisture transfer flux of Group 2
n	Number
o	Start of the steady-state period of a test
o’	Extrapolation point of a test
out	Outlet of the LAMEE
sol	Salt solution or liquid water

w	Water vapor
$W_{sol(i)}$	Solution humidity ratio of the moving point of a test

CHAPTER 1

INTRODUCTION

1.1 MOTIVATION

Fouling can simply be defined as the buildup of unwanted material on surfaces. Fouling is ubiquitous in industry, and adversely affects both heat exchangers [1] and membrane exchangers [2]. Fouling reduces the effectiveness of heat exchangers [3]. In membrane exchangers, fouling results in the deposition of particles either within membrane pores (internal fouling) or on membrane surfaces (external fouling), and limits the quantity of moisture than can permeate through a membrane [2].

Fouling results in substantial (i) technical, (ii) environmental, and (iii) economic consequences in industry. Firstly, fouling leads to an increase in the energy consumption of processes and equipment, material replacement and maintenance, and downtime losses [4],[5]. Secondly, the increase in energy consumption that is caused by fouling leads to a rise in the amount of CO_2 emissions released into the environment. Fouling in crude oil refineries reportedly contributes up to 2.5% of the worldwide CO_2 emissions caused by humans [6]. Thirdly, fouling significantly impacts the economy of nations, and is estimated to account for 0.25% – 0.35% of the gross national product of industrialized countries [7]. The economic cost of fouling is equivalent to approximately US$ 5 – 7 billion and US$ 47 – 66 billion in Canada and the USA, respectively, in 2016, using economic data from The World Bank Group [8],[9].

Although fouling negatively impacts on several industries (*e.g.* power generation, desalination, mining, oil and gas production, etc.), this thesis focuses on fouling in heating, ventilating and air-conditioning (HVAC) applications. This is because HVAC systems account for about half of the energy consumed in buildings and up to one-fifth of the total energy consumed in developed countries [10]. In 2002, buildings accounted for approximately 33% of global CO_2 emissions released to the atmosphere, and this value is projected to increase by a factor of 50% by 2030 [11].

In addition, the global demand for air-conditioning is projected to rise by over a factor of 30 between 2000 and 2100 [12]. Considering that the majority of people spend up to 90% of their time in buildings, the use of HVAC systems to provide thermal comfort and high indoor air quality favorably impacts on the wellbeing and performance of occupants [13].

Within the field of HVAC systems, previous researchers have focused on heat exchanger fouling (Refs. [14]–[24]) rather than membrane fouling (Refs. [25]–[27]). Nevertheless, membranes are increasingly adopted in HVAC applications [28], such as in air-to-air membrane energy exchangers for ventilation energy recovery. A recent progress in the application of membranes in HVAC systems is the development of a liquid-to-air membrane energy exchanger (LAMEE). Unlike conventional heat exchangers that transfer only heat between fluid streams, LAMEEs use semi-permeable membranes to either independently or simultaneously exchange heat and moisture between an air stream and a liquid desiccant solution [29]–[31].

Although LAMEEs are highly promising and have been projected to potentially reduce the energy consumption of HVAC systems by 20% – 60% [29], the porous membranes used in LAMEEs are susceptible to fouling. Yet, there is a paucity of studies on fouling in LAMEEs and in other membrane exchangers used in HVAC applications. In addition, the need to conduct in-depth research on membrane fouling in HVAC applications has been suggested by recent review papers such as Refs. [28] and [30]. Consequently, solving the challenges of fouling in LAMEEs can potentially minimize the energy that is consumed by HVAC systems.

1.2 LITERATURE SURVEY

The survey of previous research on fouling, presented in this section, is divided into three parts. The first part (Section 1.2.1) addresses the methods that are used to detect fouling in heat and membrane exchangers in diverse applications, and the second part (Section 1.2.2) focuses on crystallization fouling in membrane exchangers for HVAC applications. The third part (Section 1.2.3) outlines the research gaps that are identified from the review in the first two parts.

1.2.1 Fouling detection methods

As highlighted in Section 1.1, fouling results in severe losses to the industry. Although the main goal of fouling research is to prevent the occurrence of fouling [32], fouling can only be regulated

or mitigated but not completely eradicated. The first step towards the control of fouling is the application of methods that can detect the occurrence, onset and development of fouling in heat and membrane exchangers. Diverse fouling detection methods have been documented in the literature (Refs. [33]–[35]), and these methods can be categorized as either invasive or non-invasive. Invasive methods can physically examine fouling, but require the interruption of processes or teardown of equipment to extract and characterize fouling deposits. However, non-invasive methods are able to detect fouling without physical interaction with a surface and do not interfere with process operations. An overview of various fouling detection methods is shown in Figure 1.1.

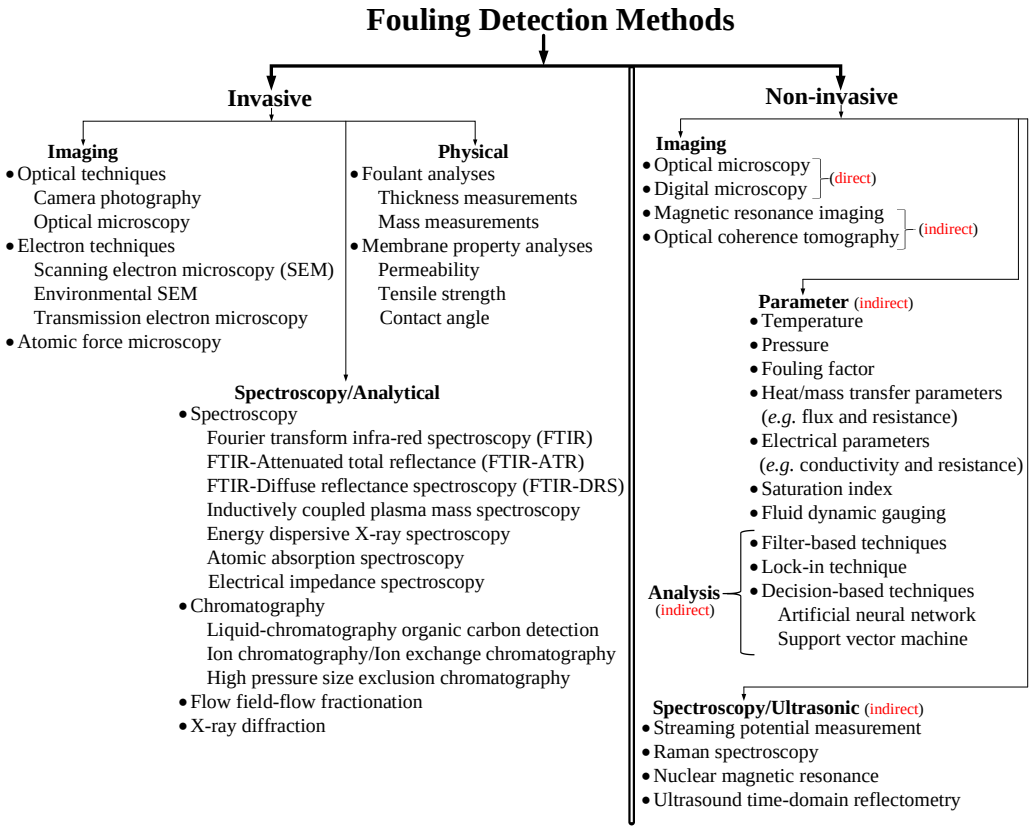

Figure 1.1. Classification of fouling detection methods. **Note**. The methods are compiled from Refs. [4],[25],[26],[33]–[73].

Figure 1.1 shows that fouling detection methods can be broadly classified into invasive and non-invasive methods, and further divided into sub-categories which include lists of specific methods. As an example, scanning electron microscopy (SEM) is an invasive method that is classified under the "imaging" sub-category because it can be used to image the surface of a material to detect the presence of fouling deposits. In this thesis, non-invasive methods are also divided into direct and

indirect methods (*see* Figure 1.1). Direct non-invasive methods can be used to non-invasively and directly detect fouling. In Figure 1.1, digital microscopy is a direct non-invasive method that is classified under the "imaging" sub-category. Digital microscopy can be used to directly observe fouling during a test. On the other hand, indirect non-invasive analysis methods can be used to non-invasively and indirectly detect fouling by analyzing measurements of indirect non-invasive parameter methods. In Figure 1.1, decision-based techniques are indirect non-invasive analysis methods that are classified under the "analysis" sub-category. Decision-based techniques can be used to indirectly detect fouling by analyzing indirect non-invasive parameter methods (*e.g.* flux).

Although both non-invasive and invasive methods have been used to detect fouling in heat and membrane exchangers, fouling studies (*e.g.* Refs. [36],[43],[46],[69]) typically confirm fouling by monitoring the degradation in the performance of exchangers using indirect non-invasive parameter methods (*e.g.* flux or resistance), and subsequently examine the presence and characteristics of fouling deposits directly using an invasive method like SEM. As a result, these studies are only able to confirm that fouling occurred in a test, and the point at which fouling started (*i.e.* the onset of fouling) is not determined.

The scarcity of studies that have investigated the onset of fouling in exchangers is a major gap in the fouling literature. The ability to detect the start of fouling can serve as an early warning system that gives room for the implementation of strategies that can prevent significant damage to exchangers from the accumulation of deposits. Invasive methods are not appropriate for online monitoring of fouling in exchangers because they are disruptive and time-consuming. On the other hand, non-invasive methods are well suitable for real-time detection and diagnostics of fouling in exchangers, and enable engineers to identify operational parameters that can control fouling in real-time and minimize financial losses.

A few studies (*e.g.* Refs. [26],[65],[67]) have detected the onset of fouling using direct non-invasive methods which involve the observation of fouling in real-time. In these studies, the direct non-invasive methods were observed to detect the start of fouling earlier than the indirect non-invasive parameter methods that were implemented (*i.e.* measurements of moisture transfer rate or flux). Nevertheless, the results of the direct non-invasive methods were not used to calibrate the

indirect non-invasive parameter methods. Thus, the sensitivities of the indirect non-invasive parameter methods were not tuned to detect fouling early.

There are limited studies (*e.g.* Refs. [49],[56],[70]) that have used indirect non-invasive analysis methods to detect when a change in an indirect non-invasive parameter method is enough to confirm the occurrence or start of fouling. Ref. [49] used Kalman filter methods to analyze measurements of temperature and mass flow rate. Ref. [56] implemented a lock-in method to analyze temperature measurements, whereas Ref. [70] applied acoustic parameters (which were obtained from ultrasonic measurements) within an artificial neuron network. However, the indirect non-invasive analysis methods implemented in these three studies suffer from two key limitations. Firstly, the methods make use of complex mathematic models which may not be easily implementable to detect fouling in operating exchangers. Secondly, the methods generally require large data sets (from hundreds to millions of samples) to reliably detect fouling.

None of the studies of Refs. [49],[56],[70] systematically compared the performance of various indirect non-invasive analysis methods to detect the onset of fouling. Ref. [47] recently applied four indirect non-invasive analysis methods to detect the start of fouling in a domestic hot water exchanger by analyzing simulated overall heat transfer coefficient and temperature data. However, the sensitivity of the analysis methods was assessed using a design fouling factor rather than a direct fouling detection method, and the analysis methods were not subsequently calibrated to detect the start of fouling.

This thesis addresses the lack of systematic development and comparison of non-invasive methods that can detect the onset of fouling in exchangers. In this thesis, indirect non-invasive analysis methods will be used to detect the onset of fouling in a LAMEE at different operating conditions, and the sensitivity of the analysis methods will be calibrated using a direct non-invasive method.

1.2.2 Crystallization fouling in membrane exchangers for HVAC applications

As previously mentioned in Section 1.1, membranes have a high potential for HVAC applications but a key limitation is their propensity for fouling. So far, only three studies have addressed fouling in membrane-based HVAC systems (Refs. [25]–[27]). Charles and Johnson [25] and Crawford and da Silva [26] studied the effect of crystallization fouling on the performance of membrane exchangers used for evaporative cooling, whereas Engarnevis *et al.* [27] studied the effect of

particulate fouling on the performance of air-to-air membrane energy exchangers used for ventilation energy recovery. The effects of air-side particulate and biological fouling on membranes were also investigated in the study of Ref. [25], and the results indicated that crystallization fouling had the greatest adverse effect on the performance of the exchanger.

Although the three studies on fouling in membrane-based HVAC systems (Refs. [25]–[27]) only examined three types of fouling (crystallization, particulate and biological), fouling itself can be categorized into five types, namely: (i) crystallization, (ii) particulate, (iii) biological, (iv) corrosion, and (v) chemical reaction [74]. However, this thesis focuses on crystallization fouling for a number of reasons which are briefly outlined in the following paragraphs.

Firstly, the physics of operation of LAMEEs favors the occurrence of crystallization fouling. The driving potential in LAMEEs is the difference in humidity ratio between air that is in equilibrium with the desiccant solution and the bulk air stream. As moisture is transferred from the desiccant solution to the air stream, crystals may precipitate from the solution and accumulate on the membrane. The buildup of crystals on the membrane would serve as an additional resistance to moisture transfer from the solution to the air stream. The resistance circuit of the LAMEE is shown in Chapter 3 (Figure 3.2), and the equations that relate the driving potential in the LAMEE to the moisture transfer flux and resistance are presented in Chapter 3 (**Eqs. 3.3** and **3.4**).

Secondly, it is envisaged that the impact of air side particulate fouling would be insignificant if appropriate air-side filters are installed in the HVAC system. Thirdly, the occurrence of biological fouling in liquid desiccants is questionable because of their low relative humidity [28], which may be unsuitable to the growth of micro-organisms. Although Charles and Johnson [25] reported the observation of biological fouling on the air side of a membrane-based evaporative cooling unit, its effects were reported to be minimal in the same study [25].

Fourthly, corrosion fouling may be avoided by using (i) corrosion-resistant materials such as plastic/fiber reinforced plastic [75], synthetic plastic [76], titanium [77], and copper-nickel alloy [77], (ii) corrosion inhibitors (*e.g.* lithium chromate [78]), and (iii) alternative liquid desiccants which are less corrosive (*e.g.* potassium formate [77]). Finally, chemical reaction fouling is

unlikely to occur if there are no reactants or catalysts in the feed solution that may initiate chemical reactions that form products which can foul the membrane.

There are no studies in the literature on crystallization fouling in LAMEEs, and only two studies (Refs. [25] and [26]) have addressed the effect of mineral fouling on membrane exchangers used for evaporative cooling. The studies of Refs. [25] and [26] reported that crystallization fouling could reduce the amount of moisture transfer through a membrane by over 90% within 100 [25] and 14 [26] hours of testing. Although the two studies (Refs. [25] and [26]) also investigated the presence of crystal formation on fouled membranes using SEM, the studies were essentially preliminary studies and a comprehensive characterization of crystallization fouling in membranes was not performed. Three limitations of the previous research on crystallization fouling in membrane exchangers for HVAC applications are highlighted in Sections 1.2.2.1, 1.2.2.2 and 1.2.2.3, and will be subsequently addressed in this thesis.

1.2.2.1 Range of test parameters

The limited range of test parameters in the studies of Refs. [25] and [26] are briefly described under the following points.

- **Operating conditions**. Crystallization fouling has been tested at very few operating conditions. The study of Ref. [25] assessed fouling in a membrane exchanger at one air relative humidity and two solution concentrations, whereas the study of Ref. [26] assessed fouling at one air relative humidity and one solution concentration.
- **Moisture transfer rate**. Although the study of Ref. [25] documented the impact of solution concentration on crystallization fouling in the exchanger tested, the studies of Refs. [25] and [26] did not assess the impact of moisture transfer rate through membranes on the likelihood for crystallization fouling in membrane exchangers.
- **Membrane**. The studies of Refs. [25] and [26] tested only one type of membrane, and the effect of any membrane properties on the likelihood of fouling in the exchangers was not assessed.

1.2.2.2 Evolution of fouling

The studies of Refs. [25] and [26] used indirect non-invasive parameter methods to monitor the performance of membrane exchangers during experimental tests, and the study of Ref. [26] further

examined the evolution of fouling in a membrane exchanger by using a direct non-invasive method (*i.e.* time-lapse photography). However, there are three limitations in the previous studies of Refs. [25] and [26]. Firstly, the regimes of crystallization fouling in membranes were not identified in any of the two studies. Secondly, the morphology of crystal deposits on membranes at different periods of a test was not characterized; thus, structural transformations in the crystal deposits as a function of time were not determined. Thirdly, none of the two studies used both non-invasive and invasive methods to comprehensively analyze the evolution of crystallization fouling in membranes. Nevertheless, it is important to identify the development of fouling in the LAMEE in order to gain insight into the growth and mechanisms of crystallization fouling in membranes.

1.2.2.3 Elemental analysis

Although the studies of Refs. [25] and [26] characterized the morphology of fouling deposits using SEM, neither study performed elemental analysis to determine the composition of deposit formations on fouled membranes. The elemental analysis of fouling deposits can aid in identifying dominant foulant elements and the regions where foulants accumulate on a membrane.

1.2.3 Research gaps

The key research gaps that have been identified from the literature survey in Sections 1.2.1 and 1.2.2 are outlined as follows (*the research gap numbers will be used throughout the thesis*):

1. Development of indirect non-invasive analysis methods to detect fouling:
    - **a.** Application of indirect non-invasive analysis methods to detect the onset of fouling.
    - **b.** Calibration of indirect non-invasive analysis methods using a direct non-invasive method.
2. Comprehensive characterization of crystallization fouling in LAMEEs:

    Range of test parameters
    - **a.** Evaluation of the impact of moisture transfer rate on fouling.
    - **b.** Investigation of different operating conditions that result in fouling.
    - **c.** Evaluation of the impact of membrane resistance on fouling.

    Evolution of fouling
    - **d.** Identification of the regimes of crystallization fouling growth in a LAMEE.
    - **e.** Delineation of the evolution of crystallization fouling in membranes.

    Elemental analysis
    - **f.** Analysis of the composition of membrane foulants.

1.3 RESEARCH OBJECTIVES

Three research objectives are developed to address the research gaps outlined in Sections 1.2.3. Firstly, the primary goal of this thesis is to develop and calibrate indirect non-invasive analysis methods to detect the onset of crystallization fouling in a LAMEE. Secondly, the different operating conditions that are likely to result in crystallization fouling in LAMEEs will be identified. Thirdly, the evolution of crystallization fouling in membranes will be identified. A detailed list of the research objectives of the thesis and the chapters where each objective is addressed is presented in Figure 1.2.

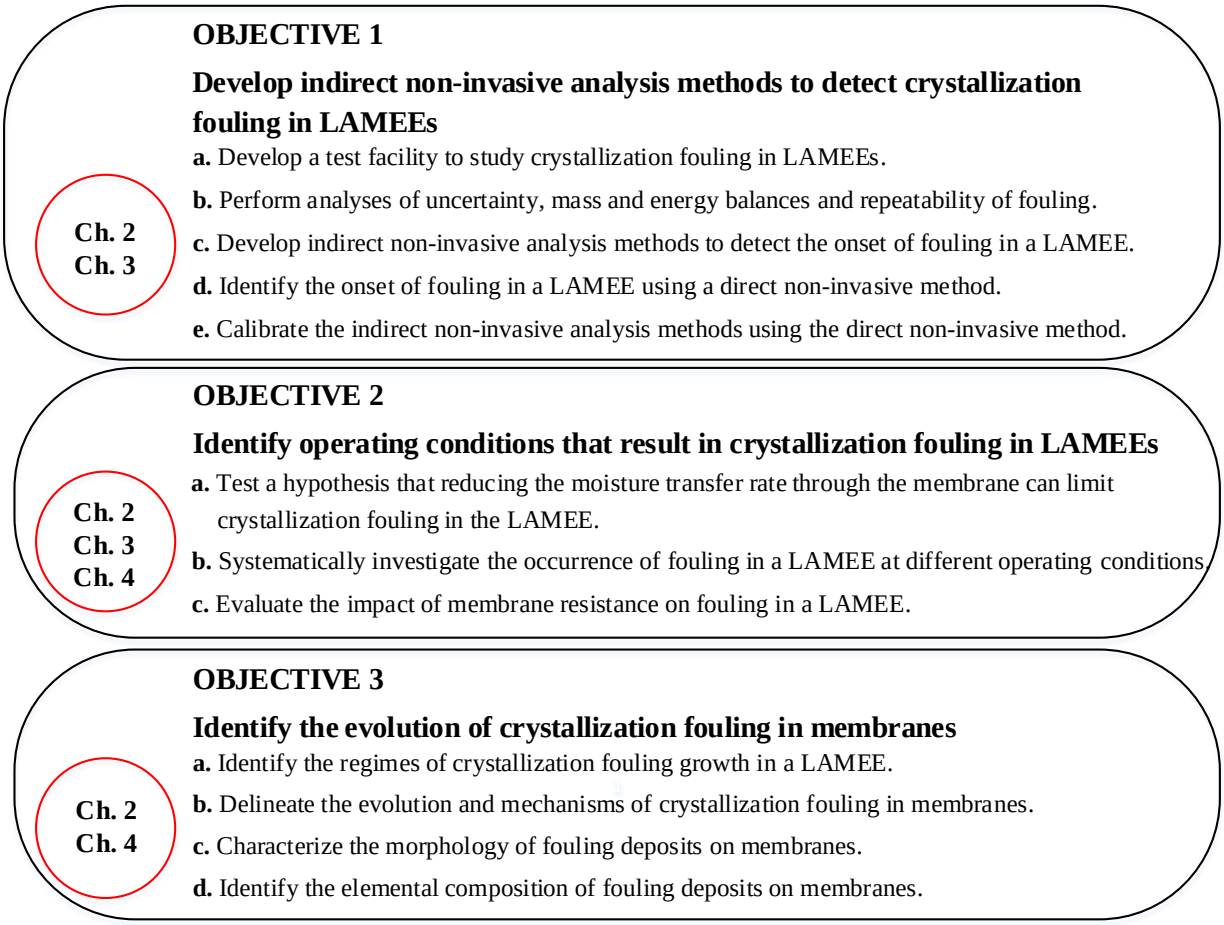

Figure 1.2. Overview of the research objectives of the thesis and the chapters where each objective is addressed. **Note**. The numbers that correspond to the research objectives will be used throughout the thesis.

1.4 THESIS STRUCTURE

The thesis is written in manuscript-style, and consists of five chapters (Chapters 1 – 5) and two appendices (Appendices A and B). Chapter 1 contains an introduction to the thesis and Chapter 5 contains the conclusions of the thesis. Each of the middle chapters (Chapters 2, 3 and 4) consist of a research paper that addresses a portion of the three thesis objectives outlined in Figure 1.2.

The first objective of the thesis will be addressed in Chapters 2 and 3. In Chapter 2, the background work for the thesis will be presented, including the test facility used to study crystallization fouling in LAMEEs and uncertainty analysis. Furthermore, two indirect non-invasive analysis methods (uncertainty and statistical methods) are developed to detect the onset of fouling by analyzing one indirect non-invasive parameter method (moisture transfer flux). In Chapter 3, an additional indirect non-invasive analysis method (slope method) is developed and the three indirect non-invasive analysis methods will be used to detect the onset of fouling by evaluating two indirect non-invasive parameter methods (moisture transfer flux and resistance). In addition, a direct non-invasive method (digital microscopy) will be used to determine the onset of crystallization fouling in the LAMEE. The three indirect non-invasive analysis methods (uncertainty, statistical and slope methods) will then be calibrated using the results from the direct non-invasive method.

The second objective of the thesis is to identify different operating conditions that are likely to result in crystallization fouling in LAMEEs. The second objective of the thesis consist of three points which will be addressed in Chapters 2, 3 and 4. Firstly, in Chapter 2, a hypothesis that states that reducing the moisture transfer rate through the membrane can limit the likelihood of crystallization fouling in the LAMEE will be tested by comparing the occurrence and impact of fouling on the moisture transfer flux of the LAMEE in tests performed at different moisture transfer rates. The hypothesis will be further tested in Chapter 4 by using invasive methods (scanning electron microscopy (SEM) and energy dispersive X-ray spectroscopy (EDX)) to analyze the spatial morphology and composition of fouling deposits on a membrane in which moisture transfer occurs only at certain regions of the membrane. Secondly, the conditions that lead to crystallization fouling in LAMEEs will be identified in both Chapters 2 and 3. To identify the conditions that are likely to cause crystallization fouling in the LAMEE, two indirect non-invasive analysis methods (uncertainty and statistical methods) will be used to evaluate one

indirect non-invasive parameter method (moisture transfer flux) in Chapter 2. In Chapter 3, an indirect non-invasive analysis method (slope method) will be introduced, and the three indirect non-invasive analysis methods will be used to confirm or reject the occurrence of fouling by evaluating two indirect non-invasive parameter methods (moisture transfer flux and resistance). Thirdly, the impact of membrane resistance on crystallization fouling in LAMEEs will be assessed in Chapter 3 by examining the occurrence and onset of fouling in the LAMEE using two types of membranes with different vapor diffusion transfer resistances.

The third objective of the thesis is to identify the evolution of crystallization fouling in membranes. The third objective of the thesis consists of four points, and the first point will be addressed in Chapter 2 and the remaining three points will be addressed in Chapter 4. Firstly, the regimes of crystallization fouling growth in a LAMEE will be identified by analyzing an indirect non-invasive parameter method (moisture transfer flux) during a test. Secondly, the evolution and mechanisms of crystallization fouling in membranes will be identified by using non-invasive methods (two indirect non-invasive parameter methods – moisture transfer flux and resistance) and invasive methods (optical microscopy and SEM). Thirdly, the morphology of fouling deposits will be characterized using an invasive method (SEM). Finally, an invasive method (EDX) will be used to analyze the composition of fouling deposits on membranes.

Chapter 5 provides a summary, the key conclusions and contributions of the thesis, and also suggests some areas for future research. The copyright permissions for the manuscripts included in this thesis are given in Appendix A, and a desiccant solution property is given in Appendix B.

1.5 LIST OF PUBLICATIONS

1.5.1 Papers in Refereed Journals

The following chapters of the thesis consist of the manuscripts that are outlined below:

Chapter 2 Olufade, A. O.; Simonson, C. J. Detection of crystallization fouling in a liquid-to-air membrane energy exchanger. *Experimental Thermal and Fluid Science* 2017, *in press*.

Chapter 3 Olufade, A. O.; Simonson, C. J. Development of non-invasive methods to detect the onset of crystallization fouling in a liquid-to-air membrane energy exchanger. *Journal of Membrane Science* 2017, *submitted.*

Chapter 4 Olufade, A. O.; Simonson, C. J. Characterization of the evolution of crystallization fouling in membranes using non-invasive and invasive methods. *Langmuir* 2017, *submitted*.

The research papers in Chapters 2, 3 and 4 have been slightly modified to eliminate repetition and make the thesis cohesive.

1.5.2 Papers in Conference Proceedings

The following conference papers were published from this PhD research but are not included in this thesis:

Olufade, A.; Simonson, C. Quantitative detection of crystallization fouling in a liquid-to-air membrane energy exchanger. In: Keller, L.; Sengpiel, R.; Offermann, S. (Eds.), *Proceedings of the 16th Aachener Membran Kolloquium*; Aachen, Germany, November 2 – 3, 2016; pp 105–113.

Olufade, A. O.; Simonson, C. J. Impact of crystallization fouling on the moisture transfer resistance of a liquid-to-air membrane energy exchanger. In: *International Conference on Heat Exchanger Fouling and Cleaning XII*; Madrid, Spain, June 11 –16, 2017.

CHAPTER 2

DEVELOPMENT OF INDIRECT NON-INVASIVE ANALYIS METHODS

2.1 OVERVIEW

This chapter is the first step towards meeting the first and second objectives of the thesis (*i.e.* to develop non-invasive methods to detect the occurrence and onset of crystallization fouling in a liquid-to-air membrane energy exchanger (LAMEE), and identify the operating conditions that lead to fouling in LAMEEs). In this chapter, a test facility which was developed to study crystallization fouling in LAMEEs is described. Afterwards, two indirect non-invasive analysis methods are developed to detect fouling in the LAMEE by evaluating one indirect non-invasive parameter method (*i.e.* moisture transfer flux). Furthermore, a hypothesis that states that crystallization fouling in the LAMEE can be reduced by reducing the rate of moisture transfer through the membrane is introduced and tested.

The test facility presented in this chapter will be slightly modified for the research described in Chapter 3 and used for the results in Chapter 4. In addition, the indirect non-invasive analysis methods presented in this chapter will be expanded in Chapter 3.

The manuscript presented in this chapter has been accepted for publication in Experimental and Thermal Fluid Science. The development of the test facility, experimental testing, data analyses and manuscript writing were performed by the first author (PhD student – Mr. Adesola O. Olufade), and the manuscript was critically reviewed by the second author (supervisor – Prof. Carey J. Simonson).

Detection of Crystallization Fouling in a Liquid-To-Air Membrane Energy Exchanger

(Accepted in Experimental Thermal and Fluid Science in October 2017)

A.O. Olufade, C.J. Simonson

2.2 ABSTRACT

A liquid-to-air membrane energy exchanger (LAMEE) is a new development for air-conditioning that facilitates the exchange of heat and moisture between air and liquid streams, through a semi-permeable membrane. However, fouling may occur in the membrane and severely lower the performance of a LAMEE.

The primary aim of this chapter is to develop indirect non-invasive analysis methods to detect crystallization fouling in the LAMEE by analyzing the changes in an indirect non-invasive parameter method (*i.e.* moisture transfer flux). Two indirect non-invasive analysis methods, which consist of uncertainty and statistical methods, are applied to confirm or reject the occurrence of fouling in the LAMEE for several tests in which $MgCl_2$(aq) desiccant solution is dehydrated.

The results indicate that crystallization fouling can be detected in the LAMEE with the methods presented. Crystallization fouling can reduce the rate of moisture transfer through the membrane by up to 60%. Furthermore, a major contribution of this chapter is that reducing the rate of moisture transfer through the membrane can delay crystallization fouling in the LAMEE.

2.3 INTRODUCTION

Fouling is the accumulation and attachment of unwanted matter on a surface [2]. Fouling reduces the overall heat transfer coefficient and efficiency of heat exchangers [79], and affects over 90% of the heat exchangers used in industry [32]. Membranes are also plagued with fouling due to particles which deposit and block the membrane pores, form a layer on the membrane surface, or a combination of both mechanisms [2]. Fouling results in severe technical and economic consequences, and heating, ventilating and air-conditioning (HVAC) systems account for a significant share of global energy consumption as described in Chapter 1 (Section 1.1).

This chapter partially addresses the two research gaps of the thesis. The specific sub-research gaps of the thesis that are addressed in this chapter are 1(**a**), 2(**a**), 2(**b**) and 2(**d**) (*the research gaps of the thesis and their corresponding numbers are given in Chapter 1 (Section 1.2.3)*).

Research gap 1(**a**) is the lack of development and application of indirect non-invasive analysis methods to detect the onset of fouling. As previously discussed in Chapter 1 (Section 1.2.1), many fouling studies (*e.g.* Refs. [36],[43],[46],[48],[69],[80]) typically confirm or reject the occurrence of fouling in a test by using the traditional approach of monitoring the changes in the performance of an exchanger, and subsequently examining membranes or plates/tubes to identify and characterize deposit formations. The major problem with the traditional approach is the delayed detection of fouling. Consequently, fouling usually results in the substantial accumulation of deposits which damages exchangers long before the measured performance of the exchangers noticeably deteriorate.

The methods used to investigate deposit formations are normally invasive, because they interrupt operating processes to physically examine the presence of fouling. Invasive methods can neither reliably detect the initiation of deposit formation nor rapidly detect and monitor fouling in real-time industrial systems. On the other hand, non-invasive methods can detect fouling without interfering with operating exchangers, and can be applied for online detection of fouling in practical systems. Thus, this chapter focuses on the development of indirect non-invasive analysis methods that can be used to detect the start of fouling in a liquid-to-air membrane energy exchanger (LAMEE).

As outlined in Chapter 1 (Section 1.2.3), research gap 2(**a**) is the absence of evaluation of the impact of moisture transfer rate on fouling in a LAMEE, and research gap 2(**b**) is the lack of investigation of the different operating conditions that lead to fouling in a LAMEE. Research gap 2(**d**) involves identifying the regimes of crystallization fouling growth in a LAMEE.

To address the aforementioned research gaps, this chapter aims to meet the following objectives of the thesis (*see Figure 1.2 in Chapter 1 for the complete list of the objectives of the thesis that use the same numbering as presented here*):

1(**a**): Develop a test facility to study crystallization fouling in LAMEEs.

1(**b**): Perform analyses of uncertainty, mass and energy balances and repeatability of fouling.

1(**c**): Develop indirect non-invasive analysis methods to detect the onset of fouling in a LAMEE.

2(**a**): Test a hypothesis that reducing the moisture transfer rate through the membrane can limit crystallization fouling in the LAMEE.

2(**b**): Systematically investigate the occurrence of fouling in a LAMEE at different operating conditions.

3(**a**): Identify the regimes of crystallization fouling growth in a LAMEE.

2.4 THEORY AND HYPOTHESIS OF EXPERIMENT

Crystallization fouling typically occurs when ions precipitate from a salt solution and attach to the surface of a heat exchanger [81] or membrane [38]. Generally, crystallization fouling involves complex thermo-chemical and hydrodynamic processes [69], and is impacted by diverse factors such as solution type and properties (*e.g.* concentration, pH), operating conditions (*e.g.* heat flux, fluid velocity and temperature, wall conditions), surface properties (*e.g.* roughness, surface energy), membrane properties (morphology, pore size and distribution), and equipment configuration or geometry (Refs. [2],[69],[82]).

Supersaturation is a principal condition for crystallization [83], and therefore plays a key role in the formation and growth of crystallization fouling. Supersaturation, or supersolubility, occurs when the solution exceeds its saturation concentration at a given temperature. When supersaturation is achieved, foreign substances in the solution or surface defects may induce the seeding of crystal nuclei [81]. Supersaturation can be achieved through several processes, namely:

a. Evaporation of water from a salt solution such that the concentration of salt exceeds the saturation concentration [84],[85].
b. Cooling of a normal solubility salt solution below its saturation temperature [84].
c. Heating of a reverse solubility salt solution above its saturation temperature [84].
d. Mixing of solutions [84],[85].
e. Alteration of the pH of a solution [84].

Crystals may nucleate on the membrane surface (surface crystallization), or within the bulk solution (bulk crystallization) and deposit on the membrane surface [38]. Furthermore, nucleation may be enhanced due to the presence of seeded crystals or suspended particles in the bulk solution [38].

Crystal growth can be explained by diffusion-reaction theories [83], which consist of mass diffusion and reaction kinetics. Mass diffusion transports ions from the solution to a surface due to the concentration difference between the bulk solution and the solution near the interface. Reaction kinetics involves the attachment of the solute ions to the surface due to the driving force between the interface and solution saturation concentrations [69],[83]. Crystallization fouling may be governed by diffusion, reaction, or a combination of both mechanisms depending on the operating condition [84].

The experimental scenario consists of a dry air stream and a liquid desiccant solution, which are separated by a semi-permeable membrane. As dry air flows on one side of the membrane, moisture is transferred from the liquid desiccant to the air stream through the pores of the membrane. It is envisaged that the continuous evaporation of water from the liquid desiccant at constant temperature will increase the interface concentration of the desiccant solution until it is supersaturated. The attainment of supersaturation at the solution-membrane interface may initiate the nucleation of crystals on the membrane surface. If the bulk solution is already supersaturated, crystals may directly nucleate on the membrane surface or crystals may transport from the bulk solution and attach on the membrane surface. The growth of crystals on the membrane can block the membrane pores, and eventually reduce the rate of moisture transfer through the membrane.

Although supersaturation is created by evaporating water from a liquid desiccant at constant temperature, normal solubility salts (*e.g.* $MgCl_2$) can also be cooled below their saturation temperature to achieve supersaturation. However, the approach of cooling the solution to achieve supersaturation is not considered in this thesis. This is because changing the solution temperature affects the rate of moisture transfer through a membrane due to the coupling of heat and moisture transfer. In addition, varying the temperature of the solution may significantly influence the kinetics of crystallization fouling. Consequently, it may be difficult to assess the impact of fouling on a LAMEE due to the complexities that may arise from changing the solution temperature.

The process of evaporating a salt solution to achieve supersaturation is shown in Figure 2.1.

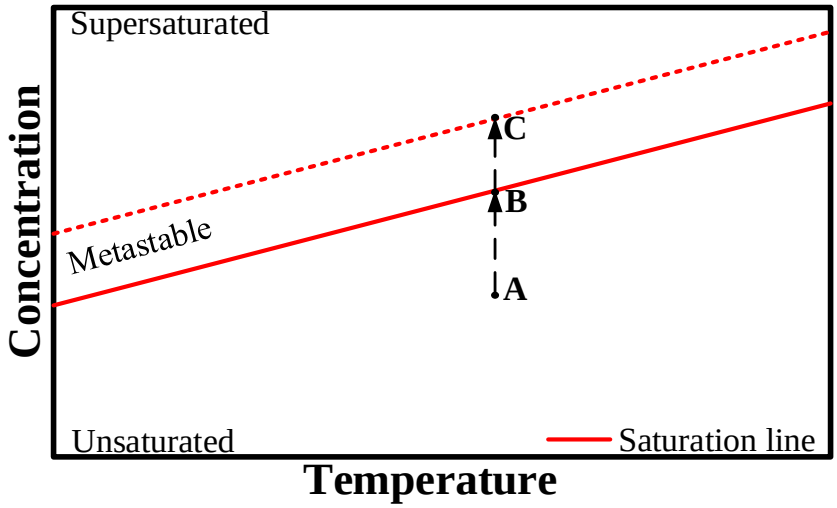

Figure 2.1. Process of supersaturation of a salt solution (A—B—C) through evaporation (adapted from Ref. [83]).

Figure 2.1 contains unsaturated, metastable and supersaturated zones, and these three zones will be briefly described based on Mullin [83]. In the unsaturated zone, the salt solution is below its saturation concentration and crystallization cannot occur. The metastable zone lies between the unsaturated and supersaturated zones where crystallization is unlikely to occur but may be initiated under special conditions. In the supersaturated zone which lies above the metastable zone, the solution is strongly supersaturated and spontaneous crystallization may even occur in the bulk fluid. During the evaporation of a salt solution at constant temperature, the solution concentration at the solution-membrane interface increases from point A in the stable zone to point B on the saturation line to point C in the metastable zone. Crystallization typically occurs when the solution concentration at the solution-membrane interface reaches point C in the metastable zone.

The supersaturation of a salt solution may be delayed or prevented by reducing the evaporation rate during the process A to C. Furthermore, the evaporation rate through the membrane can be adjusted by varying the relative humidity of air. It is therefore possible to assess the impact of the moisture transfer rate through the membrane on crystallization fouling in the LAMEE by varying the relative humidity of the air. It is expected that high moisture transfer rates may accelerate crystallization fouling, whereas low moisture transfer rates may significantly delay or prevent crystallization fouling.

A hypothesis is therefore proposed as follows:

> "Crystallization fouling in the LAMEE is influenced by the rate of moisture transfer through the membrane; thus, fouling may be reduced by lowering the rate of moisture transfer."

2.5 EXPERIMENTS

A test facility is developed to test crystallization fouling in a LAMEE. The LAMEE uses a membrane to separate an air stream from a stagnant liquid desiccant solution, while facilitating the exchange of heat and moisture between the two fluids. During a typical operation of the LAMEE, moisture is transferred from the liquid desiccant to the air stream. The evaporation of water from the liquid desiccant may result in supersaturation conditions at the solution-membrane interface and lead to crystallization fouling.

In order to simulate the conditions that may lead to crystallization fouling, a test facility is designed to deliver air flow at a regulated relative humidity, and provide stationary liquid desiccant solution at a constant concentration to the LAMEE. Figure 2.2 shows a schematic of the test facility.

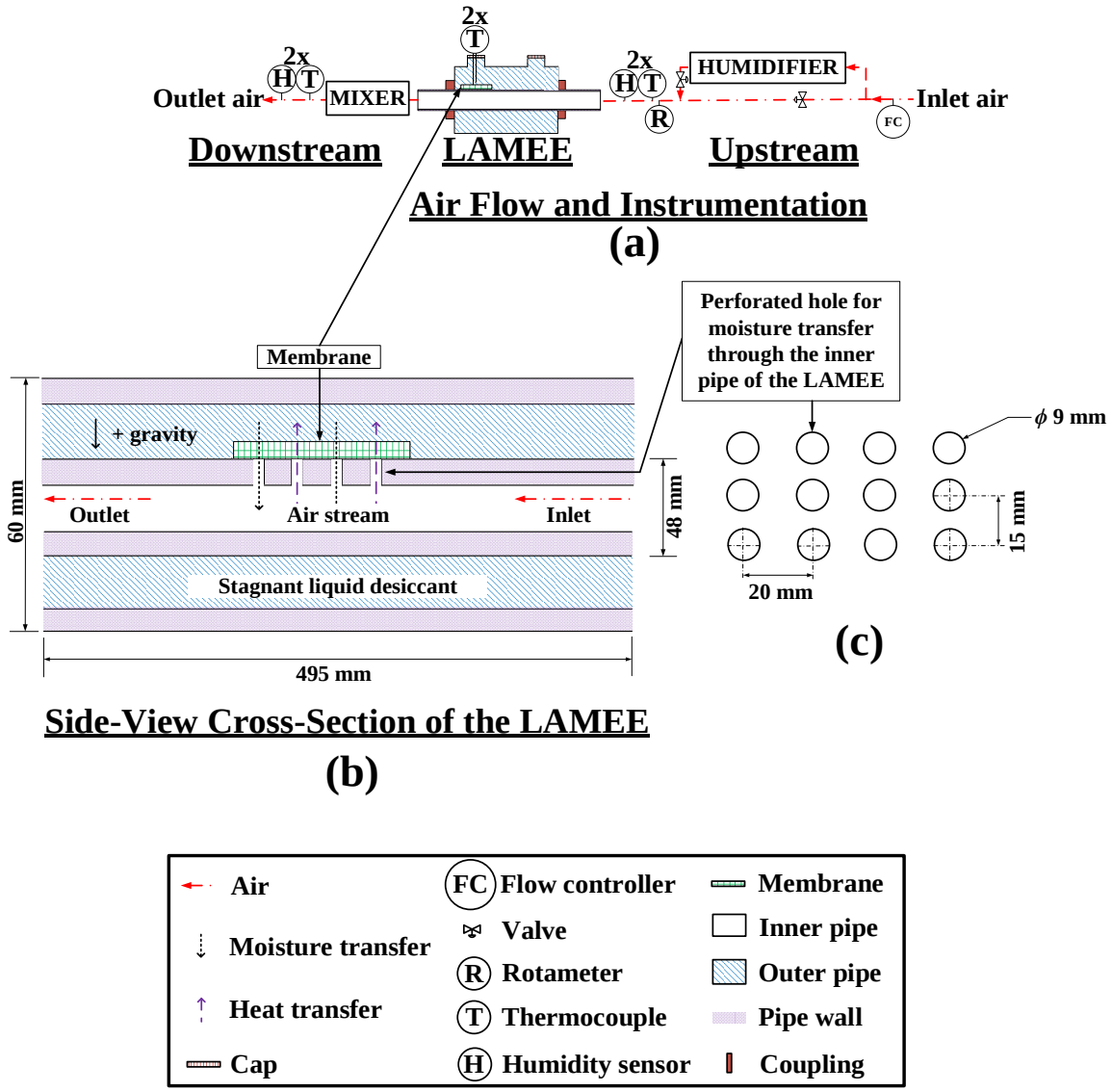

Figure 2.2. Schematic of the test facility. **Note**. The diagrams are not drawn to scale.

Figure 2.2(**a**) shows the air flow and instrumentation of the test facility which consists of an upstream section, a LAMEE and a downstream section. The side-view cross-section of the LAMEE is shown in Figure 2.2(**b**), and the arrangement and dimensions of holes in the inner pipe of the LAMEE are depicted in Figure 2.2(**c**). The pipes are impermeable to moisture transfer; thus, these holes are the areas of active moisture transfer between the air stream and the liquid desiccant.

In the test section upstream of the LAMEE (Figure 2.2**a**), air is drawn from the laboratory at room temperature conditions (~23 ^{o}C). The humidity of the air stream is conditioned with a humidifier, and its flow rate is regulated with an air flow controller and rotameter before and after the

humidifier, respectively. Hydrodynamically fully developed laminar air flow is supplied to the LAMEE with the air flow controller. Air is supplied to the LAMEE at a typical flow rate of ~1.4×10^{-5} kg/s through a plastic pipe of internal diameter, D = 40 mm (Reynolds number = ~23), and approximately 1000 mm in length (25·D).

The LAMEE is a concentric pipe energy exchanger, consisting of inner and outer pipes, as shown in Figure 2.2(**b**). Air flows through the inner pipe of the LAMEE, while a liquid desiccant solution is contained in the outer pipe (or shell). The surface of the inner pipe is perforated with 12 holes (Figure 2.2**c**) to facilitate the transfer of moisture between the liquid desiccant and air stream. The perforated holes on the inner pipe of the LAMEE are sealed with a semi-permeable membrane which prevents direct contact between the air stream and liquid desiccant, while allowing the exchange of heat and moisture between the two fluids.

In the test section downstream of the LAMEE (Figure 2.2**a**), the air stream leaving the LAMEE is mixed in order to allow measurement of the bulk properties. Finally, the air stream exits the downstream section of the test facility. Thermocouples and capacitance-based humidity sensors are used to measure the temperature and relative humidity of air at the inlet and outlet of the LAMEE, respectively. Data acquisition is performed using equipment from National Instruments (NI) (chassis: NI SCXI-1000, modules: NI SCXI-1102, terminal blocks: NI SCXI-1303), and a LabVIEW 2010 program is used to monitor and record the test data.

The specifications of the membrane used in the LAMEE are given in Table 2.1. This membrane was used in a LAMEE prototype [86], with a measured effectiveness of up to 80% [87].

Table 2.1. Specifications of the membrane used in the LAMEE [86].

Parameter and unit	**Value**
Material [-]	Expanded polytetrafluoroethylene (ePTFE) laminates
Pore size [μm]	0.3
Porosity [%]	85
Vapor diffusion resistance [s/m]	97 ± 11
Water vapor permeability [kg/(m·s)]	$6.63 \times 10^{-6} \pm 7.7 \times 10^{-7}$
Thickness [mm]	0.54 ± 0.016
Liquid penetration pressure [kPa]	>82

2.5.1 Test procedure

At the beginning of a test, a membrane is placed over the perforated holes on the surface of the inner pipe of the LAMEE, and the membrane edges are sealed to the surface of the inner pipe with double-sided and aluminum tapes. Thus, the inner pipe of the LAMEE is intact, while the outer pipe (shell side for liquid desiccant) is still disassembled. The air flow is turned on and the humidifier regulates the air humidity to a desired set point. After the temperature and relative humidity of the air stream at the upstream and downstream sections of the test facility are equal, the outer pipe (shell side) of the LAMEE is assembled.

The air flow through the inner pipe is continuous while the outer pipe, caps and couplings are being assembled around the inner pipe to make a complete LAMEE. The outer pipe of the LAMEE is filled with a liquid desiccant and a sample of the solution is taken with a syringe in order to measure the density of the solution using a density meter. The mass of the LAMEE is measured with a mass balance. The test is deemed to start once the shell of the LAMEE is filled with the desiccant solution.

During a test, the mass flow rate of air, and the temperature and relative humidity of air at the inlet and outlet of the LAMEE are measured. These measurements are used to calculate the rate of moisture transfer through a membrane, and to assess the impact of crystallization fouling on the performance of the LAMEE.

After a test, the mass of the LAMEE is measured with a mass balance and the difference between the initial and final masses of the LAMEE provides the mass of water evaporated from the liquid desiccant during the test. The density of the liquid desiccant is also measured at the end of every test with a density meter. The concentration of the liquid desiccant (C_{sol}) is determined from its measured density with a correlation from the literature [88]. The density of the liquid desiccant is measured before and after a test to confirm that the change in the bulk solution concentration is negligible during a test. The membrane is removed from the LAMEE and the LAMEE is washed with hot distilled water after every test.

2.5.2 Instrumentation and uncertainty analysis

The uncertainties in temperature and relative humidity are determined by calibrating the thermocouples and humidity sensors with a dry-well temperature calibrator (± 0.1 ^{o}C) [89] and a humidity generator (± 0.5%) [90], respectively.

The uncertainties in air flow rate (± 1%) [91] and solution density (± 0.05 kg/m^3) [92] are obtained from the manufacturer specifications, respectively. The uncertainty in mass measurement is ± 1.1 g, which is obtained from a calibration of the mass balance using standard masses. The uncertainties in the measured variables are presented in Table 2.2.

Table 2.2. Specifications and uncertainties of the instrumentation.

Instrument	**Parameter**	**Capacity/ Calibration range**	**Uncertainty**
Thermocouples (T-type)	Temperature	20 – 30 ^{o}C	± 0.2 – 0.3 ^{o}C
Humidity sensors (Honeywell HIH)	Relative humidity	10% – 50% at 20 – 30 ^{o}C	± 1%
Flow controller (MKS 1259C-10000SV)	Flow rate	0.17 L/s	± 1%
Rotameter (Dwyer RMB-SSV)	Flow rate	0.004 – 0.04 L/s	± 0.001 L/s
Density meter (Anton Paar DMA 4500M)	Density	0 – 3000 kg/m^3	± 0.05 kg/m^3
Mass balance (OHAUS Voyager Pro VP6102CN)	Mass	6.1 kg	± 0.0011 kg

Note. The uncertainty in the area of the membrane is assumed to be ± 5%.

The total uncertainty (U) in a calculated parameter combines the systematic (B) and random (P) uncertainties to maintain 95% confidence intervals according to ASME PTC Standard 19.1 [93]:

$$U = \sqrt{B^2 + P^2} \,. \tag{2.1}$$

The systematic uncertainty in a calculated parameter is determined from the errors propagated in the measured variables, and is mathematically expressed by [94]:

$$B = \sqrt{\sum_{1}^{n} \left(\frac{\partial F}{\partial \varphi_n} B_{\varphi_n} \right)^2} \,, \; F = f(\varphi_1, \varphi_2, \cdots, \varphi_n) \,. \tag{2.2}$$

The random uncertainty of a calculated parameter for a single test is estimated from:

$$P = t' \cdot SE \ , \tag{2.3}$$

for constant values, and,

$$P = t' \cdot SEE \, , \tag{2.4}$$

for data fitted to a trend line using a linear regression.

SE and SEE are the Standard Error (standard deviation of the mean) and Standard Error of Estimate, respectively, whereas t' is the Student distribution constant (t' is assumed to be 2 for 30 or more measurements at the 95% confidence interval).

2.5.3 Mass and energy balances

Mass and energy balances are performed to ensure the experiment conserves moisture and energy within the limits of experimental uncertainty for the tests conducted. To check conservation of mass for the air flow, a test is performed where the air flow rate is measured using rotameters installed in the upstream and downstream sections of the test facility. The measurements indicate no air leakage in the test facility within instrumentation uncertainty. Consequently, the mass flow rates of air in the upstream and downstream sections are considered to be equal, and only one rotameter is used for subsequent tests in order to avoid over-pressurization of the test facility.

To compute a mass balance for water (*i.e.* moisture balance), the quantity of water lost by the stagnant solution in the outer pipe of the LAMEE is compared to the quantity of water gained by the air stream. The quantity of water evaporated from the solution ($m_{w,sol}$) is determined from the difference in the mass of the LAMEE ($m_{LAMEE,i} - m_{LAMEE,f}$), which is measured before and after every test. The quantity of moisture gained by the air stream ($m_{w,air}$) is calculated from the sum of the product of the mass flow rate of air and the difference in the humidity ratio of inlet and outlet air streams over a test duration ($\sum_{0}^{t} \dot{m}_{air} \left(W_{air,out} - W_{air,in} \right) \Delta t$). The moisture balance (MB) is satisfied when MB is less than the uncertainty in the MB:

$$MB = \left| m_{w,sol} - m_{w,air} \right| = \left| \left[m_{LAMEE,i} - m_{LAMEE,f} \right] - \left[\sum_{0}^{t} \dot{m}_{air} \left(W_{air,out} - W_{air,in} \right) \Delta t \right] \right| \leq U_{MB} . \quad (2.5)$$

To compute an energy balance, the energy change in the solution is compared to the energy change in the air stream. The amount of energy change in the solution (q_{sol}) is calculated from the product of the mass of evaporated water and its latent heat of vaporization ($\left(m_{LAMEE,i} - m_{LAMEE,f} \right) h_{fg}$), whereas the quantity of energy change in the air stream (q_{air}) is determined from the sum of the product of the mass flow rate of air and the difference between the enthalpy of inlet and outlet air streams over a test duration ($\sum_{0}^{t} \dot{m}_{air} \left(h_{air,out} - h_{air,in} \right) \Delta t$). The energy balance (EB) is assessed by checking if the amount of energy exchanged between the solution and air satisfy:

$$EB = \left| q_{sol} - q_{air} \right| = \left| \left[\left(m_{LAMEE,i} - m_{LAMEE,f} \right) h_{fg} \right] - \left[\sum_{0}^{t} \dot{m}_{air} \left(h_{air,out} - h_{air,in} \right) \Delta t \right] \right| \leq U_{EB} . \quad (2.6)$$

The normalized moisture (MB^*) and energy (EB^*) balances are determined from:

$$MB^* = \frac{MB}{m_{w,sol}}, \quad (2.7)$$

$$EB^* = \frac{EB}{q_{sol}}. \quad (2.8)$$

Moisture and energy balances are assessed for a test performed with distilled H_2O(aq), and the results are given in Table 2.3.

Table 2.3. Assessment of the moisture and energy balances for a test conducted with air at 23 °C and RH_{air} = 10%, and distilled H_2O(aq) at 23 °C.

Moisture		**Energy**	
MB [g]	0.3	EB [kJ]	0.4
U_{MB} [g]	5.2	U_{EB} [kJ]	13.9
MB^* [%]	10.0	EB^* [%]	4.9

The amount of moisture and energy transferred between the solution and air streams are compared for several operating conditions, and the results are shown in Figure 2.3.

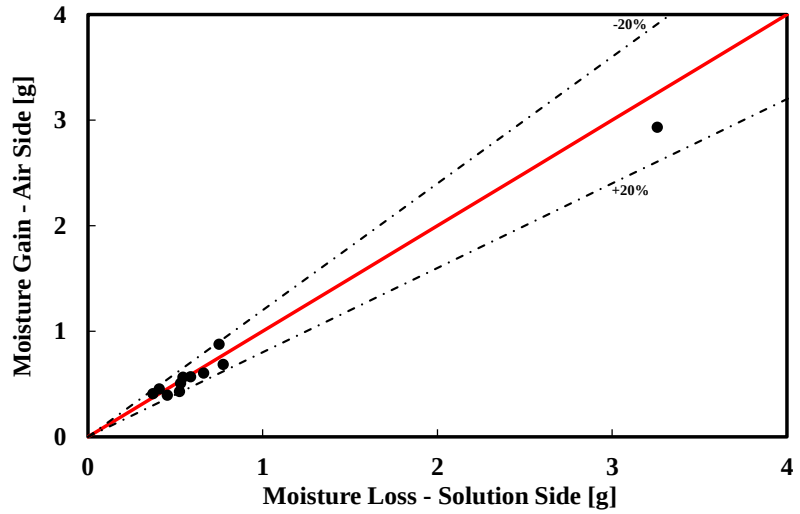

(a) Moisture balance.

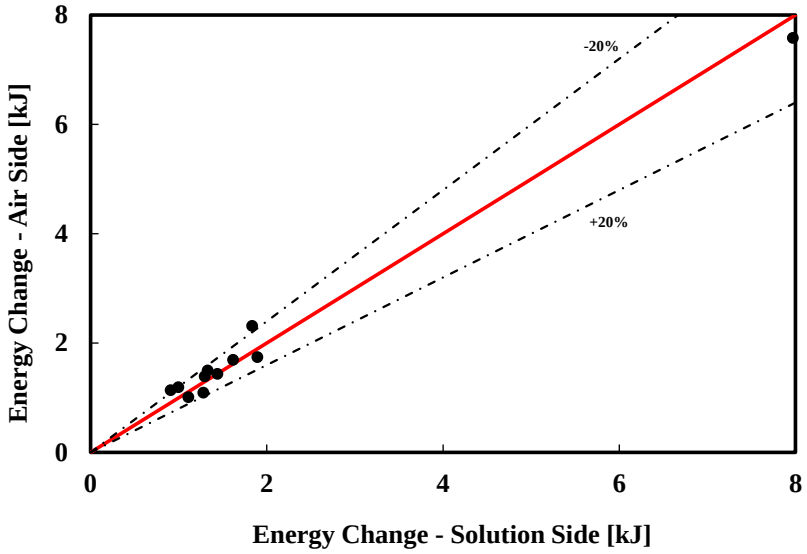

(b) Energy balance.

Figure 2.3 Comparison of the (**a**) moisture and (**b**) energy balances for air and $MgCl_2$(aq). **Note**. The data points at the extreme right of Figure 2.3(**a** and **b**) are for a test performed using distilled H_2O(aq).

Figure 2.3 shows that the discrepancies in the moisture and energy balances mostly lie within ±20%. In addition, the moisture and energy balances are less than their respective uncertainties, which indicates that all important moisture and energy flows are accounted for and properly measured.

2.6 DATA ANALYSIS

The two variables that are varied in the experimental tests conducted are the concentration of the desiccant solution and the relative humidity of air. The concentration of the liquid desiccant is varied in order to evaluate the role of bulk solution supersaturation, whereas the relative humidity of inlet air is changed in order to gauge the impact of moisture transfer rate on crystallization fouling in the LAMEE. The dimensionless solution concentration (C_{sol}^{*}), which is the ratio of the concentration of a solution to its saturation concentration at the same temperature, is given by:

$$C_{sol}^{*} = \frac{C_{sol}}{C_{sol,sat}}. \qquad (2.9)$$

The solution saturation concentration ($C_{sol,sat}$) is calculated using **Eq. (B.1)** in Appendix B.

Several tests are performed to dehydrate $MgCl_2$(aq) for roughly 12 h, and the test operating conditions are presented in Table 2.4.

Table 2.4. Test operating conditions.

Parameter and unit		**Values**
Relative humidity of air, RH_{air} [%]		10 ± 1, 20 ± 2, 30 ± 2
Dimensionless solution concentration, C_{sol}^{*} [-]	$MgCl_2$(aq)	~0.9 (unsaturated), ~1.0 (saturated), ~1.03 (supersaturated)
Temperature of air and desiccant solution [°C]		23 ± 2

The operating conditions studied in this thesis are extreme for LAMEEs operating in HVAC systems (*see* Table 2.4). However, these conditions are selected in order to accelerate the fouling tests. The concentration of $MgCl_2$(aq) is limited to C_{sol}^{*} = ~1.03 due to the difficulties associated with the measurement and estimation of the thermodynamic properties of highly supersaturated $MgCl_2$(aq), and preparation and preservation of stable and homogenous solution samples at high supersaturation levels.

2.6.1 Transient period

In this thesis, it is intended to study fouling under steady-state conditions. However, the boundary conditions (*i.e.* temperature and humidity ratio) of the desiccant solution at the solution-membrane interface are in a transient state at the beginning of a test. Figure 2.4 shows the transients response of the temperature and humidity ratio of the liquid desiccant solution at the start of a typical test.

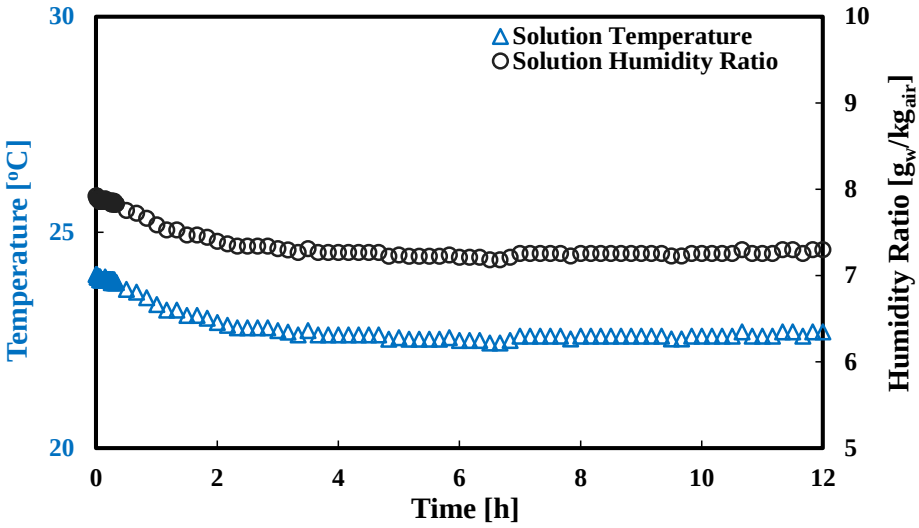

Figure 2.4. Temperature of $MgCl_2$(aq) (C_{sol}^* = 0.9) desiccant solution and humidity ratio of air in equilibrium with the desiccant solution at the solution-membrane interface during a test with RH_{air} = 20%. **Note**. Unit "h" refers to "hour" throughout the thesis; 1 h = 3600 s.

Figure 2.4 shows that temperature and humidity ratio of the liquid desiccant at the solution-membrane interface decrease at the start of a test. The observed decline in the solution properties can be explained by the latent heat of phase change associated with the evaporation of moisture at the solution-membrane interface. When the test commences, moisture is transferred from the liquid desiccant to the air stream through the membrane pores. Evaporative cooling occurs in the solution due to the latent heat of vaporization, which causes a gradual decline in the solution temperature until the heat transfer rate from the air stream to the liquid equals the rate of phase change energy required to evaporate water from the solution. A similar decay in the liquid temperature was reported during the transient portion of an experimental study on evaporative cooling in Ref. [95].

2.6.2 Indirect non-invasive parameter method

In this chapter, the impact of crystallization fouling on the LAMEE is assessed through indirect measurements of a non-invasive parameter method (*i.e.* moisture transfer flux). The moisture transfer flux is the rate of moisture transfer from the solution to the air per unit surface area of the membrane, and is estimated as follows:

$$\dot{m}_v'' = \frac{\dot{m}_{air}\left(W_{air,out} - W_{air,in}\right)}{A_{mem}}. \qquad (2.10)$$

The moisture transfer flux is normalized using the following expression:

$$M^{*} = \frac{\dot{m}''_{v}}{\dot{m}''_{v,o}}, \qquad (2.11)$$

where $\dot{m}''_{v,o}$ is the moisture transfer flux when an experiment reaches steady-state conditions. The steady-state conditions will be defined in Section 2.6.3.

Figure 2.5 shows that the moisture transfer flux changes during the 12-h test and the greatest change is during the transient period at the beginning of the experiment.

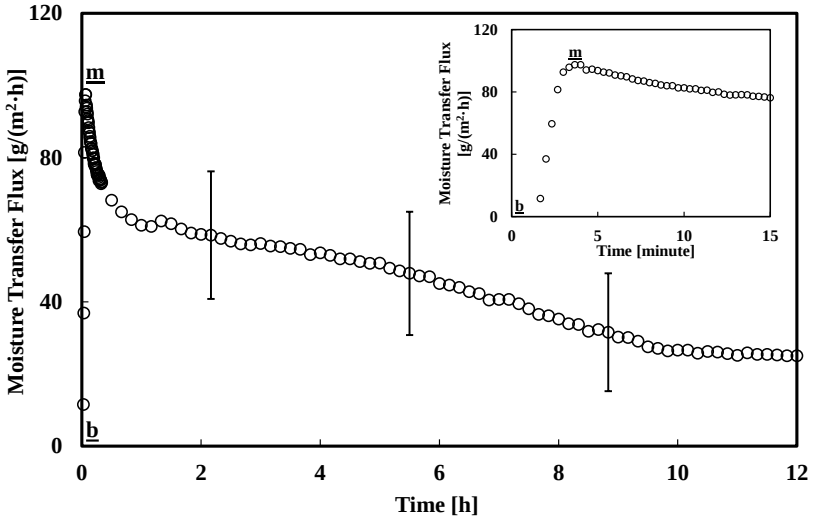

Figure 2.5. Moisture transfer flux as a function of time during a test with $MgCl_2$(aq) (C_{sol}^{*} = 1.03) at RH_{air} = 10%. **Note**. The transients at the start of the test are shown in the inset plot. The beginning (**b**) and maximum (**m**) points are indicated in Figure 2.5. The measurements are resolved at 10-minute intervals from 20 minutes after the beginning point (**b**) in order to reduce the quantity of data processed and the time needed for computation. Unit "g" refers to "gram" throughout the thesis; 1 g = 0.001 kg.

Figure 2.5 shows a rapid increase in moisture transfer flux at the beginning of a test (**b**) until a maximum point is reached (**m**). After the maximum point (**m**), the moisture transfer flux begins to decrease rapidly. The decline in moisture transfer flux after point (**m**) (Figure 2.5) is due to the decline in the solution temperature which results from evaporative cooling of the solution (Figure 2.4). A decline in the temperature of the solution leads to a decline in its equilibrium humidity ratio, and eventually results in a corresponding decline in the rate of moisture transfer through the membrane. This transient process continues until the air stream and liquid desiccant reach steady-state conditions.

Although it appears that the test does not reach steady state in Figure 2.5 because the moisture transfer flux continuously declines in the experiment, steady-state conditions may have actually been attained much earlier in the test. The start of the steady-state period of a test cannot be directly established by monitoring the moisture transfer flux because the transients in flux may arise from either a reduction in the temperature of the solution (due to evaporative cooling of the solution at the solution-membrane interface as explained in Section 2.6.1) or due to fouling of the membrane. Therefore, the critical task is to locate the point where the boundary conditions of the desiccant solution at the solution-membrane interface reach steady state during a test where fouling may or may not be taking place.

2.6.3 Steady state

The steady-state period of a test is defined as the period where the boundary conditions of the desiccant solution at the solution-membrane interface are at equilibrium. The start of the steady-state period is the start point for the steady-state data analysis. Figure 2.6 illustrates the steady-state period by comparing a $MgCl_{2(aq)}$ test with a control test that is performed using distilled $H_2O_{(aq)}$.

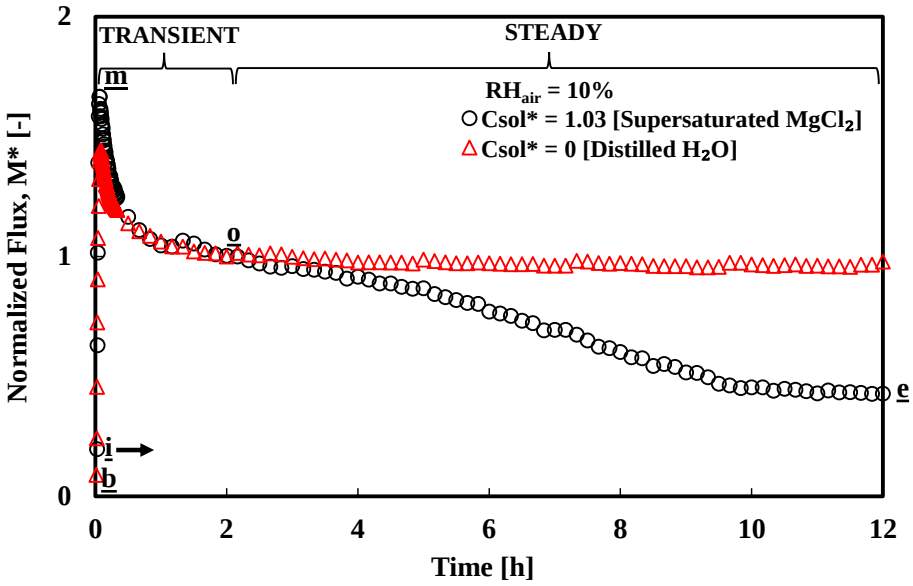

Figure 2.6. Moisture transfer flux as a function of time in a test with $MgCl_2$(aq) (C_{sol}^* = 1.03) at RH_{air} = 10%. **Note**. The beginning (**b**), moving (**i**), maximum (**m**), start of the steady-state period (**o**), and end (**e**) points are indicated in Figure 2.6. The moving point (**i**) is incremented in the moving window in the direction of the arrow. The normalized flux parameter is used in Figure 2.6 so as to compare the $MgCl_2$(aq) test with a control test using H_2O(aq).

Figure 2.6 shows that the control test performed with H_2O(aq) reaches steady-state conditions at a similar time as the $MgCl_2$(aq) test. However, unlike the test with $MgCl_2$(aq), the normalized moisture transfer flux is observed to remain constant at ~1 once the system reaches steady state in the test with H_2O(aq). This indicates that the system has reached steady state much earlier in the test with $MgCl_2$(aq) even though flux decline is continuous during the steady-state period.

In other words, the flux decline in the transient period ($MgCl_2$(aq) and H_2O(aq) tests) is caused by the transients of evaporative cooling at the start of the tests (*see* Section 2.6.1), whereas the flux decline in the steady-state period of the $MgCl_2$(aq) test is most likely caused by a different physical phenomenon such as fouling. It should be noted that fouling is a transient phenomenon and not a steady state process. In this thesis, steady state is exclusively used to describe the boundary conditions of the solution at the solution-membrane interface and not the process of fouling.

A moving window is created between a moving point (**i**) and the end point of the test (**e**) in Figure 2.6, in order to analyze the transient and steady-state periods of a test. The moving point (**i**) is incremented in the moving window from the beginning of the test (*i.e.* point (**b**) at t = 0 h) towards the end point (**e**) which is fixed at t = 12 h.

To establish that there is a transient period in a test, the difference in the solution humidity ratio between the maximum point (**m**), *i.e.* $W_{sol(m)}$, and a moving point (**i**), *i.e.* $W_{sol(i)}$, must exceed the systematic uncertainty in the solution humidity ratio at the moving point (**i**), *i.e.* $B_{W_{sol(i)}}$:

$$W_{sol(m)} - W_{sol(i)} > B_{W_{sol(i)}} . \qquad (2.12)$$

To determine the start point of the steady-state period, the moving point (**i**) is increased until the start of steady-state conditions (**o**) is located. Four criteria are used to estimate the start point of the steady-state period (**o**) of a test, and they are presented in Table 2.5.

Table 2.5. Comparison of the criteria used to estimate the start point of the steady-state period of a test with $MgCl_2$(aq) (C_{sol}^{*} = 1.03) at RH_{air} = 10%.

No	Criteria and description	Start point of the steady-state period	
		Time [h]	Moisture transfer flux [g/(m²·h)]
1	This criterion is satisfied when the solution humidity ratio at point (**i**) is within ±1 standard deviation ($\sigma_{W_{sol(i:e)}}$) of the average solution humidity ratio between a moving point (**i**) and the end point (**e**) ($\bar{W}_{sol(i:e)}$), as given by: $\bar{W}_{sol(i:e)} - \sigma_{W_{sol(i:e)}} \le W_{sol(i)} \le \bar{W}_{sol(i:e)} + \sigma_{W_{sol(i:e)}}$	2.7	56.0
2	This criterion is satisfied when the solution humidity ratio at point (**i**) is within ±2 standard deviations ($\sigma_{W_{sol(i:e)}}$) of the average solution humidity ratio between a moving point (**i**) and the end point (**e**) ($\bar{W}_{sol(i:e)}$), as given by: $\bar{W}_{sol(i:e)} - 2\sigma_{W_{sol(i:e)}} \le W_{sol(i)} \le \bar{W}_{sol(i:e)} + 2\sigma_{W_{sol(i:e)}}$	2.0	58.7
3	This criterion is satisfied when the normalized ratio of the difference between the solution humidity ratio at a moving point (**i**) and the average solution humidity ratio in the moving window (**i** – **e**) ($\bar{W}_{sol(i:e)} - W_{sol(i)}$) to the average solution humidity ratio in the moving window (**i** – **e**) ($\bar{W}_{sol(i:e)}$) is less than or equal to 1%: $\left\lvert \frac{\bar{W}_{sol(i:e)} - W_{sol(i)}}{\bar{W}_{sol(i:e)}} \right\rvert \le 1\%$	2.2	58.5
4	This criterion is satisfied when the ratio of the standard deviation ($\sigma_{W_{sol(i:e)}}$) to average ($\bar{W}_{sol(i:e)}$) solution humidity ratio between a moving point (**i**) and the end point (**e**) is less than or equal to 1%: $\frac{\sigma_{W_{sol(i:e)}}}{\bar{W}_{sol(i:e)}} \le 1\%$	2.0	58.7

The second and third criteria in Table 2.5 typically yield similar results for the start point of the steady-state period (**o**) of a test, and the criterion that yields the corresponding maximum time is selected (*i.e.* the second criterion in Table 2.5). In addition, the second criterion is selected because it accounts for a 95% confidence interval. Table 2.5 shows that the start point of the steady-state period estimated using the four criteria are within a close range (*see* Figure 2.6 for point (**o**)). Furthermore, the maximum discrepancy in the moisture transfer flux at point (**o**) is less than 5% (Table 2.5). A similar comparison was performed for tests at other operating conditions and comparable findings were obtained. Consequently, it is reasonable to conclude that the proposed methodology for the estimation of the start point of the steady-state period of a test is correct and reliable.

2.6.4 Repeatability

The repeatability of the experimental measurements was assessed by performing three tests at the same operating condition. The profile of the moisture transfer flux for the tests are compared in Figure 2.7.

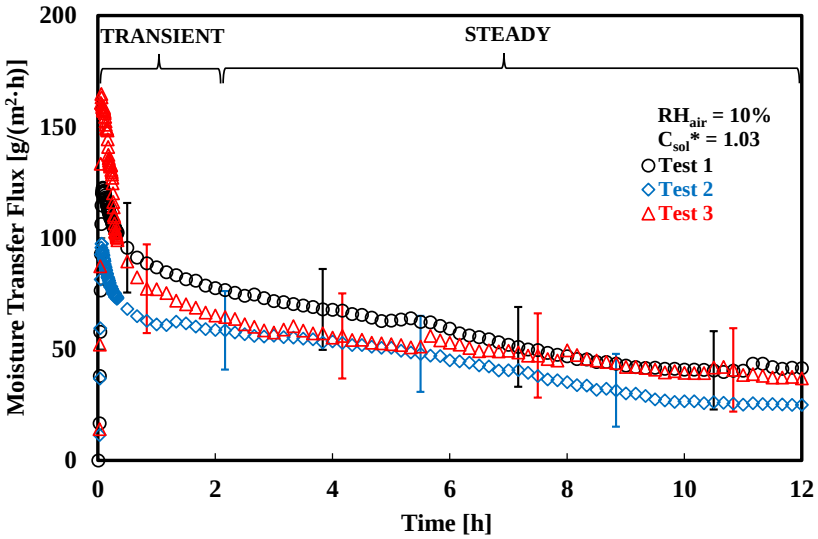

Figure 2.7. Moisture transfer flux as a function of time for three tests with $MgCl_2$(aq) (C_{sol}^* = 1.03) at RH_{air} = 10%. **Note**. The uncertainty bars are included for a few points for clarity.

Figure 2.7 shows that the tests have good repeatability since the moisture transfer flux for all tests agree within their uncertainty bounds. The uncertainty bars presented in Figure 2.7 include both systematic and random uncertainties for individual tests, and the details of the uncertainty analysis are presented in Section 2.5.2.

The repeatability of the fouling measurements is further assessed by fitting the data within the linear region of the steady-state period of the tests with a linear regression, as shown in Figure 2.8.

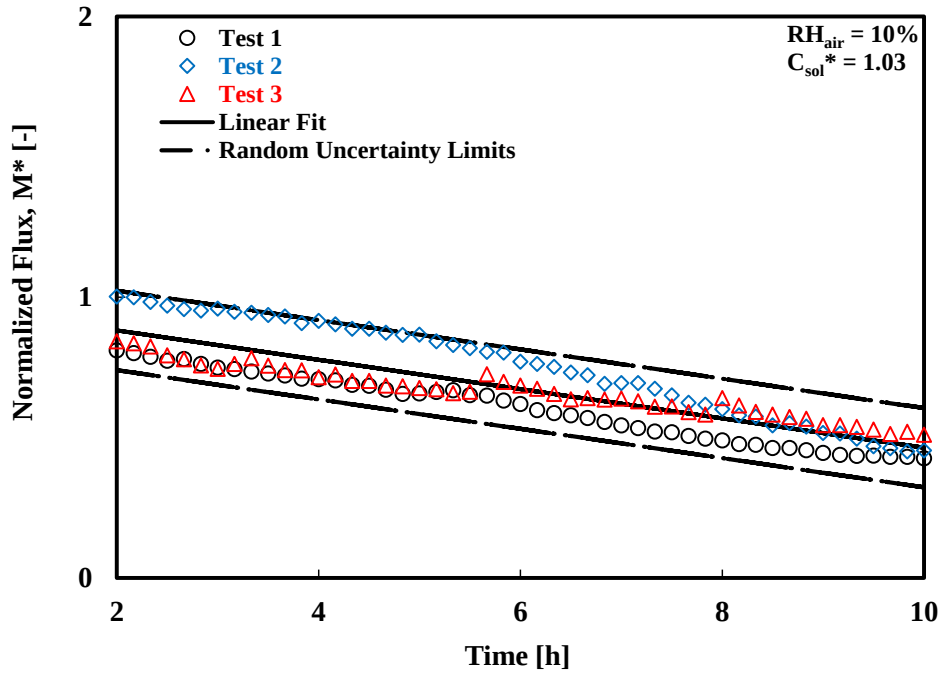

Figure 2.8. Normalized flux as a function of time for three tests with supersaturated $MgCl_2$(aq) (C_{sol}^* = 1.03) at RH_{air} = 10%.

The transient period of the tests are excluded from the regression model because the transient period in fouling tests is usually dominated by heat and mass transfer dynamics rather than fouling [69]. In addition, the transient period of fouling tests is typically excluded when assessing the repeatability of fouling in heat exchangers [69]. The test data in Figure 2.8 are limited to 10 h because the measurements begin to reach an asymptotic limit (*i.e.* flatten out) towards the end of the test.

The uncertainty bounds of the linear fit are determined by estimating the random uncertainty in the regression model at a 95% confidence interval. Figure 2.8 confirms that the tests have good repeatability since all the measurements lie within the uncertainty bounds of the linear fit.

2.6.5 Indirect non-invasive analysis methods

It is expected that the moisture transfer flux remains constant during a test without fouling. The occurrence of fouling in a test will reduce the quantity of fluid that permeates through a membrane, and this observation has been reported in previous studies (Refs. [26],[36],[80]). The decline in the rate of moisture transfer through a membrane may be caused by the formation and agglomeration of crystals within the pores of a membrane. Although a decline in the moisture transfer flux through a membrane may signify the occurrence of crystallization fouling in a LAMEE, a benchmark is needed to determine when the change in flux is large enough to confirm that fouling is occurring in the test. In this chapter, two indirect non-invasive analysis methods (an uncertainty analysis and a statistical test) are used to detect fouling in the LAMEE by evaluating the changes in an indirect non-invasive parameter method (*i.e.* moisture transfer flux).

2.6.5.1 Uncertainty method

The uncertainty method is used to examine the occurrence of crystallization fouling in a LAMEE by checking if the moisture transfer flux during the steady-state period of a test decreases by more than its corresponding uncertainty, as given by:

$$f_u = \left| \frac{\dot{m}''_v - \dot{m}''_{v,o}}{U_{\dot{m}''_v - \dot{m}''_{v,o}}} \right| > 1. \qquad (2.13)$$

The criterion that is used to detect fouling, f_u, is called a fouling detection parameter. The point at which **Eq. (2.13)** is first satisfied is named a fouling detection point, and is denoted by ($\underline{\mathbf{f}}_{\mathbf{u}}$) for the uncertainty method.

2.6.5.2 Statistical method

The occurrence of fouling in a test would result in a noticeable decline in the moisture transfer flux; thus, it is possible to check for fouling by comparing the moisture transfer flux between a test without fouling and a test where fouling is examined. A statistical method is developed to assess the difference between the means of two populations, *i.e.* a test without fouling versus a test where fouling is examined. A statistically significant difference between the means of the two populations confirms the occurrence of fouling, whereas a statistically insignificant difference

between the means of two populations rejects the occurrence of fouling. The two populations (Groups 1 and 2) for a test and their distribution are shown in Figure 2.9.

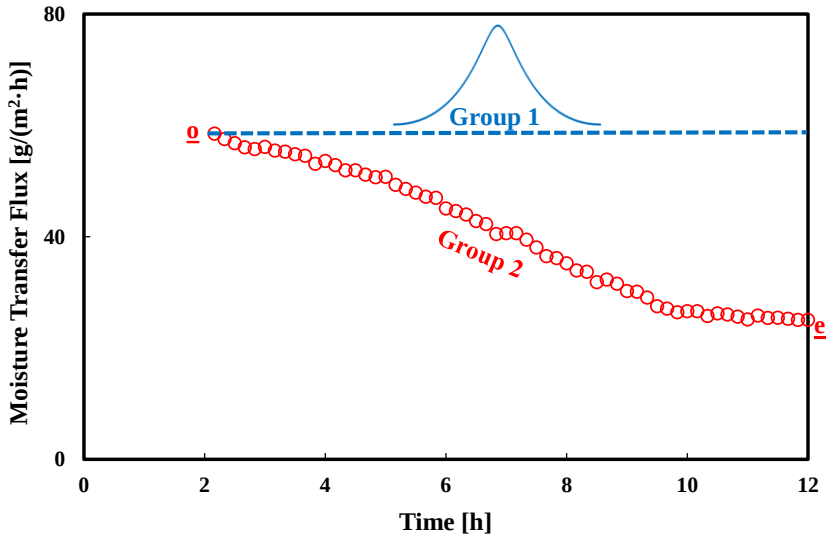

(a)

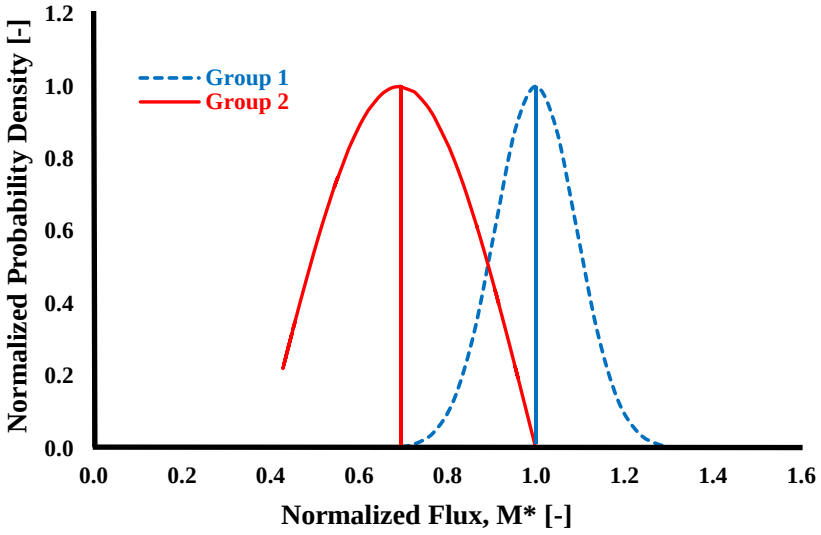

(b)

Figure 2.9. Moisture transfer flux as a function of time for a test with $MgCl_2$(aq) (C_{sol}^* = 1.03) at RH_{air} = 10%. **Note**. The populations and distributions of Groups 1 and 2 are shown in Figure 2.9(**a**) and (**b**), respectively. Group 1 is the test with H_2O(aq) where there is no fouling and Group 2 is the test group were fouling is tested. The start of the steady-state period (**o**) and end (**e**) points of the tests are indicated in Figure 2.9(**a**).

In Figure 2.9(**a**), the first population (Group 1) serves as the control group in which there is no fouling whereas the second population (Group 2) is the test group in which fouling is examined. Group 1 is populated by the estimated moisture transfer flux at the start point of the steady-state period (**o**). The standard deviation of Group 1 is calculated at six times of ~ ±1.5% of the moisture transfer flux at point (**o**). The value of ±1.5% is estimated from the standard deviation of moisture transfer flux for a test performed with distilled H_2O(aq). The standard deviation of Group 1 accounts for over a 99.99% confidence interval, and represents a worst-case random uncertainty for a test with no fouling. However, in Chapter 3 (Section 3.5.2.1.2), the standard deviation of Group 1 is calculated as two times of ~ ±1.5% of the moisture transfer flux in order to account for a 95% confidence interval which is more realistic. Group 2 consists of the moisture transfer flux during a test (**o** – **e**), and its average and standard deviation are calculated from the estimated moisture transfer flux during a test (**o** – **e**).

Figure 2.9(**b**) shows that fouling decreases the moisture transfer flux and shifts the distribution and mean of Group 2 leftwards from that of Group 1. A Welch's t-test is, therefore, used to statistically compare the means of Groups 1 and 2 in Figure 2.9(**a**). The null hypothesis for the t-test is that the difference between the statistical means of Groups 1 and 2 ($\overline{\dot{m}''_{v,Group\ 1}} - \overline{\dot{m}''_{v,Group\ 2}}$) is equivalent to the discrepancy in their standard deviations (d). The t-statistic ($t_{1\text{-}2}$) is calculated as follows [96]:

$$t_{1\text{-}2} = \frac{\left(\overline{\dot{m}''_{v,Group\ 1}} - \overline{\dot{m}''_{v,Group\ 2}}\right) - d}{\sqrt{\frac{\sigma^2_{\dot{m}''_{v,Group\ 1}}}{n_{Group\ 1}} + \frac{\sigma^2_{\dot{m}''_{v,Group\ 2}}}{n_{Group\ 2}}}}, \tag{2.14}$$

where the degree of freedom (df) is given by:

$$df = \frac{\left(\frac{\sigma^2_{\dot{m}''_{v,Group\ 1}}}{n_{Group\ 1}} + \frac{\sigma^2_{\dot{m}''_{v,Group\ 2}}}{n_{Group\ 2}}\right)^2}{\frac{\left(\frac{\sigma^2_{\dot{m}''_{v,Group\ 1}}}{n_{Group\ 1}}\right)^2}{n_{Group\ 1} - 1} + \frac{\left(\frac{\sigma^2_{\dot{m}''_{v,Group\ 2}}}{n_{Group\ 2}}\right)^2}{n_{Group\ 2} - 1}}, \tag{2.15}$$

and,

$$d = \left| \sigma_{\dot{m}''_{v,\text{Group 1}}} - \sigma_{\dot{m}''_{v,\text{Group 2}}} \right|. \tag{2.16}$$

Consequently, the null hypothesis is rejected if the t-test ($t_{1\text{-}2}$) exceeds the critical t-value at the corresponding degree of freedom and confidence interval ($t_{df,95\%}$), as given by the criterion for the statistical method (f_{st}):

$$f_{st} = \left(\left| t_{1\text{-}2} \right| - t_{df,95\%} \right) > 0. \tag{2.17}$$

On the other hand, the null hypothesis is accepted if the inequality in **Eq. (2.17)** is not satisfied. An acceptance of the null hypothesis indicates that fouling is not detected in a test, whereas a rejection of the null hypothesis confirms that fouling can be detected during a test.

For both the uncertainty and statistical methods, a moving window is used to conclude the onset of fouling for tests where fouling is confirmed. The start of the moving window is the start-point of the steady-state period (**o**) which is fixed, and the end of the moving window is incremented step-by-step from point (**o**) towards the end point (**e**) of the test. The point at which **Eq. (2.17)** is first satisfied is named a fouling detection point, and is denoted by (**f_{st}**) for the statistical method.

2.6.6 Asymptotic point of fouling

The asymptotic point of fouling is the point where there is no further change in the moisture transfer flux during a test. The literature suggests that crystallization fouling may exhibit an asymptotic growth regime [84]. Therefore, it is important to identify if there is an asymptotic point for a test where fouling occurs.

The asymptotic point of fouling is determined by implementing three steps. Firstly, the fouling detection points (**f_{st}**) and (**f_u**) are compared, and the point that corresponds to a greater value of time is selected. For the test at RH_{air} = 10% and C_{sol}^* = 1.03, point (**f_u**) has a greater value of time than point (**f_{st}**) (*see* Figure 2.11). Secondly, a linear fit is created by moving forwards from point (**f_u**) to the end point (**e**) of the test. Thirdly, the point that yields the maximum R^2 value of the linear

fit within the range (**f_u** – **e**) is selected as the asymptotic point (**a**). The profile of the R^2 value within the range (**f_u** – **e**) for a test is shown in Figure 2.10.

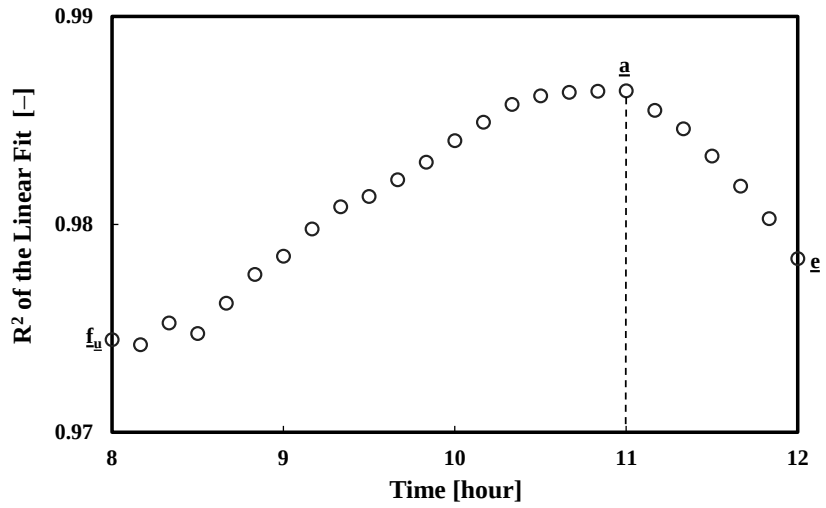

Figure 2.10. R^2 of the linear fit within the range (**f_u** – **e**) for a test with $MgCl_2$(aq) (C_{sol}^* = 1.03) at RH_{air} = 10%. **Note**. The point (**a**) with the maximum R^2 value is the asymptotic point.

Using the three steps described in this section, the asymptotic point is estimated to be at 11 h in a test with RH_{air} = 10% and C_{sol}^* = 1.03 (*see* Figure 2.10). The asymptotic point of fouling and other relevant points in the transient and steady-state periods are highlighted in Figure 2.11.

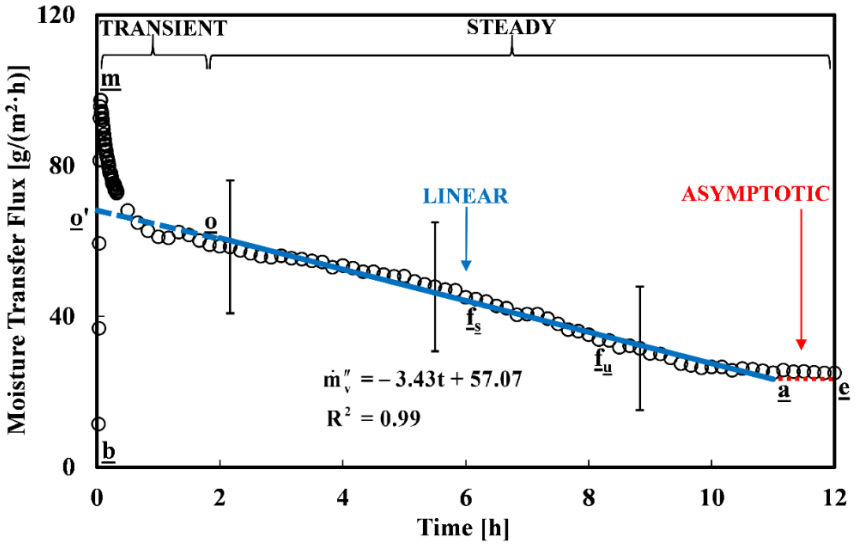

Figure 2.11. Moisture transfer flux as a function of time for a test with $MgCl_2$(aq) (C_{sol}^* = 1.03) at RH_{air} = 10%. **Note**. The beginning (**b**), extrapolation (**o'**), maximum (**m**), start of the steady-state period (**o**), fouling detection – statistical method (**f_{st}**), fouling detection – uncertainty method (**f_u**), asymptotic (**a**), and end (**e**) points are indicated in Figure 2.11.

Figure 2.11 shows the transient period, which consists of an initial rise in moisture transfer flux at the beginning of a test and subsequent decay until steady-state conditions are attained (**b** – **m** – **o**). During the steady-state period, the moisture transfer flux decays in a linear fashion until fouling is detected (**o** – $\mathbf{f_{st}}$ or **o** – $\mathbf{f_u}$) and reaches an asymptotic stage near the end (**a** – **e**).

2.6.7 Influence of the transient period of a test on fouling

It is important to determine the role of the transient period on a fouling test. The primary question to be answered is whether the transient period of a test could have initiated fouling that would not have occurred during the steady-state period of a test. To test this, it should be determined if fouling is more likely to have actually occurred in the transient period (**b** – **o**) or steady-state period (**o** – **e**).

The main change in the transient period is that the temperature of the solution decreases (concentration is constant). Since $MgCl_2$ is a normal soluble salt, cooling the solution in the transient period means that the risk of crystallization fouling increases as the test moves closer to the start of the steady-state period (**o**). Thus, fouling is more likely to occur during the steady-state period (**o** – **e**) rather than during the transient period (**b** – **o**). Consequently, it is reasonably assumed that the transient process itself does not trigger fouling.

It is also important to estimate the amount of fouling that would have happened during the transient period of a test. For this estimation, the fit for the linear decay in moisture transfer flux is extrapolated backwards to intercept the vertical axis, and the intercept is called the extrapolation point (**o'**) (*see* Figure 2.11). Generally, it is very unlikely that fouling occurred at the very start of the test, *i.e.* t = 0 h, without undergoing an induction period. Thus, this estimation would give a maximum amount of fouling in the transient period because it assumes no induction period, and the fouling rate will be higher in the steady-state period than in the transient period as previously described. The discrepancy between the moisture transfer flux at the start point of the steady-state period (**o**) and extrapolation point (**o'**), is estimated as follows:

$$\dot{m}''_{v,discrepancy} = \frac{\dot{m}''_{v,o'} - \dot{m}''_{v,o}}{\dot{m}''_{v,o}} \times 100\% . \qquad (2.18)$$

The discrepancy in moisture transfer flux yields ~20% for a test with the highest fouling risk (RH_{air} = 10% and C_{sol}^{*} = 1.03). This discrepancy may be considered small since it only accounts for ~25% of the total decay in moisture transfer flux for the entire test (**o'– e**). This indicates that the major portion (~80%) of the decline in moisture transfer flux is dominated by fouling in the steady-state period rather than the transient period. Thus, fouling in the transient period plays a negligible role compared to fouling in the steady-state period of the test.

2.7 RESULTS

The indirect non-invasive analysis methods presented in Section 2.6 are used to determine the occurrence and onset of fouling in the LAMEE at two test conditions, and the results are shown in Figure 2.12.

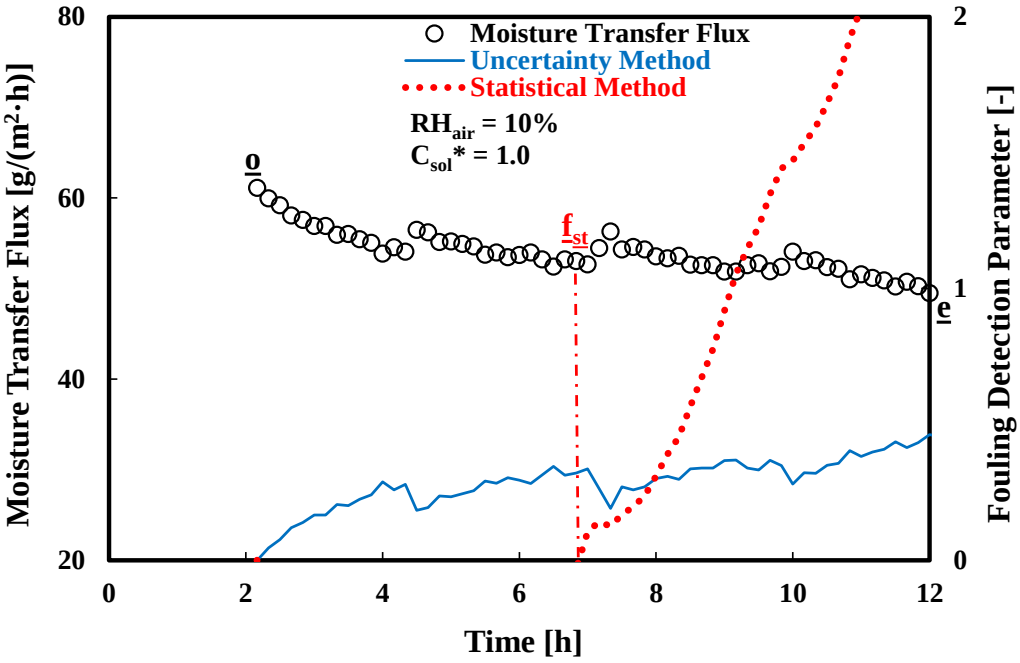

(a)

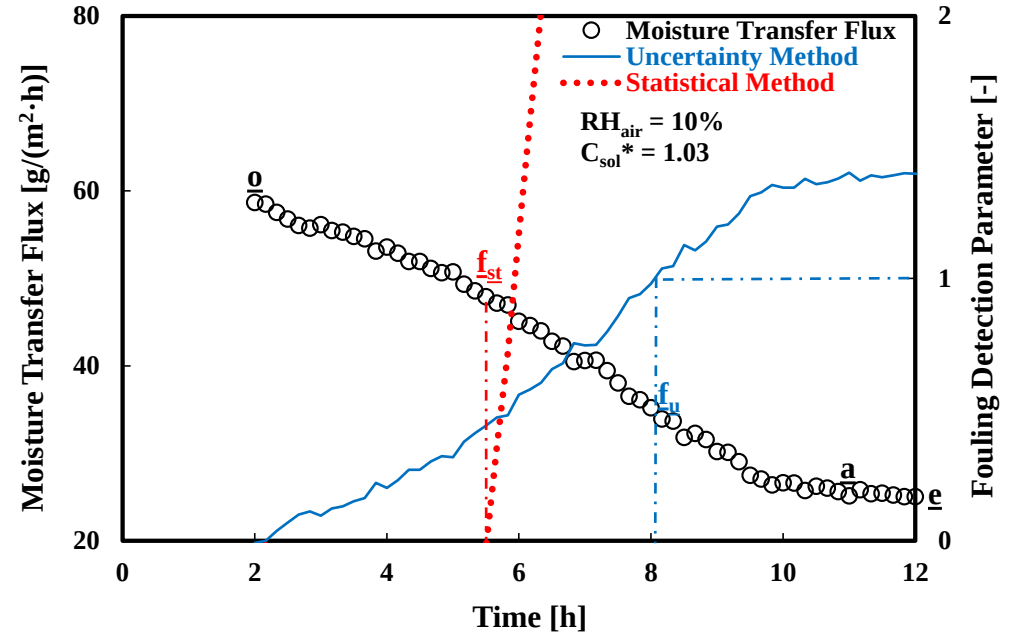

(b)

Figure 2.12. Comparison of moisture transfer flux and fouling detection parameter for two tests using $MgCl_2$(aq) with (**a**) RH_{air} = 10% and C_{sol}^* = 1.0 and (**b**) RH_{air} = 10% and C_{sol}^* = 1.03. **Note**. The start point of the steady-state period (**o**), fouling detection – statistical method (**f_{st}**), fouling detection – uncertainty method (**f_u**), asymptotic (**a**), and end (**e**) points are indicated in Figure 2.12. Fouling detection parameter refers to criteria f_u and f_{st} for the uncertainty and statistical methods, respectively.

The fouling detection parameter for the statistical method exceeds the value of 0 in Figure 2.12(**a**), which indicates that crystallization fouling was detected during the test. Although the continuous decay in moisture transfer flux in Figure 2.12(**a**) indicates the occurrence of fouling, the magnitude change in moisture transfer flux only accounts for 50% of the corresponding uncertainty in the change. Therefore, fouling cannot be concluded for this test using the uncertainty method. However, the statistical method is able to detect fouling in Figure 2.12(**a**) at ~6.8 h.

On the other hand, both the uncertainty and statistical methods are able to detect fouling in Figure 2.12(**b**). Figure 2.12(**b**) shows that the statistical method detects fouling at ~5.7 h whereas the uncertainty method detects fouling at ~8.2 h. The reason for the difference in the time that the onset of fouling is detected can be attributed to the fact that the statistical method is more sensitive to the changes in moisture transfer flux compared to the uncertainty method. Nevertheless, the sensitivity of both the uncertainty and statistical methods will be tuned in Chapter 3, by using a direct non-invasive method based on the observation of fouling using a microscope.

Figure 2.12(**a**) and (**b**) show that the moisture transfer flux decays by ~20% and ~60%, respectively, during the tests. The underlying physics that explains the decay in moisture transfer flux that is observed in Figure 2.12(**a**) and (**b**) is described as follows. As evaporation occurs on the solution side of the LAMEE, moisture is transferred from the liquid desiccant to the air, and results in an increase in the concentration of the liquid desiccant at the solution-membrane interface. The continuous evaporation of water from the liquid desiccant accelerates the nucleation of crystals that deposit or accumulate on the membrane, and thereby limits the amount of moisture that permeates through the membrane.

The indirect non-invasive analysis methods are also used to examine the occurrence of fouling in the LAMEE at other operating conditions, and both the uncertainty and statistical methods are in agreement, except for the test at RH_{air} = 10% and C_{sol}^{*} = 1.0 (Figure 2.12**a**). The results of the examination of fouling in the LAMEE at various operating conditions is shown in Figure 2.13.

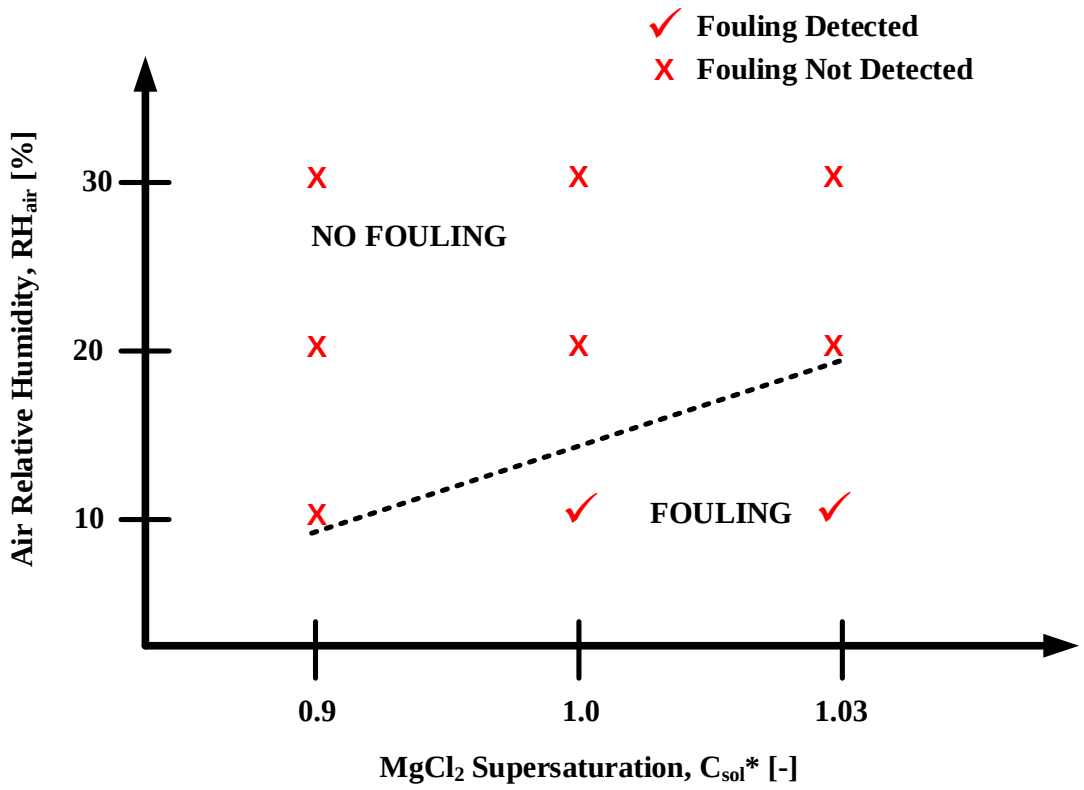

Figure 2.13. Results of the examination of fouling in the LAMEE at various operating conditions.

Figure 2.13 shows that the solution concentration (degree of supersaturation of a bulk solution) impacts the occurrence of crystallization fouling in the LAMEE. Fouling is not detected in the LAMEE when the concentration of the liquid desiccant is below saturation, irrespective of the air relative humidity.

Additionally, Figure 2.13 shows that the relative humidity of air impacts the occurrence of fouling in the LAMEE. Fouling is not detected in the LAMEE when the relative humidity of air is above 10%, even if the solution is at supersaturated conditions. This suggests that even when the bulk solution is slightly supersaturated, crystallization fouling may not be detected in the LAMEE because of the reduced potential for moisture transfer as the humidity of the air increases.

2.7.1 Effect of the supersaturation of the bulk solution

A comparison of the moisture transfer flux at the start point of the steady-state period for tests with $MgCl_2$(aq) at RH_{air} = 10% is presented in Figure 2.14.

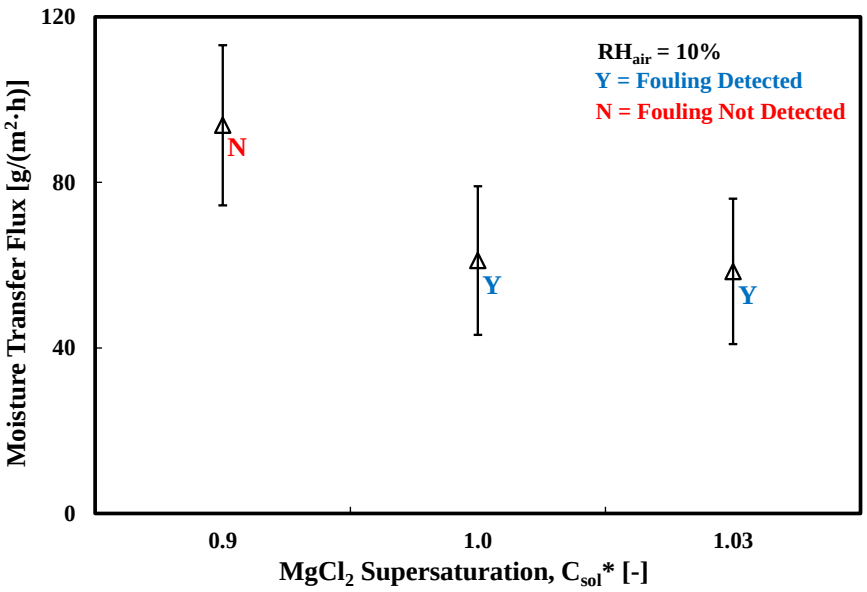

Figure 2.14. Comparison of moisture transfer flux at the start of the steady-state period for tests performed with $MgCl_2$(aq) at RH_{air} = 10% and various solution concentrations (C_{sol}^* = 0.9, 1.0, and 1.03).

Figure 2.14 shows that the moisture transfer flux reduces from 94 g/(m^2·h) to 61 g/(m^2·h) and 58 g/(m^2·h) for C_{sol}^* = 0.9, 1.0, and 1.03, respectively. This indicates that the reduction in moisture transfer flux between the tests C_{sol}^* = 0.9 versus 1.0 and C_{sol}^* = 0.9 versus 1.03 represents a decline of ~35% and ~38%, respectively. The decline in moisture transfer flux can be attributed to a reduction in the vapor pressure of the solution as its concentration is increased, which results in a decline in the potential for moisture transfer through the membrane.

Figure 2.14 shows that fouling is only detected at C_{sol}^* = 1.0 and C_{sol}^* = 1.03, which suggests that the solution concentration plays a key role in the formation of fouling. A supersaturated solution (C_{sol}^* = 1.03) increases the propensity for bulk crystallization in the liquid desiccant, which can accelerate the development of fouling in the membrane. In addition, the fact that fouling is detected at C_{sol}^* = 1.0 indicates that crystallization fouling can be initiated in a LAMEE even if the bulk solution concentration is not supersaturated, provided the evaporation rate is sufficient to create supersaturation at the solution interface. The results obtained are consistent with the theory which stipulates that supersaturation (in the bulk solution or at the solution interface) is a prerequisite for the occurrence of crystallization.

2.7.2 Effect of the relative humidity of air

A comparison of the moisture transfer flux at the start point of the steady-state period for tests performed with $MgCl_2$(aq) with C_{sol}^* = 1.03 is shown in Figure 2.15.

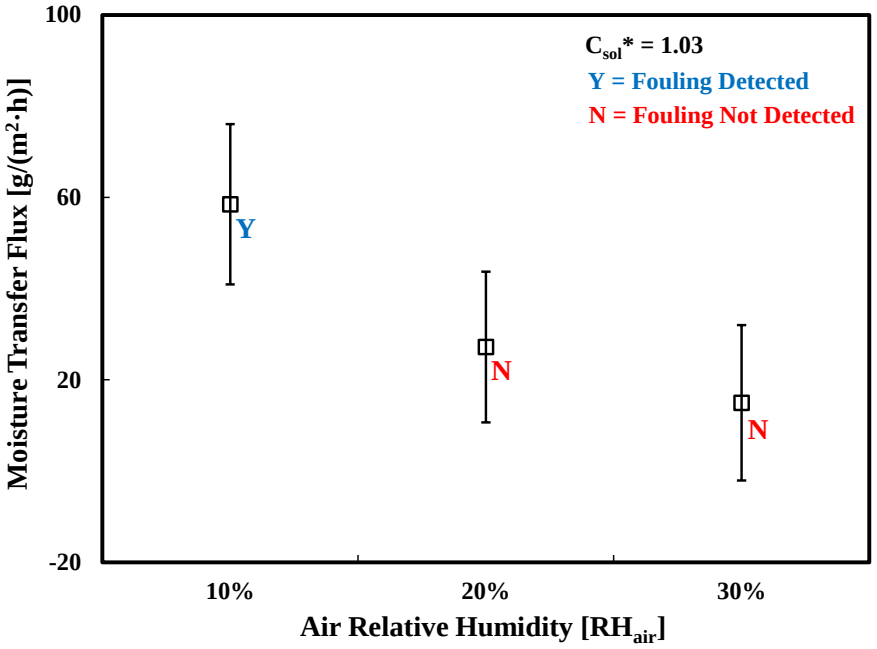

Figure 2.15. Comparison of moisture transfer flux at the start point of the steady-state period for tests with $MgCl_2$(aq) (C_{sol}^* = 1.03) at various relative humidity of air (RH_{air} = 10%, 20% and 30%).

Figure 2.15 shows that the moisture transfer flux for the tests at RH_{air} = 10%, 20% and 30% are 58 g/(m^2·h), 27 g/(m^2·h) and 15 g/(m^2·h), respectively. A possible reason why fouling is only detected at RH_{air} = 10% is explained as follows. The potential for moisture transfer between the air and desiccant solution is highest for air at RH_{air} = 10% versus 20% and 30%. The high potential for moisture transfer at RH_{air} = 10% creates a high evaporation rate which is sufficient to initiate the precipitation and growth of crystals. On the other hand, lower evaporation rates through the membrane at RH_{air} = 20% and 30% may not provide sufficient increase in the solution concentration to initiate the seeding of crystals.

2.7.3 Impact of moisture transfer rate on crystallization fouling in the LAMEE

A comparison of the moisture transfer flux for tests with $MgCl_2$(aq) with C_{sol}^* = 1.03 is shown in Figure 2.16.

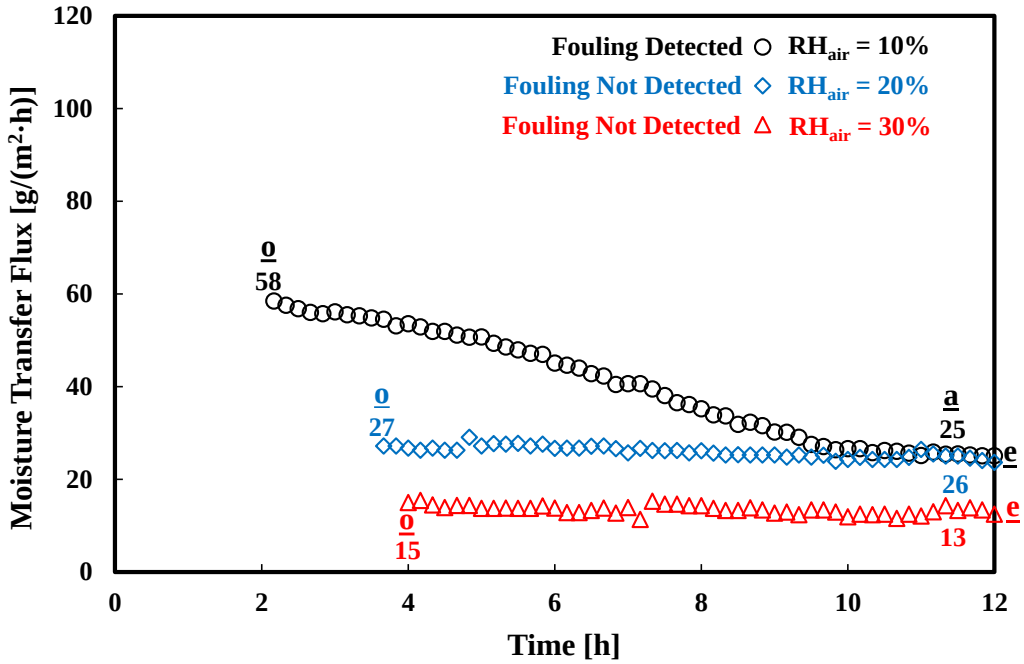

Figure 2.16. Comparison of moisture transfer flux for tests with $MgCl_2$(aq) (C_{sol}^* = 1.03) at various relative humidity of air (RH_{air} = 10%, 20% and 30%).

Figure 2.16 shows that the moisture transfer flux reduces by ~57% within the steady-state period at RH_{air} = 10%, whereas the reduction in moisture transfer flux is less than 15% for both RH_{air} = 20% and 30%, respectively. Although the moisture transfer flux is two times higher at the start of the test for RH_{air} = 10% compared to RH_{air} = 20%, the higher evaporation rate at RH_{air} = 10% may have initiated fouling in the membrane to such an extent that the moisture transfer flux reduces to the same value as the test for RH_{air} = 20% within the steady-state period (25 – 26 g/(m^2·h)). In other words, fouling caused the long term moisture transfer flux to be the same for both RH_{air} = 10% and 20% tests.

Although the results in Figure 2.16 establish that fouling is only detected at RH_{air} = 10%, this is not a definite conclusion that fouling is absent in the tests with RH_{air} = 20% and 30%. On the contrary, Figure 2.16 indicates that the higher relative humidity of air in the tests with RH_{air} = 20% and 30% lowered the moisture transfer flux to such an extent that it falls below the detection limit of the uncertainty and statistical methods.

This finding confirms the fact that reducing the moisture transfer rate through the membrane can reduce crystallization fouling in the LAMEE (*see* Section 2.4). However, this hypothesis only

holds when the moisture transfer rate is reduced for a solution at a specific concentration. This is an important finding which implies that operating the LAMEE at conditions that produce significantly high moisture transfer rates should be avoided, because of the possibility of initiating crystallization fouling within the membrane over time. However, high evaporation rates mean that the size of the LAMEE can be reduced. A design-stage optimization of the LAMEE is therefore recommended in order to estimate the range of operating conditions that favor both high evaporation rates and low fouling potential.

2.8 CONCLUSION

In this chapter, a test facility is developed to detect crystallization fouling in a liquid-to-air membrane energy exchanger (LAMEE) which uses a $MgCl_2$(aq) desiccant. Two indirect non-invasive analysis methods are developed and applied to confirm or reject the occurrence of crystallization fouling in the LAMEE, and to determine the time when fouling can be confirmed during a test. The key findings are summarized as follows:

1. Crystallization fouling can be detected in a LAMEE using the methods implemented. Furthermore, fouling may degrade the performance of a LAMEE by reducing its moisture transfer flux by nearly 60%.
2. Crystallization fouling in the LAMEE may exhibit linear and asymptotic growth regions. For a 12-h test with a supersaturated solution, the moisture transfer flux decayed linearly and gradually approached an asymptotic point at about 11 h.
3. Crystallization fouling is dependent both on the supersaturation of the desiccant solution and the relative humidity of air.

An important contribution of this thesis (from this chapter) is the fact that reducing the evaporation rate through a membrane can lower the potential for crystallization fouling in a LAMEE. This will enable engineers to consider the optimal design parameters and operating conditions that ensure high moisture transfer rates and also reduce the risk of crystallization fouling in a LAMEE.

Finally, it is important to state that the two indirect non-invasive analysis methods presented in this chapter are unable to detect fouling in the LAMEE at most of the operating conditions tested. Nevertheless, the methods introduced in this chapter will be improved in Chapter 3.

CHAPTER 3

CALIBRATION OF INDIRECT NON-INVASIVE ANALYIS METHODS

3.1 OVERVIEW

This chapter continues the work presented in Chapter 2 towards meeting the first and second objectives of the thesis. This chapter expands the two indirect non-invasive analysis methods in Chapter 2 (uncertainty and statistical methods) to include a slope method, and the three indirect non-invasive analysis methods are used to detect the occurrence and onset of fouling by analyzing two indirect non-invasive parameter methods (*i.e.* moisture transfer flux and resistance). Furthermore, the impact of membrane resistance on crystallization fouling in a liquid-to-air membrane energy exchanger (LAMEE) is evaluated by using two different membranes. Finally, a direct non-invasive method (*i.e.* digital microscopy) is used to detect the onset of fouling in the LAMEE, and the results are subsequently used to calibrate the sensitivity of the three indirect non-invasive analysis methods.

The manuscript included in this chapter was submitted to Journal of Membrane Science. The first author (PhD student – Mr. Adesola O. Olufade) analyzed the experimental data and wrote the manuscript, and the second author (supervisor – Prof. Carey J. Simonson) reviewed the manuscript.

Development of Non-Invasive Methods to Detect the Onset of Crystallization Fouling in a Liquid-To-Air Membrane Energy Exchanger

(Submitted to Journal of Membrane Science in December 2017)

A.O. Olufade, C.J. Simonson

3.2 ABSTRACT

Liquid-to-air membrane energy exchangers (LAMEEs) use semi-permeable membranes and are designed to transfer heat and moisture between air and liquid streams in heating, ventilating, and air-conditioning (HVAC) systems. However, crystallization fouling in membranes is possible in practical HVAC applications, which may lead to severe degradation in the performance of LAMEEs.

The main aim of this chapter is to identify the onset of fouling in a LAMEE using a direct non-invasive method (*i.e.* digital microscopy), and to use the results to calibrate three indirect non-invasive analysis methods. The three indirect non-invasive analysis methods consist of uncertainty and statistical methods (which were presented in Chapter 2) and a slope method which is introduced in this chapter. The three indirect non-invasive analysis methods detect fouling by evaluating experimental measurements from two indirect non-invasive parameter methods (*i.e.* moisture transfer flux and resistance). Experimental tests are performed to dehydrate varying concentrations of $MgCl_2$(aq) desiccant solutions using two types of membrane.

The main contribution of this chapter is that the direct non-invasive method (*i.e.* digital microscopy) detects the onset of fouling earlier than the indirect non-invasive analysis methods by a factor of three to eight. Consequently, the results of the direct method are used to tune the indirect methods in order to increase the sensitivity of the indirect methods to detect fouling earlier. The results also show that the membrane with lower vapor diffusion resistance (VDR) produces a higher flux which leads to a higher tendency for fouling than the membrane with higher VDR.

3.3 INTRODUCTION

The motivation for studying fouling is already discussed in Chapter 1 (Section 1.1). In this chapter, the two research gaps of the thesis in Chapter 1 (Section 1.2.3) are partially addressed. The specific sub-research gaps of the thesis that are addressed in this chapter are 1(**a**), 1(**b**) and 2(**c**)

(*the research gaps of the thesis and their corresponding numbers are outlined in Chapter 1 (Section 1.2.3)*).

Research gap 1(**a**) is the lack of development and application of indirect non-invasive analysis methods to detect the onset of fouling in liquid-to-air membrane energy exchangers (LAMEEs). Although the literature review of research gap 1(**a**) has already been described in Chapter 1 (Section 1.2.1), the review broadly addressed the onset of fouling in exchangers, and membrane exchangers for heating, ventilating and air-conditioning (HVAC) applications were not specifically discussed. A brief review of the determination of the onset of fouling in membrane exchangers for HVAC applications will be presented in this chapter.

Out of the three studies on fouling in membrane-based HVAC systems (Refs. [25]–[27]), only one study (Ref. [26]) investigated the onset of fouling by using a direct non-invasive method (*i.e.* time-lapse photography). However, the camera used for imaging could only detect deposit particles within the resolution of the human eye, and the images were captured at a minimum of 1-h intervals. Thus, the critical time that fouling started could not be estimated due to the limitations of the implemented method.

Research gap 1(**b**) is the lack of calibration of indirect non-invasive analysis methods using a direct non-invasive method, and research gap 2(**c**) is the lack of assessment of the impact of membrane resistance on fouling in the LAMEE.

This chapter aims to meet a number of objectives in order to address the aforementioned research gaps. Objectives 1(**c**) and 2(**b**) of the thesis (which were addressed in Chapter 2) are further addressed in this chapter by refining the statistical method and introducing an indirect non-invasive analysis method (*i.e.* slope method) to identify the occurrence and onset of fouling in the LAMEE. The objectives of the thesis that are specifically addressed in this chapter are to (*the objectives of the thesis are presented in Chapter 1 (Figure 1.2)*):

1(**d**): Identify the onset of fouling in a LAMEE using a direct non-invasive method.

1(**e**): Calibrate the indirect non-invasive analysis methods using the direct non-invasive method.

2(**c**): Evaluate the impact of membrane resistance on fouling in a LAMEE.

3.4 TEST FACILITY

The test facility that was presented in Chapter 2 (Figure 2.2) is modified in this chapter. The key modification to the test facility is the addition of a digital microscope that is used to directly and non-invasively detect fouling. The revised schematic of the test facility is shown in Figure 3.1.

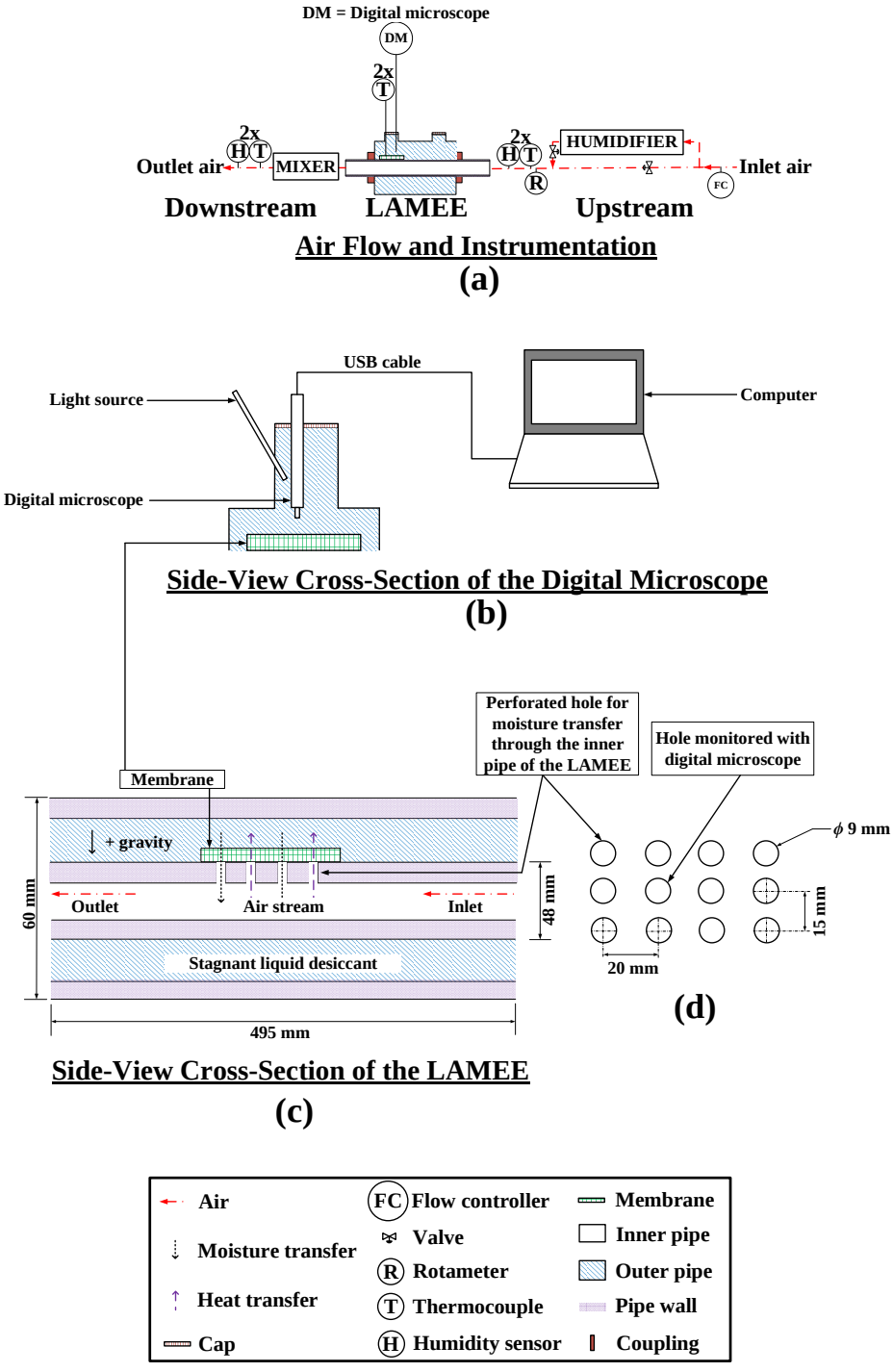

Figure 3.1. Schematic of the complete test facility. **Note**. The diagrams are not drawn to scale.

Figure 3.1 shows the test facility schematic which consists of (**a**) air flow and instrumentation, (**b**) digital microscope, (**c**) LAMEE, and (**d**) the top view of the holes perforated on the inner pipe of the LAMEE. In Figure 3.1(**a**), the mass flow rate and relative humidity of air are controlled in the upstream section before air is delivered to the LAMEE, whereas the air stream that exits the LAMEE is mixed to give the bulk properties of air at the outlet. Measurement sensors are installed to measure the properties of air at the inlet and outlet of the LAMEE. The sensors are calibrated before and after experimental testing. In addition, moisture and energy balances have been evaluated, and moisture and energy are confirmed to be conserved within the measurement uncertainties. The details of the test facility operation, instrumentation, uncertainty analysis, mass and energy balances, and repeatability have been presented in Chapter 2.

An addition to the test facility in this chapter (compared to Chapter 2) is that a digital microscope is set up to directly observe crystallization fouling in membranes (*see* Figure 3.1**b**). The microscope is positioned orthogonally to the LAMEE to focus on a membrane section that is about 530 mm from the inlet of the LAMEE, and approximately 55 mm below the lens of the microscope. The microscope can capture real-time video and still photographs with a resolution of 640 × 480 pixels, and has a built-in digital signal processing module which transmit images to a computer for subsequent image processing. A light source with negligible heating is installed to illuminate the membrane section under the view of the microscope, in order to improve the image contrast and clarity. Since the experiment begins as soon as the LAMEE is assembled as described in Chapter 2 (Section 2.5.1), it is not possible to take an image at the very start of the test. Rather, the microscope needs to be positioned and focused during the test, and the first image is taken at 15 minutes from the beginning of a test. Thereafter, images are taken at 10-minute intervals for a test performed at a high fouling rate, and at 15-minute intervals for a test performed at a low fouling rate.

In this chapter, two membranes are tested in the LAMEE, and their specifications are given in Table 3.1.

Table 3.1. Specifications of the membranes used in the LAMEE.

Parameter and unit	**Membrane A** [86]	**Membrane B** [97]
Material [-]	ePTFE laminates	ePTFE surface and PP support
Pore size [μm]	0.3	0.2
Porosity [%]	85	Not reported
Vapor diffusion resistance [s/m]	97 ± 11	23 ± 5
Thickness [mm]	0.540 ± 0.016	0.13 – 0.20
Liquid penetration pressure [kPa]	>82	>345

Note. ePTFE = Expanded Polytetrafluoroethylene; PP = Polypropylene.

Membrane A was previously tested in Chapter 2 (Table 2.1). On the other hand, Membrane B has not been previously tested in the LAMEE but has a lower vapor diffusion resistance (VDR) than Membrane A. Thus, Membrane B is a potential candidate for future prototypes of the LAMEE.

3.5 METHODOLOGY

Experiments are performed to dehydrate $MgCl_2$(aq) desiccant solution in tests that last for roughly 12 h, and the details of the test conditions have been presented in Chapter 2 (Table 2.4). In this section, the indirect non-invasive parameter methods that are used to assess the effect of fouling on the performance of the LAMEE are first presented (Section 3.5.1); thereafter, the indirect non-invasive analysis methods that are used to evaluate the indirect non-invasive parameter methods are discussed (Section 3.5.2).

3.5.1 Indirect non-invasive parameter methods

In this chapter, the impact of fouling on the LAMEE is assessed using two indirect performance parameter methods. The first parameter method is the moisture transfer flux which has been presented in Chapter 2 (Section 2.6.2). The second parameter method, which is introduced in this chapter, is the moisture transfer resistance of the LAMEE. Although up to 8 parameters have been previously used to evaluate the performance of LAMEEs [92],[98],[99], moisture transfer flux and resistance are implemented in this thesis because they are well-suited to characterize fouling as evidenced by their wide adoption in the literature (*see* Refs. [36],[43],[46],[48],[69],[80],[100]) and are familiar to engineers in the industry.

3.5.1.1 Moisture transfer flux

As presented in Chapter 2 (Section 2.6.2), the moisture transfer flux is defined as the amount of water vapor transferred from the desiccant solution to the air stream per unit surface area of the membrane, as given by

$$\dot{m}''_v = \frac{\dot{m}_{air}\left(W_{air,out} - W_{air,in}\right)}{A_{mem}}. \tag{3.1}$$

The moisture transfer flux is normalized as follows:

$$M^* = \frac{\dot{m}''_v}{\dot{m}''_{v,o}}. \tag{3.2}$$

The instantaneous moisture transfer flux is denoted by $\dot{m}''_v$, and $\dot{m}''_{v,o}$ is the moisture transfer flux immediately after the transient startup and at the start of the steady-state period. The start of the steady-state period of a test is defined as when the boundary conditions of the solution at the solution-membrane interface are constant. The analysis method that is used to determine the steady-state period of a test has been explained in Chapter 2 (Section 2.6.3).

3.5.1.2 Moisture transfer resistance

The resistance circuits and schematics of the LAMEE without and with fouling are shown in Figure 3.2.

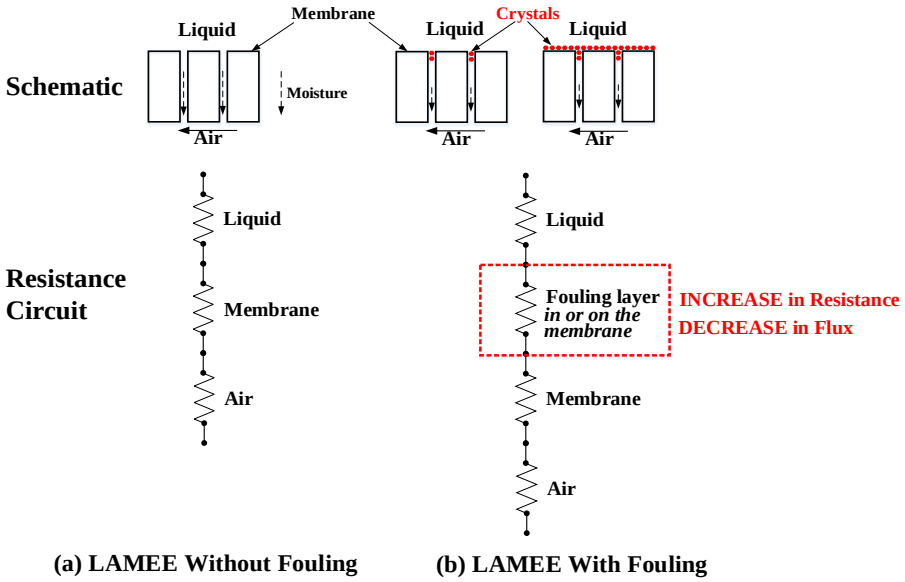

Figure 3.2. Schematic and resistance circuit of a LAMEE (**a**) without and (**b**) with fouling.

Figure 3.2(**a**) shows the transfer of moisture from the liquid desiccant to the air stream through the membrane pores. The solution concentration at the solution-membrane interface will increase as moisture evaporates from the liquid desiccant. This may lead to localized supersaturation at the solution-membrane interface or suspended particles in the solution may transport and attach to the membrane surface. The growth of crystals can occur within the membrane pores (internal fouling) or in the form of a cake layer on the membrane surface (external fouling) (Figure 3.2**b**).

Figure 3.2 also depicts the development of fouling in a LAMEE using resistance circuits. Figure 3.2(**a**) shows the component resistances of a LAMEE (*i.e.* air-side, membrane and liquid-side resistances) when there is no fouling. If fouling occurs during a test, the growth of crystals in the membrane would constitute an additional resistance, *i.e.* fouling resistance (Figure 3.2**b**). The fouling resistance may eventually limit the rate of moisture transfer from the desiccant solution to the air stream, and increase the moisture transfer resistance of the LAMEE.

The moisture transfer resistance of the LAMEE represents the total resistance to moisture transfer between the desiccant solution and air stream, as given by

$$R = \frac{\Delta W_{lm}}{\dot{m}''_v}. \tag{3.3}$$

The log-mean humidity ratio, ΔW_{lm}, is given by

$$\Delta W_{lm} = \frac{\left(W_{sol} - W_{air,in}\right) - \left(W_{sol} - W_{air,out}\right)}{\ln\left(\frac{W_{sol} - W_{air,in}}{W_{sol} - W_{air,out}}\right)}. \tag{3.4}$$

The moisture transfer resistance of the LAMEE (R) is normalized by the resistance of the LAMEE at the start of the steady-state period (R_o) as follows:

$$R^* = \frac{R}{R_o}. \tag{3.5}$$

3.5.1.3 Performance of a LAMEE

The performance of a LAMEE is characterized using moisture transfer flux and resistance, as given in Figure 3.3.

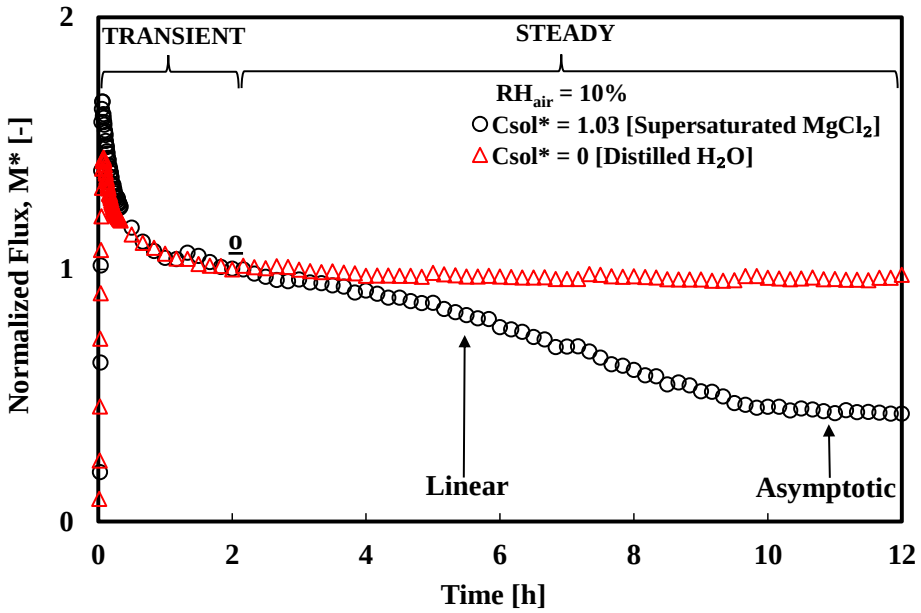

(a)

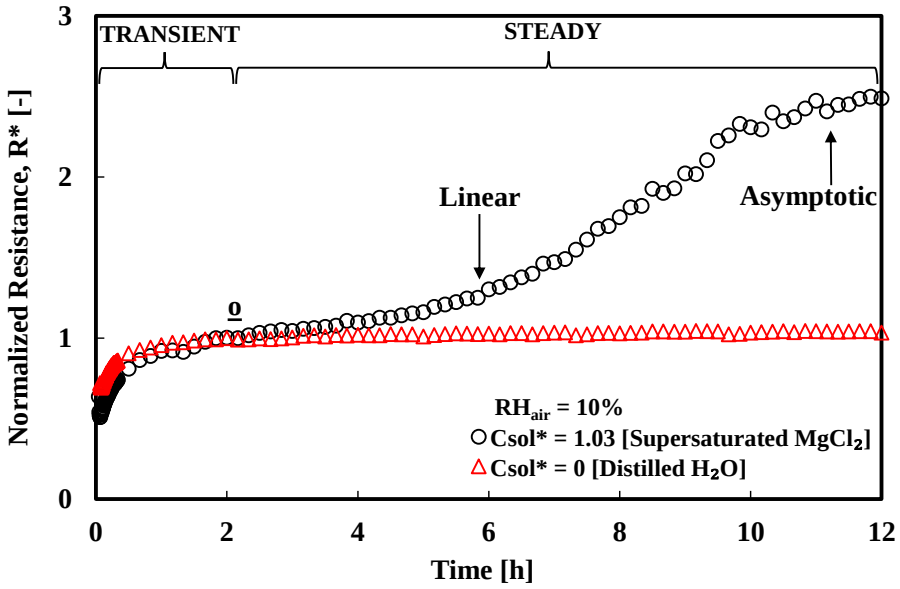

(b)

Figure 3.3. Performance of a LAMEE with normalized moisture transfer (**a**) flux and (**b**) resistance for tests using Membrane A with supersaturated $MgCl_2$(aq) (C_{sol}^* = 1.03) and distilled H_2O(aq) (C_{sol}^* = 0) at RH_{air} = 10%. **Note**. The start of the steady-state period of the tests is indicated by point (**o**).

Figure 3.3(**a**) shows a rapid increase in moisture transfer flux for the tests with supersaturated $MgCl_2$(aq) and distilled H_2O(aq). Thereafter, the flux peaks and decreases until the boundary conditions of the desiccant solution at the solution-membrane interface reach steady-state conditions. The test performed with distilled H_2O(aq) maintains an M^* value of ~1 during the steady-state period, whereas a significant decline (~60%) in flux is observed for the test performed with supersaturated $MgCl_2$(aq). The trends observed suggest that there is no fouling formation in the test with distilled H_2O(aq), whereas a rapid rate of crystallization fouling may have been initiated in the test with $MgCl_2$(aq) due to the fact that the bulk solution is supersaturated.

The normalized resistance of the LAMEE in the test is shown in Figure 3.3(**b**). For both tests ($MgCl_2$(aq) and distilled H_2O(aq)), the moisture transfer resistance increases during the transient period. The value of R^* is constant at ~1 during the steady-state period of the test with distilled H_2O(aq) as expected for the case of no fouling. On the other hand, the resistance rapidly increases by over a factor of 2 during the test with supersaturated $MgCl_2$(aq). The substantial increase in resistance in the test with $MgCl_2$(aq) can be attributed to the buildup of crystals in the membrane. The deposits impede moisture transfer through the membrane and increase the moisture transfer resistance of the LAMEE.

Figure 3.3 also shows that the steady-state period of the test with supersaturated $MgCl_2$(aq) features linear and asymptotic regions. This suggests that the deposition or accumulation of crystals on the membrane initially increased in a linear fashion; later in the test, crystals are likely gradually removed from the membrane surface until the rate of crystal removal becomes equal to the rate of deposition (asymptotic region). The determination of the transition point between the linear and asymptotic regions of the test has been described in Chapter 2 (Section 2.6.6).

3.5.2 Methods to detect the onset of fouling

In the previous section, Figure 3.3 shows that fouling is likely present in the LAMEE during the test with $MgCl_2$(aq). However, the time of fouling initiation is not known. Consequently, analysis methods are needed to find the time that fouling started in the test.

In this chapter, three indirect non-invasive analysis methods (uncertainty and statistical methods from Chapter 2, and a new method in this chapter which is called the slope method) will be used

to determine the onset of fouling in the LAMEE. Thereafter, the results of the indirect non-invasive analysis methods will be tuned using a direct non-invasive method. The direct non-invasive method is introduced in this chapter and is based on the direct observation of fouling with a digital microscope.

3.5.2.1 Indirect non-invasive analysis methods

Three indirect non-invasive analysis methods are used to evaluate two indirect non-invasive parameter methods (F) in this chapter, where F is either the moisture transfer flux ($\dot{m}''_v$) or moisture transfer resistance (R). It can be concluded that fouling exists if the change in an indirect parameter method exceeds a threshold limit, whereas fouling cannot be concluded if the change in the parameter is less than the threshold limit. The phenomenology and implementation of the uncertainty and analysis methods have been previously described in Chapter 2 (Sections 2.6.5.1 and 2.6.5.1, respectively), and the two methods will only be briefly presented in this chapter.

3.5.2.1.1 Uncertainty method

As described in Chapter 2 (Section 2.6.5.1), the uncertainty method is used to compare the difference between the value of an indirect non-invasive parameter method (F) at any time and the value at the start of the steady-state period (F_o) to the corresponding uncertainty in the change in that parameter (U_{F-Fo}) at 95% confidence. Mathematically, fouling exists if the following criterion is satisfied:

$$f_u = \left| \frac{F - F_o}{U_{F-F_o}} \right| > 1, \; F = \dot{m}''_v \text{ or } R. \tag{3.6}$$

The sensitivity of the uncertainty method can be increased by multiplying the ratio in **Eq. (3.6)** with a scale factor.

3.5.2.1.2 Statistical method

In accordance with the description given in Chapter 2 (Section 2.6.5.1), the statistical method is used to detect fouling by comparing the differences in an indirect non-invasive parameter method between a test where fouling is non-existent (control group – Group 1) versus a test where fouling

is being tested (test group – Group 2). The control group (test with H_2O(aq) which has no fouling) and test group (test with $MgCl_2$(aq)) make up two distinct populations which can be statistically compared. Fouling can be confirmed if there is a statistically significant difference between the means of the two populations, whereas fouling is rejected if there is a statistically insignificant difference between the means of the two populations. The populations of the test groups (Group 2) are shown in Figure 3.4.

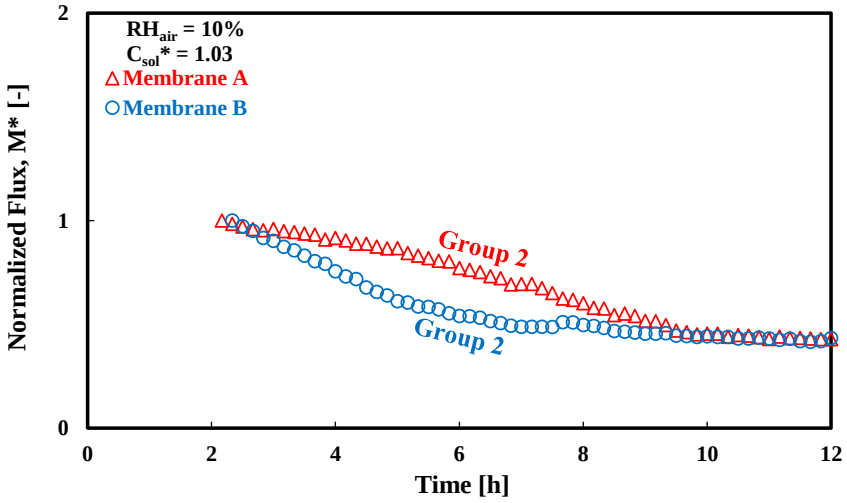

(a)

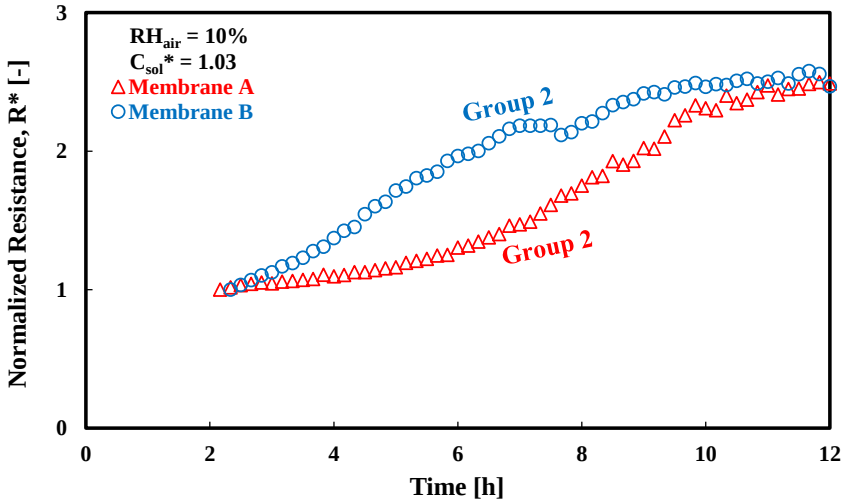

(b)

Figure 3.4. Plots of normalized moisture transfer (**a**) flux and (**b**) resistance as a function of time for tests using Membranes A and B with supersaturated $MgCl_2$(aq) (C_{sol}^* = 1.03) at RH_{air} = 10%. **Note**. Membranes A and B are the example test groups (*i.e.* Group 2) in Figure 3.4(**a** and **b**) where the test with H_2O(aq) (no fouling) serves as the control group (*i.e.* Group 1). The start of the steady-state period (**o**) and end (**e**) points of the tests are indicated in Figure 3.4.

Group 1 is populated by the moisture transfer flux or resistance at the start of the steady-state period of a test. The standard deviation of Group 1 is calculated as twice of the standard deviation of moisture transfer flux and resistance for a test performed with distilled H_2O(aq) to account for a 95% confidence interval. Therefore, the standard deviation of Group 1 is ±3.1% and ±2.0% of the moisture transfer flux and ±2.8% and ±1.0% of the moisture transfer resistance for Membranes A and B, respectively. Group 2 is populated by the measured values of the moisture transfer flux or resistance during a test, and its average and standard deviation are calculated from the measured indirect non-invasive parameters (*i.e.* moisture transfer flux or resistance).

A Welch's t-test ($t_{1\text{-}2}$) is used to compare the difference between the statistical means ($\bar{F}$) of Groups 1 and 2 ($\overline{F_{Group\ 1}} - \overline{F_{Group\ 2}}$) with the discrepancy in their standard deviations (d) [96]:

$$t_{1\text{-}2} = \frac{\left(\overline{F_{Group\ 1}} - \overline{F_{Group\ 2}}\right) - d}{\sqrt{\frac{\sigma^2_{F_{Group\ 1}}}{n_{Group\ 1}} + \frac{\sigma^2_{F_{Group\ 2}}}{n_{Group\ 2}}}},\ F = \dot{m}''_v \text{ or } R. \tag{3.7}$$

The degree of freedom (df) is given by

$$df = \frac{\left(\frac{\sigma^2_{F_{Group\ 1}}}{n_{Group\ 1}} + \frac{\sigma^2_{F_{Group\ 2}}}{n_{Group\ 2}}\right)^2}{\frac{\left(\frac{\sigma^2_{F_{Group\ 1}}}{n_{Group\ 1}}\right)^2}{n_{Group\ 1} - 1} + \frac{\left(\frac{\sigma^2_{F_{Group\ 2}}}{n_{Group\ 2}}\right)^2}{n_{Group\ 2} - 1}}. \tag{3.8}$$

The discrepancy in the standard deviation (d) is estimated using

$$d = \left|\sigma_{F_{Group\ 1}} - \sigma_{F_{Group\ 2}}\right|. \tag{3.9}$$

The criterion that establishes the occurrence of fouling is given as follows:

$$f_{st} = \frac{|t_{1\text{-}2}|}{t_{df,95\%}} > 1. \tag{3.10}$$

Unlike in **Eq. (2.17)**, criterion f_{st} in **Eq. (3.10)** is expressed as a ratio so that the criteria of the three indirect non-invasive analysis methods will have a consistent value of 1. In addition, the sensitivity of the statistical method can be augmented by adjusting the confidence interval (95%) in **Eq. (3.10)**.

3.5.2.1.3 Slope method

If there is no fouling, the indirect non-invasive parameter method of a LAMEE will be constant during the steady-state period of a test and remain within its uncertainty limits. Thus, fouling can be detected by examining the rate of change (slope) of the parameter in the linear region of the steady-state period of a test. When the slope exceeds the uncertainty in the slope at a 95% confidence interval, the slope method concludes that fouling exists:

$$f_{sl} = \left| \frac{Slope_{F_o \rightarrow F}}{P_{Slope_{F_o \rightarrow F}}} \right| > 1, \quad F = \dot{m}''_v \text{ or } R. \tag{3.11}$$

The implementation of the slope method for an entire test is shown in Figure 3.5.

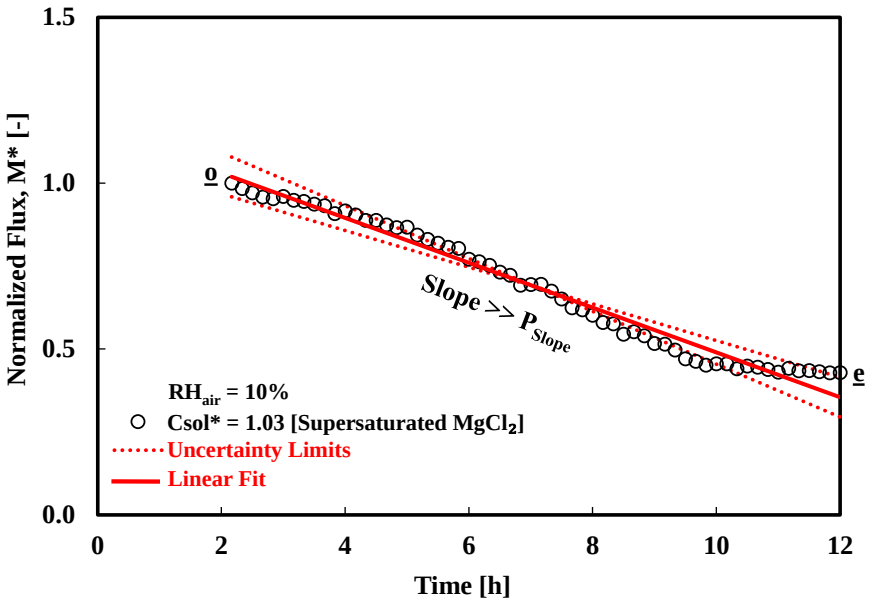

Figure 3.5. Application of the slope method to detect fouling in a test with Membrane A and supersaturated $MgCl_2$(aq) (C_{sol}^* = 1.03) at RH_{air} = 10%. The start of the steady-state period (**o**) and end (**e**) points of the tests are indicated in Figure 3.5.

Figure 3.5 shows that there is fouling in the test because the slope in moisture transfer flux exceeds its uncertainty. The slope method is implemented by first comparing the slope with the uncertainty in slope for the entire population of a test to confirm if there is fouling in a test. Afterwards, a moving window is used to detect the time that fouling started in a test where fouling is confirmed. The moving windows starts from the start of the steady-state period of a test (**o**), which is a fixed point, and the end of the moving window is extended from point (**o**) till the end point (**e**) of the test. Finally, it should be noted that the slope method can be made more sensitive by adjusting the confidence interval of the random uncertainty (95%) in the slope in **Eq. (3.11)**.

3.5.2.2 Direct non-invasive method

A direct non-invasive method that is based on digital microscopy is used to determine the onset of crystallization fouling in the LAMEE. Digital microscopy is a powerful technique that can be used to directly detect the onset of fouling on a membrane surface [67].

A digital microscope is used to monitor the membrane surface during experimental tests. Unlike the indirect non-invasive analysis methods that are used to assess fouling for all the test conditions presented in Chapter 2 (*see* Table 2.4) using Membranes A and B, the direct non-invasive method is used to observe fouling at only two of the test conditions in Table 2.4 using Membrane A. Table 3.2 presents the two test operating conditions.

Table 3.2. Test operating conditions (high and low fouling rates).

Parameter and unit	**Condition 1 (High fouling rate)**	**Condition 2 (Low fouling rate)**
Relative humidity of air, RH_{air} [%]	10 ± 1	30 ± 1
Dimensionless solution concentration, C_{sol}^{*} [-]	~1.03 (supersaturated)	~1.0 (saturated)
Temperature of air and desiccant solution [°C]	23 ± 1	

Note. Condition 1 has a higher fouling rate than Condition 2 because of its greater potential for moisture transfer (RH_{air} = 10% < 30%) and higher solution concentration (C_{sol}^{*} = 1.03 > 1.0).

The images from the digital microscope are analyzed using an image-processing software called ImageJ [101]. ImageJ is a versatile and well-established image processing program that has been used to study fouling [102],[103] and other scientific phenomena [104] by researchers in different

disciplines. The methodology used to analyze the images for the detection of fouling is adapted from Refs. [65] and [67], and the image processing steps are depicted in Figure 3.6.

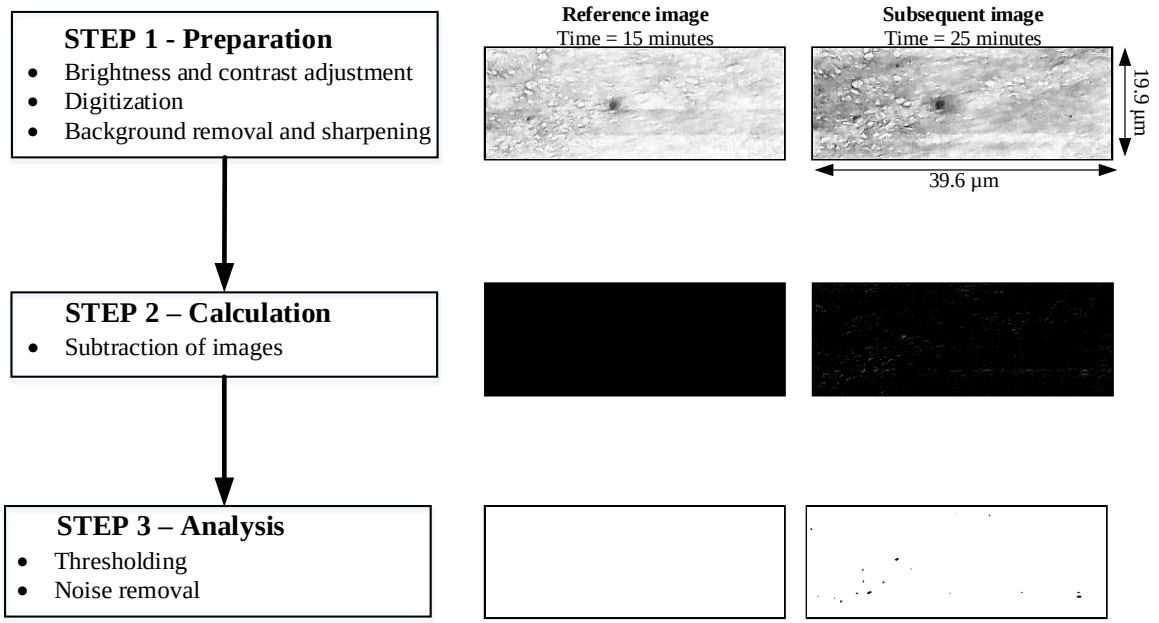

Figure 3.6. Image processing algorithm for the detection of the onset of crystallization fouling in the LAMEE. **Note**. The images shown in Figure 3.6 are for a test performed at the high fouling rate (RH_{air} = 10% and C_{sol}^{*} = 1.03). The area of focus that is monitored during the test is indicated by a dot on the membrane (*see* the images in Step 1).

The algorithm shown in Figure 3.6 consists of three major steps which are implemented using a macro that executes the built-in functions of ImageJ program [105]. The first step involves preparing an image (Step 1) for subsequent calculation (Step 2) and analysis (Step 3), and the settings of Steps 1 – 3 are explained in the following paragraphs.

In Step 1, the area of focus that is tracked during the test is selected using the "Region of Interest (ROI) Manager" function. Afterwards, the selected region of interest is cropped using the "Crop" function, and the brightness and contrast of the image are optimized using the "Brightness and Contrast" function with the "automatic" setting selected. Thereafter, the image is digitized by converting the RGB color from the digital microscope to an 8-bit grayscale image using the "8-bit" option of the "Type" function. Background noise is subtracted from the image by using the "Subtract Background" function, with selected options of "light background" (to eliminate unnecessary lighting/shadow features in the image background), "sliding paraboloid" (for

corrections of the image background) and “disable smoothing” (to ensure that the image data are preserved after the subtraction process). As recommended by Ref. [105], the “rolling ball radius” of the “Subtract Background” function is set to the threshold pixel of the image which is not part of the background. The threshold pixel is set as 0.02% of the image surface area [65]. Finally, the image is sharpened using the “Sharpen” function in order to emphasize important surface features, such as crystal particles. After Step 1, a prepared image is saved in a database for subsequent processing, and the first prepared image for a test is named as the reference image.

Step 2 is a vital stage that involves comparing the most recent prepared image and reference image to check for any changes that may have occurred on a surface [67]. The comparison is performed by subtracting the reference image from subsequent images using the “subtract” operation of the “Image Calculator” function. The subtraction process yields a residual image which may contain information on the possible presence of crystal particles on a membrane.

In Step 3, thresholding is performed by converting the subtracted grayscale image to a black and white binary image using the “Make Binary” function. In addition, the “black background” option is unchecked which implies that crystal particles will appear as black dots on a white background if a membrane is fouled. Thereafter, the image is processed for noise removal by using the “Despeckle” function. Furthermore, the “Remove Outlier” function is used to eliminate unwanted noise from the membrane surface by using the default setting of “radius”, setting the threshold to the prescribed threshold pixel, and checking the “remove dark outliers” option.

The presence and surface area of crystal particles on a surface is determined by using the “Analyze Particles” function, with the particle “size” set to the prescribed threshold pixel. The “exclude on edges” option is selected in order to minimize the effect of digital artifacts that may be attached to the edges of the image area, and the “include holes” is selected to include the interior cavity of detected particles. The “Set Measurements” function is configured to analyze particles by fitting an ellipse to particles that are detected on the image and limiting the size of particles to the prescribed threshold pixel.

Fouling is confirmed when particles are first spotted on a completely processed image. The dots on the subsequent image in Step 3 (*see* Figure 3.6) indicate that crystals have accumulated during

the period between 15 and 25 minutes from the start of the test. In addition, the uncertainty in the time that fouling is detected is calculated as half of the resolution (time interval between the images taken) during the tests at the high and low fouling rates.

3.6 RESULTS AND DISCUSSION

The indirect non-invasive analysis methods presented in Section 3.5.2.1 are applied to determine if fouling exists for Membranes A and B at different operating conditions (*see* Table 2.4), and to identify the time at which fouling starts for example tests. Thereafter, the results obtained from the direct non-invasive method (*i.e.* digital microscopy) in Section 3.5.2.2 are presented for two operating conditions (*see* Table 3.2) using only Membrane A. Finally, the indirect non-invasive analysis methods are calibrated by using measurements from the direct non-invasive method as a benchmark.

3.6.1 Indirect non-invasive analysis methods

Figure 3.7 shows the application of the analysis methods to a test with Membrane A.

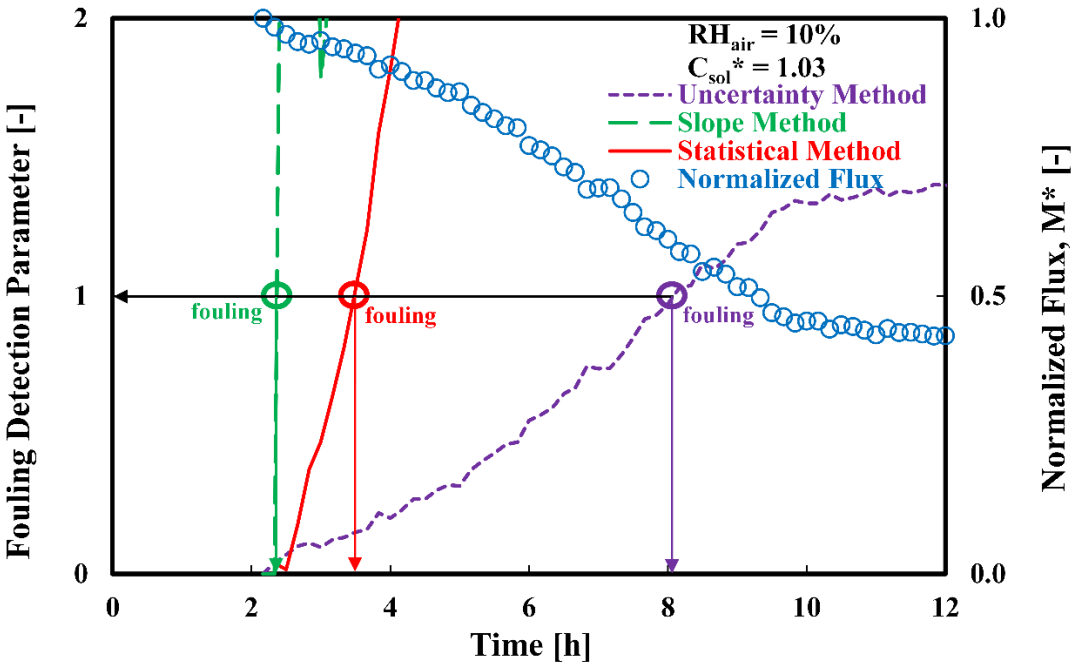

(a)

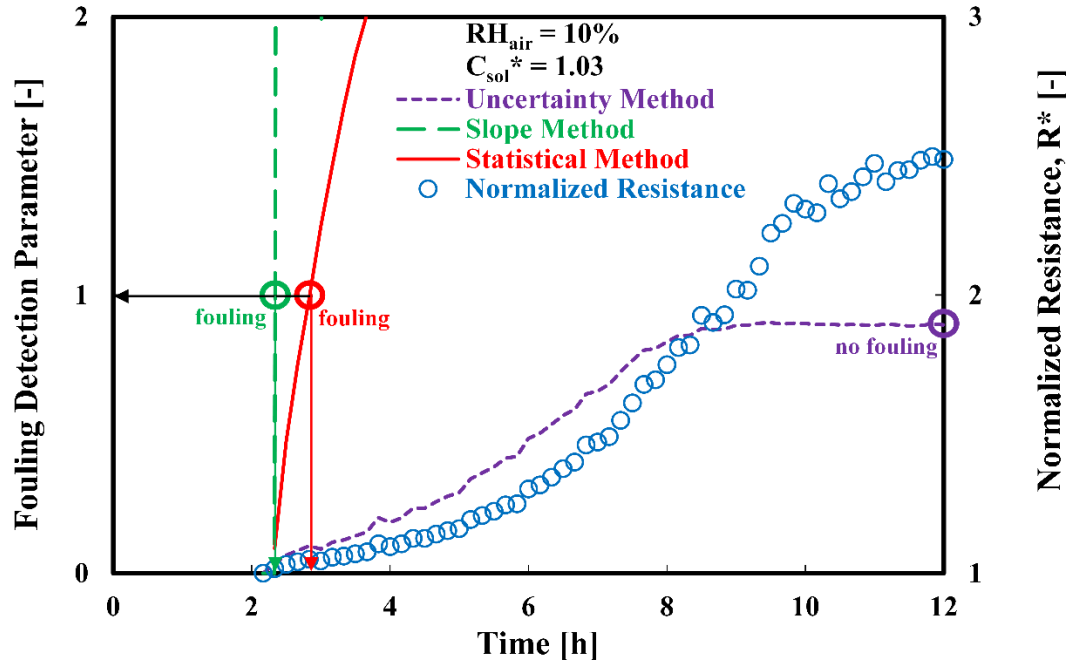

(b)

Figure 3.7. Values of fouling detection parameters for indirect non-invasive parameter methods of moisture transfer (**a**) flux and (**b**) resistance for a test using Membrane A with supersaturated $MgCl_2$(aq) (C_{sol}^* = 1.03) at RH_{air} = 10%. Fouling detection parameter refers to criteria f_u, f_{st} and f_{sl} for the uncertainty, statistical and slope methods, respectively.

As described in Section 3.5.2.1, the uncertainty, statistical and slope methods confirm fouling at the reference cut-off point of 1. It can be seen that from Figure 3.7(**a**) that the slope method is the most sensitive of the three methods since it is able to detect fouling at 2.5 h, whereas the statistical method detects fouling at 3.5 h. The uncertainty method only detects fouling at 8.2 h and is the least sensitive method.

In the test conditions of Figure 3.7(**b**), the slope and statistical methods detect fouling at 2.5 h and 3 h, respectively. However, the uncertainty method has a low sensitivity and is unable to conclude that fouling occurred in the test despite a doubling of the moisture transfer resistance of the LAMEE during the test. The relative sensitivity of the three indirect non-invasive analysis methods obtained using moisture transfer resistance in Figure 3.7(**b**) is consistent with the findings for moisture transfer flux in Figure 3.7(**a**).

Figure 3.8 depicts the application of the indirect non-invasive analysis methods to a test with the same operating conditions as in Figure 3.7 but with Membrane B.

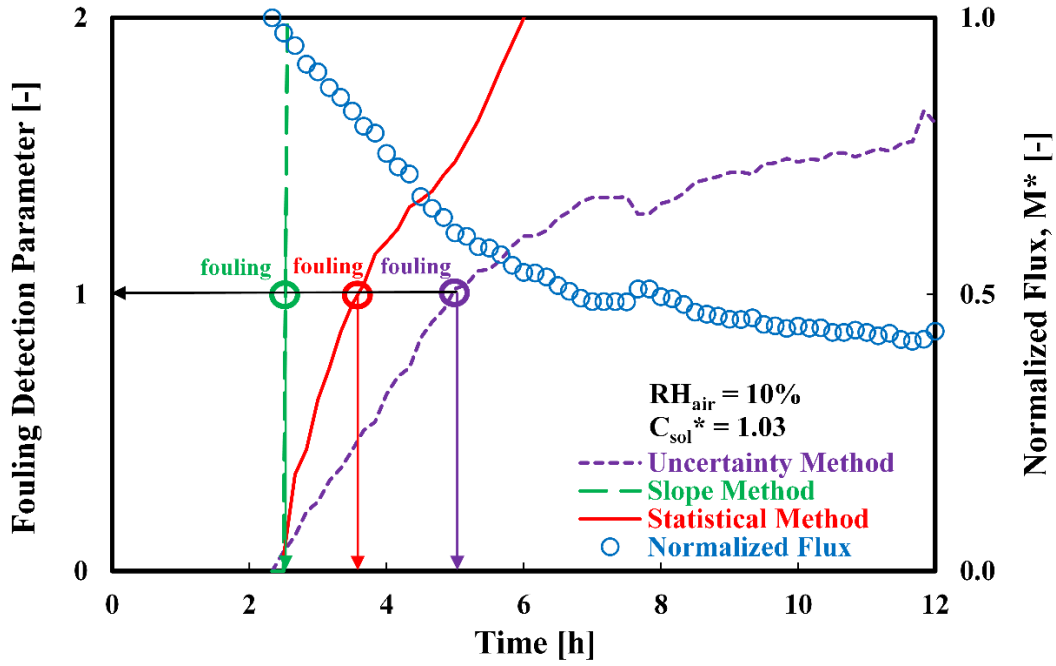

(a)

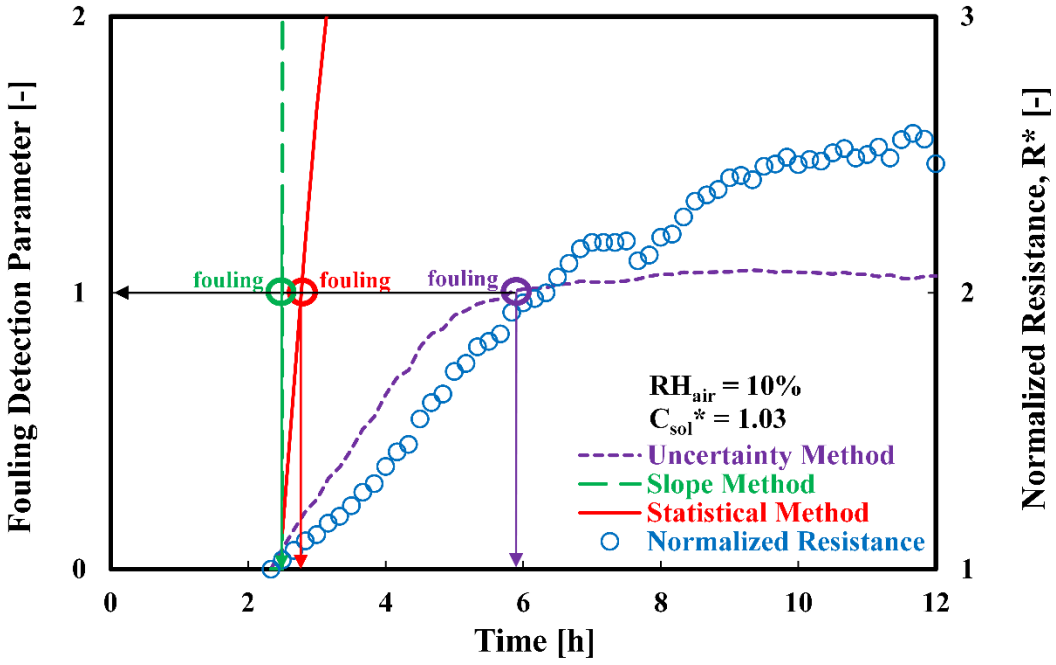

(b)

Figure 3.8. Values of fouling detection parameters for indirect non-invasive parameter methods of moisture transfer (**a**) flux and (**b**) resistance for a test using Membrane B with supersaturated $MgCl_2$(aq) (C_{sol}^* = 1.03) at RH_{air} = 10%. Fouling detection parameter refers to criteria f_u, f_{st} and f_{sl} for the uncertainty, statistical and slope methods, respectively.

Figure 3.8 shows that the degradation in the performance of the LAMEE with Membrane B is similar to that of Membrane A (*see* Figure 3.7), since the moisture transfer flux reduces by ~60% and the moisture transfer resistance increases by over a factor of 2 during the test. In addition, Figure 3.8(**a**) shows that the slope, statistical and uncertainty methods are able to detect fouling at 2.7 h, 3.7 h, and 5.0 h, respectively, using the moisture transfer flux, whereas Figure 3.8(**b**) shows that fouling is detected at 2.7 h, 2.8 h and 5.8 h, respectively, using the moisture transfer resistance. The relative sensitivity of the three methods for the detection of fouling in Membrane B (Figure 3.8) is consistent with the findings obtained using Membrane A (Figure 3.7).

The key findings from the results in Figure 3.7 and Figure 3.8 are concisely discussed by comparing the (i) three indirect non-invasive analysis methods, (ii) two indirect non-invasive parameter methods, and (iii) two membranes.

3.6.1.1 Three indirect non-invasive analysis methods

The slope method detects fouling at the earliest time for both moisture transfer flux and resistance, and is closely followed by the statistical method. In addition, the slope and statistical methods generally exhibit a good agreement. On the other hand, the uncertainty method is very conservative and is the slowest to detect fouling. Although the three indirect non-invasive analysis methods can be used to estimate the time that fouling starts in a test, they need to be calibrated to conclude the definite time of fouling initiation. This is because the methods assess fouling by indirectly measuring the impact of fouling on the performance of LAMEEs, rather than by directly detecting the presence of crystallization fouling in membranes.

3.6.1.2 Two indirect non-invasive parameter methods

Generally, moisture transfer flux appears to be more sensitive to detect fouling than moisture transfer resistance for the uncertainty and slope methods, whereas resistance is more sensitive to detect fouling than flux for the statistical method. Furthermore, the combination of the uncertainty method and moisture transfer resistance is observed to yield the least sensitivity to detect fouling (*see* Figure 3.7**b**). This can be ascribed to the fact that the uncertainty in the moisture transfer resistance is higher than that of the flux, due to the additional term (ΔW_{lm}) in **Eq. (3.3)**.

3.6.1.3 Two membranes

Crystallization fouling is initiated earlier in Membrane B than in Membrane A. The fouling rate is also higher for Membrane B than Membrane A. This behavior can be attributed to the vapor diffusion resistance (VDR) of Membrane B, which is approximately four times lower than the VDR of Membrane A. The lower VDR of Membrane B leads to higher moisture transfer rates through the membrane. At higher rates of moisture transfer through a membrane, the solution concentration at the solution-membrane interface will reach supersaturation quicker, and the tendency for the nucleation of crystal particles on the membrane will increase. It is interesting to note that the asymptotic values of the indirect non-invasive parameter methods are the same with both membranes (*see* Figure 3.4), which implies that investing in a better membrane with lower VDR may not improve the long-term performance of a LAMEE when fouling occurs.

3.6.1.4 Overview of results using indirect non-invasive analysis and parameter methods

The aforementioned findings from the tests using Membranes A and B with supersaturated $MgCl_2$(aq) (C_{sol}^* = 1.03) at RH_{air} = 10% are also observed for tests performed at other operating conditions. Table 3.3 shows an overview of the results for all the operating conditions tested.

Table 3.3. Summary of fouling tests showing the indirect non-invasive analysis methods and indirect non-invasive parameter methods that detect fouling in Membranes A and B at different operating conditions.

C_{sol}^*	RH_{air}	Moisture transfer flux			Moisture transfer resistance		
[-]	[%]	Uncertainty	Statistical	Slope	Uncertainty	Statistical	Slope
Membrane A							
0.9	10	–	D	D	–	D	D
	20	–	D	D	–	D	D
	30	–	D	D	–	–	D
1.0	10	–	D	D	–	D	D
	20	–	D	D	–	D	D
	30	–	D	D	–	D	–
1.03	10	D	D	D	–	D	D
	20	–	D	D	–	D	D
	30	–	D	D	–	D	D
Membrane B							
0.9	10	–	D	D	–	D	D
1.0		–	D	D	–	D	D
1.03		D	D	D	D	D	D

Note. D = Fouling detected; – = Fouling not detected.

Table 3.3 shows that fouling is detected in the LAMEE at all the operating conditions tested by at least one method but not by all methods. Although the results in Table 3.3 demonstrate the effectiveness of the analysis methods to detect the occurrence of fouling, the methods still need to be calibrated before they can be used to confirm the time of fouling initiation.

3.6.2 Digital microscopy

Digital microscopy is used to identify the onset of fouling in the LAMEE through real-time observation of crystallization fouling on the membrane surface. Figure 3.9 shows the application of digital microscopy to tests performed at the high and low fouling rates.

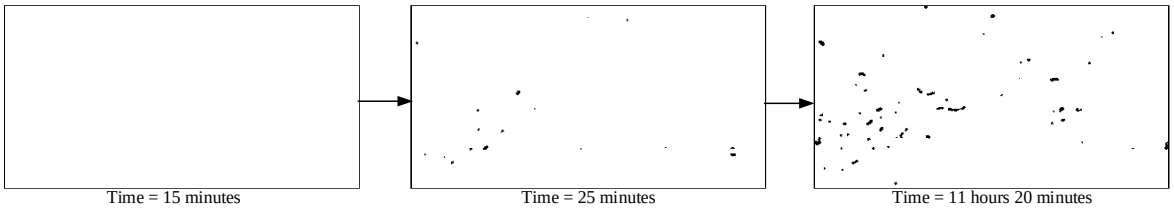

(a) High fouling rate (image dimensions = 39.6 µm × 19.9 µm).

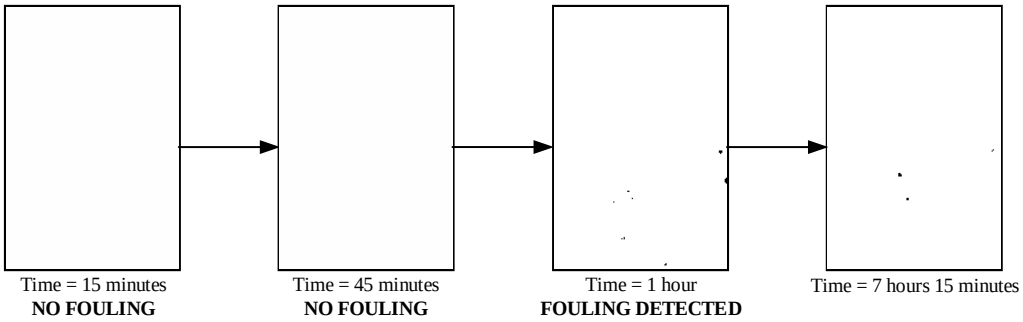

(b) Low fouling rate (image dimensions = 8.4 µm × 12.5 µm).

Figure 3.9. Detection of crystallization fouling using the digital microscopy method using Membrane A at the (**a**) high (RH_{air} = 10% and C_{sol}^{*} = 1.03) and (**b**) low (RH_{air} = 30% and C_{sol}^{*} = 1.0) fouling rates.

Figure 3.9 shows that fouling is detected at 25 minutes and at 1 h in the test with high and low fouling rates, respectively. As expected, fouling is detected earlier in the test with the high fouling rate (RH_{air} = 10% and C_{sol}^{*} = 1.03) than the test with a low fouling rate (RH_{air} = 30% and C_{sol}^{*} = 1.0), because of the higher degree of supersaturation of the bulk desiccant solution in the former which favors a faster nucleation of crystals.

After fouling is first detected, a visible increase in the growth of crystals is observed in the test with the high fouling rate (Figure 3.9**a**), whereas there is no significant increase in the buildup of crystals on the membrane surface in the test with the low fouling rate (Figure 3.9**b**). The trends in Figure 3.9 are confirmed by Figure 3.10 which presents the area of crystals on membranes as a function of time.

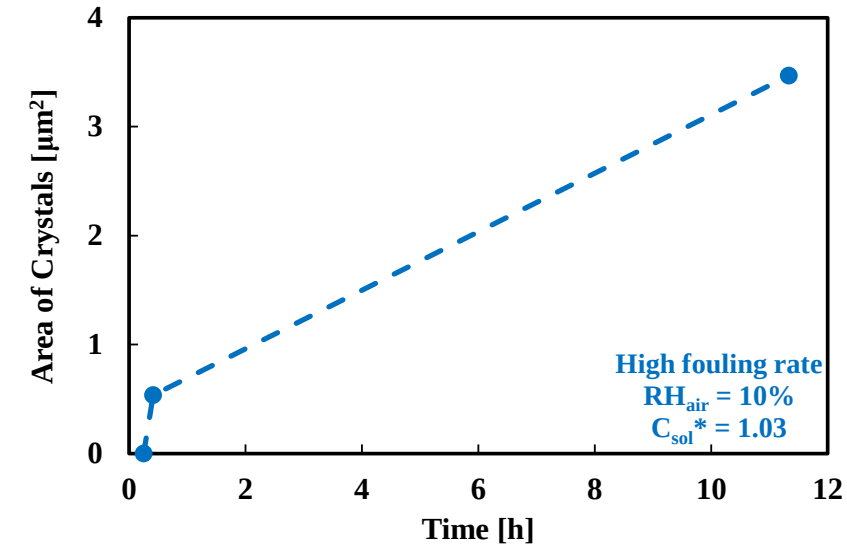

(a) High fouling rate.

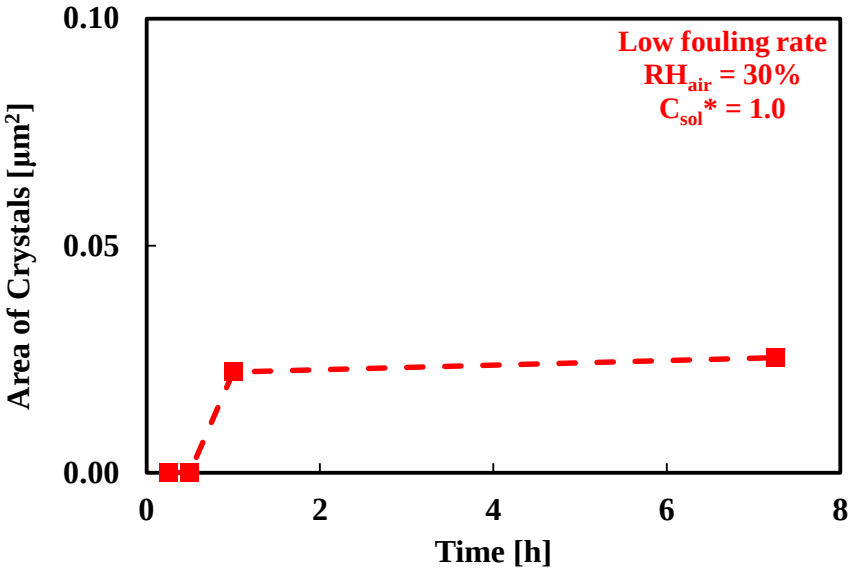

(b) Low fouling rate.

Figure 3.10. Area of crystals on the membrane surface as a function for time for tests performed using Membrane A at the (**a**) high (RH_{air} = 10% and C_{sol}^{*} = 1.03) and (**b**) low (RH_{air} = 30% and C_{sol}^{*} = 1.0) fouling rates. **Note**. Dotted lines are used to join the data points in order to highlight the trend in the data.

The area of crystals on the membrane surface increases by a factor of 6 within 11 h in the test with the high fouling rate (Figure 3.10**a**), whereas the area of crystals on the membrane surface does not increase noticeably within the first 6 h of the test with the low fouling rate (Figure 3.10**b**).

3.6.3 Comparison of direct and indirect non-invasive methods

Four non-invasive methods, which consist of three indirect analysis methods and one direct method, have been used to identify the onset of fouling in the LAMEE. A comparison of the time that fouling is detected by the four methods is shown in Figure 3.11.

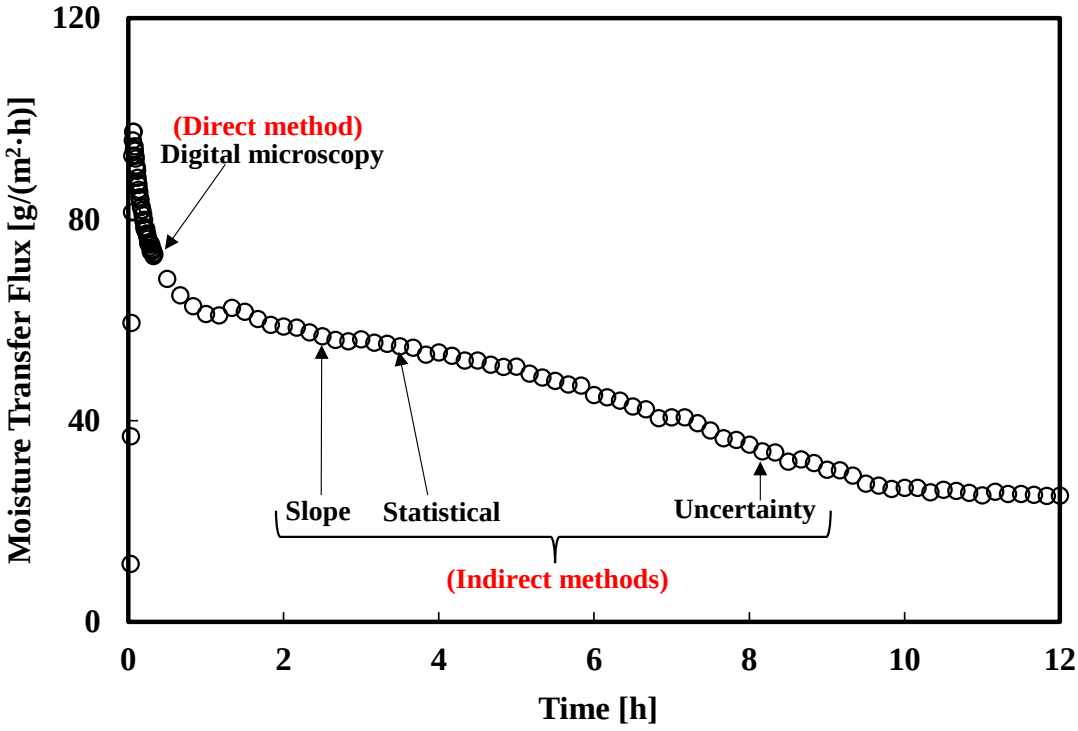

Figure 3.11. Comparison of the time that the onset of fouling is detected in the LAMEE using four non-invasive methods for a test at the high fouling rate (RH_{air} = 10% and C_{sol}^{*} = 1.03) with Membrane A. **Note**. Arrows are used to indicate the time that fouling is detected by the different methods.

Figure 3.11 indicates that fouling is first detected by the digital microscopy method at 25 minutes, and afterwards by the slope, statistical and uncertainty methods at 2.5 h, 3.5 h and 8.2 h, respectively. However, Figure 3.11 only shows the results for the test at the high fouling rate, and the indicated indirect non-invasive analysis methods are based on moisture transfer flux.

A comprehensive overview of the time that fouling is detected at the high and low fouling rates by the methods presented in this chapter is given in Table 3.4.

Table 3.4. Comparison of the time that fouling is detected by different indirect non-invasive analysis methods in 12-h tests using $MgCl_2$(aq) and Membrane A.

Tests			**Indirect non-invasive analysis methods**						
Fouling rate	**C_{sol}^* [-]**	**RH_{air} [%]**	**Moisture transfer flux**			**Moisture transfer resistance**			**DM**
			U	**ST**	**SL**	**U**	**ST**	**SL**	
High	1.03	10	8.2 h	3.5 h	2.5 h	N	3.0 h	2.5 h	25.0 m
Low	1.0	30	N	3.8 h	3.0 h	N	3.3 h	3.2 h	1.0 h

Note. U = Uncertainty method; ST = Statistical method; SL = Slope method; DM = Digital microscopy; N = Fouling undetected; m = minute. The earliest time of fouling detection is underlined for the two test conditions.

Table 3.4 shows that the digital microscopy method is more sensitive than the three indirect non-invasive analysis methods. In addition, from the results in Table 3.4, digital microscopy is estimated to detect the onset of fouling three to eight times earlier than the indirect non-invasive analysis methods for the two operating conditions tested. The results are consistent with the findings of Ref. [67] where it is reported that real-time digital microscopy is able to detect silica fouling in reverse osmosis membranes at an earlier time than observing flux decline by a factor of 2 – 7. The analyses of moisture transfer flux and resistance measurements are less sensitive to fouling because flux and resistance are estimated from bulk inlet and outlet properties of the fluid streams in exchangers, whereas fouling is essentially a localized deposition process that may not be easily identified based on bulk measurements.

The major advantage of the direct observation of fouling with a digital microscope over the indirect analysis methods is its ability to directly track and monitor the initiation of particles on a membrane without the need to rely on indirect measurements of process variables (*e.g.* temperature or concentration). However, digital microscopy requires significant image processing and is unsuitable to visualize membranes in opaque or colloidal liquids. Consequently, digital microscopy is not practicable for widespread adoption in operating exchangers.

On the other hand, the indirect non-invasive analysis methods can be used to detect and monitor fouling in real-time, and are more suitable for practical application in exchangers after their sensitivity is adjusted for early detection of fouling. In Section 3.6.4, the sensitivity of the indirect

non-invasive analysis methods presented in this chapter will be tuned using the results from the direct non-invasive method (digital microscopy).

3.6.4 Calibration of indirect non-invasive analysis methods

In this section, the three indirect non-invasive analysis methods are first calibrated and thereafter applied to detect the onset of fouling in the LAMEE. The calibration procedure is described in Section 3.6.4.1, and the results of the application of the calibrated methods to detect fouling is presented in Section 3.6.4.2.

3.6.4.1 Calibration procedure

A schematic of the calibration procedure is shown in Figure 3.12.

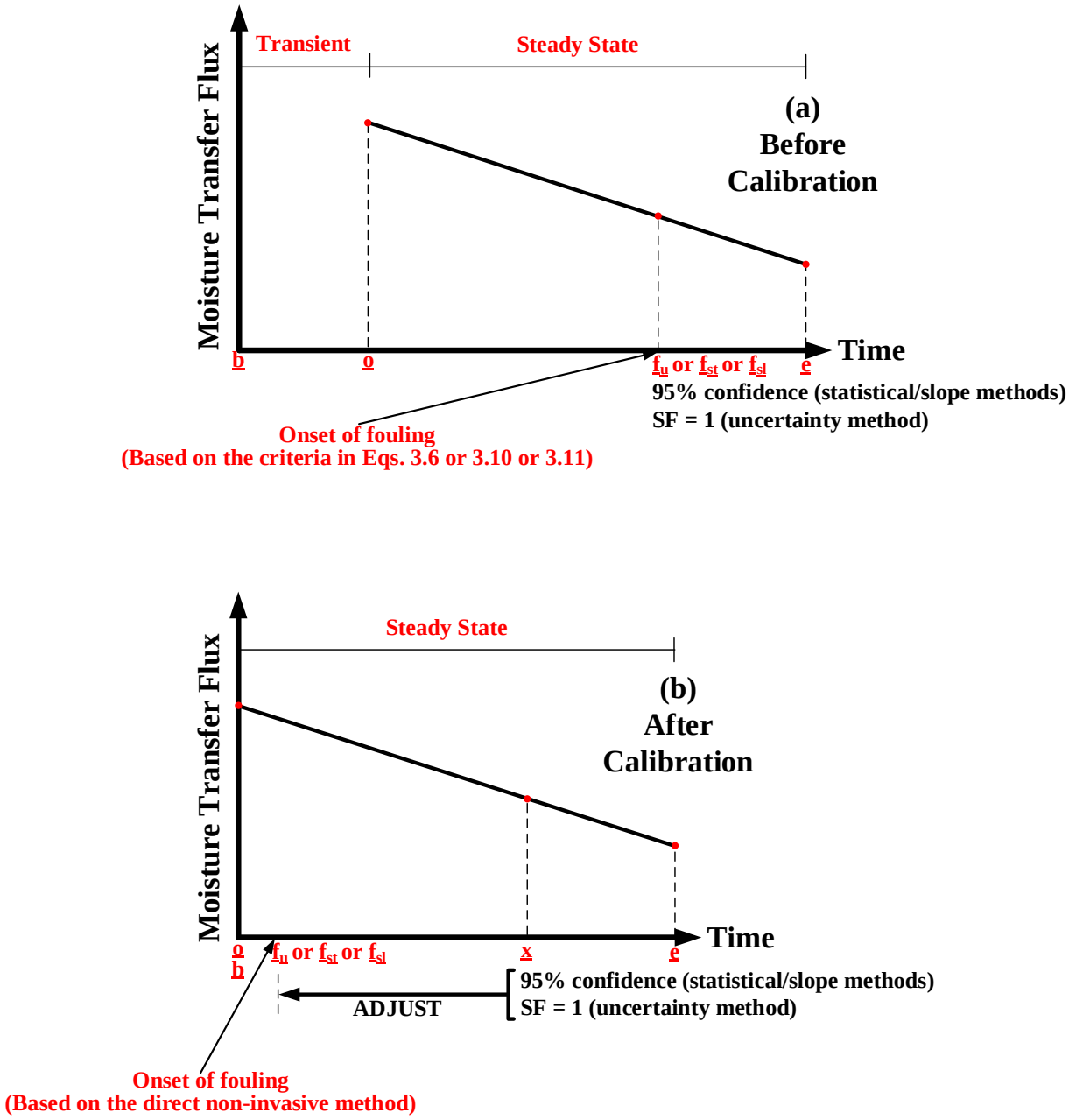

Figure 3.12. Procedure for the calibration of the indirect non-invasive analysis methods (*i.e.* uncertainty, statistical and slope methods). **Note**. The scale factor (SF) for the uncertainty method is defined in **Eq. (3.12)**. The beginning (**b**), start of the steady-state period (**o**), fouling detection (uncertainty method ($\mathbf{f_u}$), statistical method ($\mathbf{f_{st}}$), slope method ($\mathbf{f_{sl}}$)), and end (**e**) points are indicated in Figure 3.12. Point (**x**) corresponds to equivalent point that fouling is detected at 95% confidence or SF = 1 in Figure 3.12(**b**). The calibration procedure in Figure 3.12 applies to both moisture transfer flux and resistance.

Figure 3.12(**a**) illustrates the transient (**b** – **o**) and steady-state (**o** – **e**) periods of a hypothetical test before calibration is performed. As previously explained in Chapter 2 (Section 2.6.1), the boundary conditions of the desiccant solution initially undergo a transient period at the start of a test before reaching steady-state conditions. Furthermore, it has been previously established in Chapter 2 (Section 2.6.7) that the transient period of a test neither triggers fouling nor increases the likelihood of the occurrence of fouling. In other words, the transient period of a test most likely most likely has a negligible impact on crystallization fouling in the LAMEE.

In this thesis, fouling is studied under steady-state conditions; consequently, the start of the steady-state period (**o**) is used as the start point for all the data analyses in the thesis. Figure 3.12(**a**) shows that there is a decay in the moisture transfer flux between the start of the steady-state period (**o**) and the end (**e**) of the test. Fouling is detected at the fouling detection point (*i.e.* ($\mathbf{f_u}$) or ($\mathbf{f_{st}}$) or ($\mathbf{f_{sl}}$)) by using any of the uncertainty, statistical or slope methods, respectively. In addition, fouling is confirmed by the statistical and slope methods based on a 95% confidence interval using **Eqs. (3.10)** and **(3.11)**, respectively. The uncertainty method, however, detects fouling using the criterion in **Eq. (3.6)**, which is slightly modified as given by:

$$f_u = SF \times \left| \frac{F - F_o}{U_{F-F_o}} \right| > 1, \; F = \dot{m}''_v \text{ or } R, \tag{3.12}$$

where the scale factor, SF, has a default value of 1 in order to make **Eq. (3.12)** to be consistent with **Eq. (3.6)**.

As shown in Figure 3.12(**a**), the indirect non-invasive analysis methods detect fouling after the start point of the steady-state of a test (*see* Figure 3.7 and Figure 3.8). However, the direct non-invasive method (digital microscopy) detects fouling earlier than the steady-state period of the test for both tests at high and low fouling rates (*see* Table 3.4). Consequently, to calibrate the indirect non-invasive analysis methods using the digital microscopy method, the start point of the steady-state period of a test (**o**) is shifted backwards to the beginning of the test (**b**) (*i.e.* t = 0 h), as shown in Figure 3.12(**b**). In addition, the time interval between points (**o**) and ($\mathbf{f_u}$) or ($\mathbf{f_{st}}$) or ($\mathbf{f_{sl}}$) in Figure 3.12(**a**) is kept constant in Figure 3.12(**b**). Thus, point (**x**) corresponds to the equivalent point (and criterion) of fouling detection before calibration at 95% confidence (statistical and slope

methods) or SF = 1 (uncertainty method) in Figure 3.12(**b**). If fouling was not detected in Figure 3.12(**a**), as is the case for the uncertainty method, the corresponding criterion of fouling detection before calibration (*i.e.* SF = 1) in Figure 3.12(**b**) defaults to $f_u = 1$.

The indirect non-invasive analysis methods are calibrated by adjusting the default values of their settings (confidence interval and scale factor) until fouling is detected at a time that corresponds with the digital microscopy method and satisfies the criterion at point (**x**) (Figure 3.12**b**). The adjustments are performed by iteratively increasing or decreasing the default values of the settings until fouling is detected, as given by

$$\text{Adjusted value} = \text{Default value} \pm (\text{Interval} \times n), \; n = 1, 2, 3 \cdots \infty, \qquad (3.13)$$

where Adjust value is the adjusted or corrected value of the settings (confidence interval and scale factor) of the indirect non-invasive analysis methods after calibration, and Default value is the default or original value of the settings of the analysis methods before calibration. Interval is the step size that is used for the adjustment of the confidence interval and scale factor (SF) of the indirect non-invasive analysis methods. The value of Interval is 1% for the statistical and slope methods, and 0.1 for the uncertainty method.

A comparison of the default and adjusted settings of the indirect non-invasive analysis methods is shown in Table 3.5.

Table 3.5. Results of the calibration of the indirect non-invasive analysis methods.

Method	**Setting**	**Default value**	**Adjusted value**			
			High fouling rate		**Low fouling rate**	
			Flux	**Resistance**	**Flux**	**Resistance**
Uncertainty	Scale factor, SF	1	13.7	12.1	12.8	16.6
Statistical	Confidence interval	95%	27%	51%	29%	66%
Slope	Confidence interval	95%	80%	67%	82%	76%

Note. High fouling rate corresponds to the test at RH_{air} = 10% and C_{sol}^* = 1.03, whereas low fouling rate corresponds to the test at RH_{air} = 30% and C_{sol}^* = 1.0. Membrane A is used for both the high and low fouling rate tests.

It can be seen from Table 3.5 that, after calibration, the scale factor of the uncertainty method increases from 1 to 12 – 14 and 13 – 17 for the tests at the high and low fouling rates, respectively.

The reason for the increase in the scale factor can be ascribed to the fact that the uncertainty in the indirect non-invasive parameter methods (denominator in **Eq. (3.12)**) is much greater than the change in the parameters (numerator in **Eq. (3.12)**). Thus, the ratio in **Eq. (3.12)** needs to be multiplied by a scale factor of 12 – 17 to make the uncertainty method to be sensitive enough to accurately detect when fouling begins. Alternatively, the sensitivity of the uncertainty method can be improved by increasing the magnitude in moisture transfer flux or resistance (via increasing the active surface area of the membrane) and reducing the uncertainty in the humidity measurements.

Table 3.5 also shows that the confidence intervals of the statistical method decrease from 95% to 27% – 51% and 29% – 66% for the tests at high and low fouling rates, respectively. Furthermore, the confidence intervals of the slope method also decrease from 95% to 67% – 80% and 76% – 82% for the tests at high and low fouling rates, respectively. Since the digital microscopy method detects fouling earlier than both the statistical and slope methods for the tests at the high and low fouling rates, the default confidence intervals of the two methods needs to be reduced in order to augment their sensitivity for early detection of fouling. Furthermore, it can be observed that the adjusted confidence intervals of the slope method are higher than that of the statistical method (for both moisture transfer flux and resistance). This is likely because the slope method is more sensitive to detect the start of fouling than the statistical method; thus, the confidence interval of the slope method only needs to be slightly reduced to detect the onset of fouling early.

3.6.4.2 Application of the calibrated methods to detect the onset of fouling

The calibrated indirect non-invasive analysis methods are used to detect the start of fouling under two scenarios (Scenarios 1 and 2), and the results are compared with the digital microscopy method which serves as a benchmark. Scenario 1 represents when the calibrated methods are applied to the same operating condition as the calibration (Section 3.6.4.2.1), and Scenario 2 represents when the calibrated methods are applied to a different operating condition from the calibration (Section 3.6.4.2.2).

3.6.4.2.1 Scenario 1 – same operating condition as the calibration

The operating condition of the calibration that is used for Scenario 1 is the test at the high fouling rate (*see* Table 3.5). The results of the application of the calibrated methods to detect fouling at the same operating condition as the calibration (*i.e.* the high fouling rate) is shown in Figure 3.13.

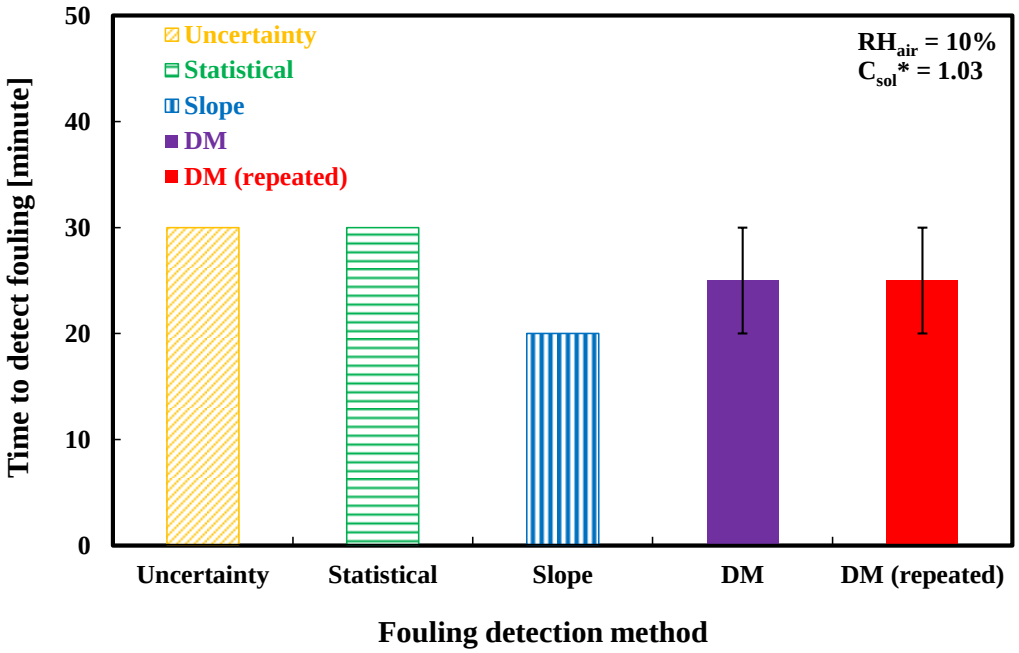

(a) Moisture transfer flux.

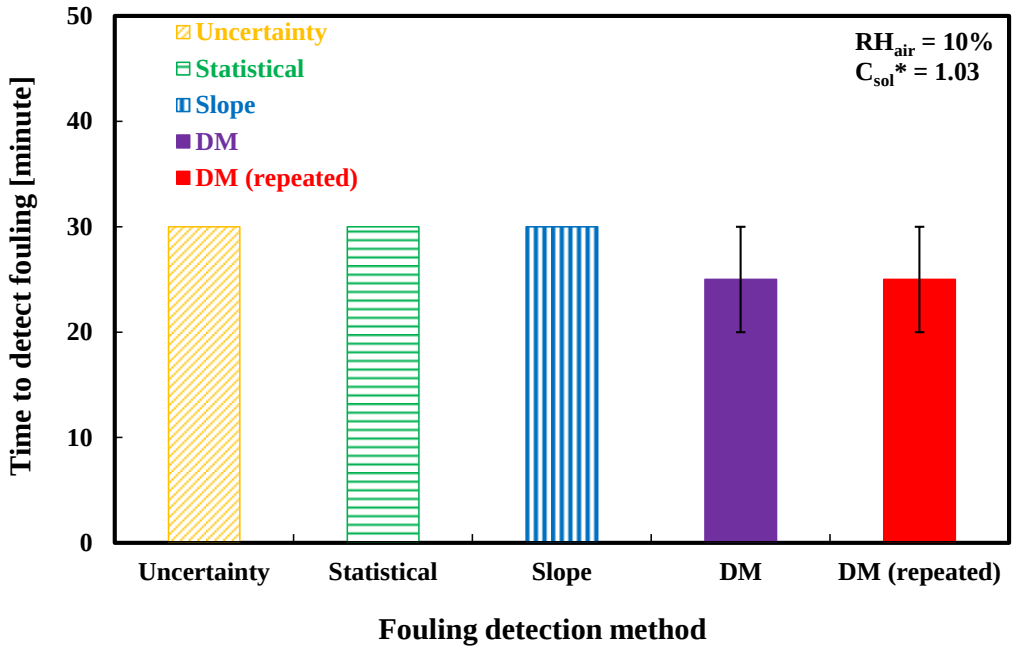

(b) Moisture transfer resistance.

Figure 3.13. Implementation of the calibrated indirect non-invasive analysis methods to detect the onset of fouling at the same operating condition as the calibration (*i.e.* the high fouling rate) using Membrane A. **Note**. DM = Digital microscopy.

Expectedly, Figure 3.13 shows that all the calibrated indirect non-invasive analysis methods detect fouling within 20 – 30 minutes for both moisture transfer flux and resistance. This represents a maximum discrepancy of 5 minutes from the time that fouling is detected by the digital microscopy method, *i.e.* 25 ± 5 minutes. The calibrated methods detect fouling at 20 minutes rather than 25 minutes because the data set is resolved at 10-minute intervals (*see* Figure 2.5). The reason for the high level of agreement between the calibrated indirect non-invasive analysis methods and the digital microscopy method is simply because the calibrated methods are applied to detect the start of fouling at the same operating condition as the calibration.

3.6.4.2.2 Scenario 2 – different operating condition from the calibration (extrapolation)

In Scenario 2, the calibrated indirect non-invasive analysis methods are extrapolated to detect the start of fouling at a different operating condition from the calibration (*i.e.* the low fouling rate), and the results are shown in Figure 3.14.

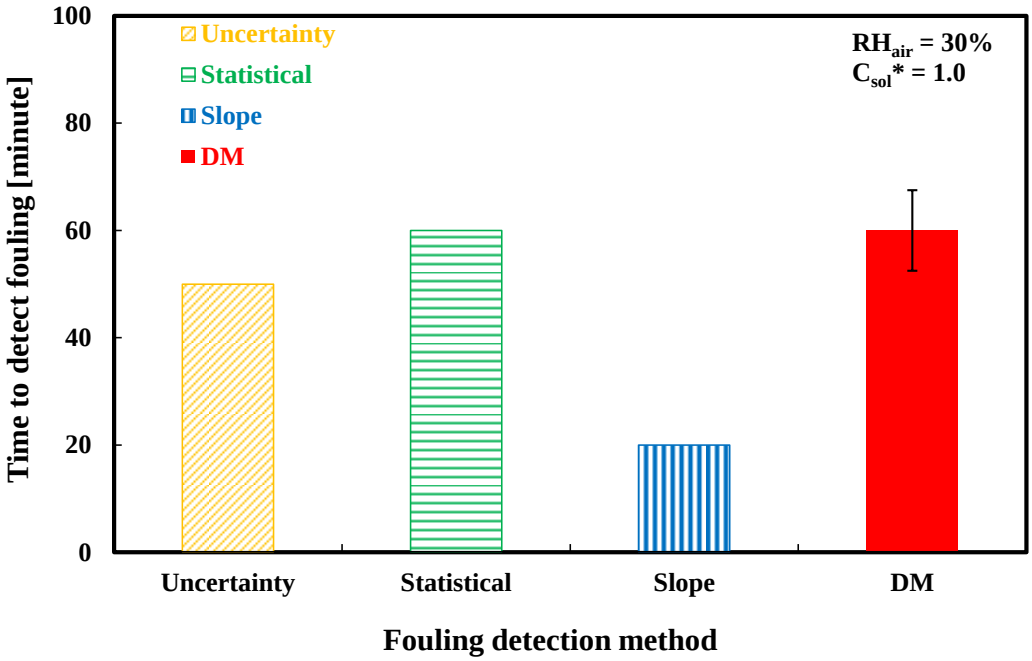

(a) Moisture transfer flux.

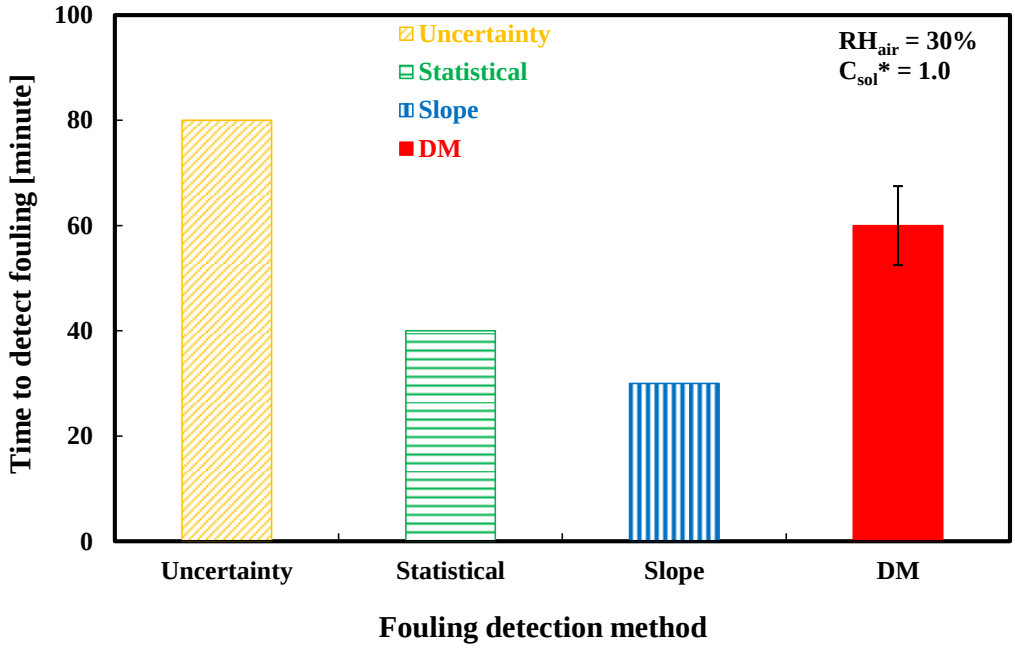

(b) Moisture transfer resistance.

Figure 3.14. Implementation of the calibrated indirect non-invasive analysis methods to detect the onset of fouling at a different operating condition from the calibration (*i.e.* the low fouling rate) using Membrane A. **Note**. DM = Digital microscopy.

Figure 3.14(**a**) shows that the calibrated uncertainty, statistical and slope methods (using moisture transfer flux) detect fouling at 50, 60 and 20 minutes, respectively, whereas the benchmark digital microscopy method detects fouling at 60 ± 7.5 minutes. Thus, the calibrated statistical method detects fouling at exactly the same time as the digital microscopy method. However, the calibrated uncertainty and slope methods detect fouling earlier than the digital microscopy method by 10 and 30 minutes, respectively, which is higher than the uncertainty of the digital microscopy method (± 7.5 minutes).

It can be seen from Figure 3.14(**b**) that the calibrated uncertainty, statistical and slope methods (using moisture transfer resistance) detect fouling at 80, 40 and 30 minutes, respectively. Thus, the discrepancy between the time that fouling is detected using the calibrated uncertainty and slope methods versus the digital microscopy method is 20 – 30 minutes, which noticeably exceeds the uncertainty of the digital microscopy method (± 7.5 minutes).

Two key findings can be concluded from the results in Figure 3.13 and Figure 3.14. Firstly, apart from the statistical method (using moisture transfer flux), the calibrated indirect non-invasive analysis methods fail to accurately detect the start of fouling when used for a different operating condition from the calibration. The reason may be attributed to the different mechanisms of deposit formation at the two operating conditions (*i.e.* high and low fouling rates). Secondly, the calibrated methods can accurately detect the start of fouling within a maximum discrepancy of 5 minutes when used for the same operating condition as the calibration. This implies that the calibrated methods should be used with care for extrapolated operating conditions. Further testing would be needed to fully determine the extrapolation uncertainty of the calibrated methods.

3.7 CONCLUSION

This chapter extends the work done in Chapter 2 by introducing a new indirect non-invasive analysis method (*i.e.* slope method) to identify the occurrence and onset of fouling in liquid-to-air membrane energy exchangers (LAMEEs). The three indirect non-invasive analysis methods (uncertainty, statistical and slope methods) are used to detect fouling by analyzing two indirect non-invasive parameter methods (moisture transfer flux and resistance). The indirect non-invasive parameter methods are calculated from experimental measurements obtained during the dehydration of $MgCl_2$(aq) desiccant solution at different concentrations. The indirect non-invasive

analysis methods are also used to compare the onset of fouling between two different membranes with different vapor diffusion resistances (VDRs).

A direct non-invasive method (*i.e.* digital microscopy) is introduced in this chapter to directly observe the onset of crystallization fouling in the LAMEE. Finally, the results of the digital microscopy method are used as a benchmark to calibrate the three indirect non-invasive analysis methods, and the calibrated analysis methods are subsequently applied to detect fouling. The main findings from the chapter are outlined as follows:

1. The three indirect non-invasive analysis methods can detect the occurrence and onset of crystallization fouling in the LAMEE. The comparison of the three analysis methods indicates that the slope method is the most sensitive method to detect the onset of fouling in the LAMEE, followed by the statistical and uncertainty methods.
2. The comparison of two membranes shows that the membrane with lower vapor diffusion resistance (VDR) produces a higher moisture transfer flux through the membrane, thereby leading to an earlier initiation of crystallization fouling in the LAMEE and a higher fouling rate compared to the membrane with higher VDR.
3. Digital microscopy is found to be the most sensitive fouling detection method, because it detects the start of fouling three to eight times earlier than the indirect non-invasive analysis methods.
4. The calibrated indirect non-invasive analysis methods can accurately detect the start of fouling at the same operating condition as the calibration, within a maximum discrepancy of 5 minutes from the time that fouling is detected with the direct non-invasive method (digital microscopy). However, the discrepancy can increase to 30 minutes when the calibrated analysis methods are extrapolated to detect fouling at a different operating condition from the calibration.

CHAPTER 4

EVOLUTION OF CRYSTALLIZATION FOULING IN MEMBRANES

4.1 OVERVIEW

This chapter partially addresses the second and third objectives of the thesis (*i.e.* to identify operating conditions that result in crystallization fouling in liquid-to-air membrane energy exchangers (LAMEEs), and identify the evolution of crystallization fouling in membranes). In this chapter, non-invasive and invasive methods are used to delineate the evolution of crystallization fouling in membranes. Two indirect non-invasive parameter methods are used to study the development of fouling in membranes by observing *in situ* measurements of moisture transfer flux and resistance. Three invasive methods are used to characterize membrane samples *ex situ*. The invasive methods consist of optical microscopy and scanning electron microscopy (SEM) which are used to identify the development of crystallization fouling in membranes, and energy dispersive X-ray spectroscopy (EDX) which is used to determine the composition of fouling deposits on membranes.

The SEM and EDX methods are also used to analyze the spatial morphology and composition of deposit formations on membranes, in order to further test the hypothesis in Chapter 2.

The manuscript included in this chapter was submitted to Langmuir. The first author (PhD student – Mr. Adesola O. Olufade) performed the experiments, analyzed the data and wrote the manuscript, and the second author (supervisor – Prof. Carey J. Simonson) reviewed the manuscript.

Characterization of the Evolution of Crystallization Fouling in Membranes Using Non-Invasive and Invasive Methods

(Submitted to Langmuir in December 2017)

A.O. Olufade, C.J. Simonson

4.2 ABSTRACT

Liquid-to-air membrane energy exchangers (LAMEEs) are promising for heating, ventilating and air-conditioning (HVAC) applications because they are able to use semi-permeable membranes to transfer heat and moisture between air and liquid desiccant streams. However, the development of crystallization fouling in membranes may pose a great risk to the long-term performance of LAMEEs.

The main aim of this chapter is to describe the use of non-invasive and invasive methods to experimentally study the evolution of crystallization fouling in membranes. Two indirect non-invasive parameter methods are used to identify the development of fouling by monitoring the changes in moisture transfer flux and resistance *in situ*. Three invasive methods are implemented to characterize membrane samples *ex situ*, by using optical microscopy and scanning electron microscopy (SEM) to delineate the development of crystallization fouling in membranes and energy dispersive X-ray spectroscopy (EDX) to identify the composition of fouling deposits. The experiments involve using dry air to dehydrate $MgCl_2$(aq) at high and low fouling rates.

SEM micrographs show that cake crystal formations accumulate on the membrane surface in the test with a high fouling rate, whereas few crystal particles are observed on the membrane surface in the test with a low fouling rate. Furthermore, SEM–EDX analysis confirms that the fouling deposits indeed consist of Mg, Cl and O elements, and indicate that fouling occurs in the regions of a membrane with high rates of moisture transfer.

4.3 INTRODUCTION

Chapter 1 (Section 1.1) provides details about the importance of studying fouling in heating, ventilating, and air-conditioning (HVAC) systems. In this chapter, the second research gap of the thesis in Chapter 1 (Section 1.2.3) is partially addressed. The specific sub-research gaps of the

thesis that are addressed in this chapter are 2(**a**), 2(**e**) and 2(**f**) (*the research gaps of the thesis and their corresponding numbers are presented in Chapter 1 (Section 1.2.3)*).

Research gap 2(**e**) is the major gap that is addressed in this chapter, and it is the lack of the delineation of the evolution of crystallization fouling in membranes. Although the literature review for research gap 2(**e**) was presented in Chapter 1 (Section 1.2.2.2), the review was limited to crystallization fouling in membrane exchangers for HVAC applications. Therefore, a broader overview of previous studies on the evolution of fouling in heat and membrane exchangers is briefly presented in this chapter.

There is a paucity of studies (*e.g.* Refs. [63],[106]) that have used both non-invasive and invasive methods to characterize the evolution of fouling. However, several studies (*e.g.* Refs. [26],[59],[61],[67],[72],[73],[107]–[109]) have used only non-invasive methods to identify the evolution of fouling. In addition, some of the studies that applied only non-invasive methods to study the evolution of fouling (*e.g.* Refs. [26],[59],[67]) subsequently used invasive methods (*e.g.* scanning electron microscopy) to characterize the morphology of fouling deposits. This chapter addresses research gap 2(**e**) by using both non-invasive and invasive methods to identify the development of fouling in the LAMEE. This has not been done by past researchers, and will therefore provide insight into how crystallization fouling evolves in membranes used for HVAC applications.

Research gap 2(**f**) is the absence of the analysis of the composition of membrane foulants, and research gap 2(**a**) is the lack of evaluation of the impact of moisture transfer rate on fouling in a liquid-to-air membrane energy exchanger (LAMEE). Research gap 2(**a**) has already been addressed in Chapter 2 and is further addressed in this chapter.

This chapters meets Objective 2(**a**) of the thesis since it further tests the hypothesis that reducing the moisture transfer rate through the membrane can minimize the likelihood of crystallization fouling in the LAMEE. This hypothesis has been previously tested in Chapter 2 using non-invasive methods, and is confirmed in this chapter by using invasive methods (*i.e.* scanning electron microscopy (SEM) and energy dispersive X-ray spectroscopy (EDX)). The objectives of the thesis

that are newly addressed in this chapter are to (*the objectives of the thesis are presented in Chapter 1 (Figure 1.2)*):

3(**b**): Delineate the evolution and mechanisms of crystallization fouling in membranes.

3(**c**): Characterize the morphology of fouling deposits on membranes.

3(**d**): Identify the elemental composition of fouling deposits on membranes.

4.4 METHODOLOGY

In this chapter, the test facility that is presented in Chapter 2 (Figure 2.2) is used to experimentally characterize crystallization fouling in membranes. Fouling is assessed at two operating conditions (high and low fouling rates), and the details of the test conditions have been previously presented in Chapter 3 (Table 3.2). The properties of the membrane used in this chapter (*i.e.* Membrane A) have been previously presented in Chapter 2 (Table 2.1), and the micrographs of the membrane are shown in Figure 4.1.

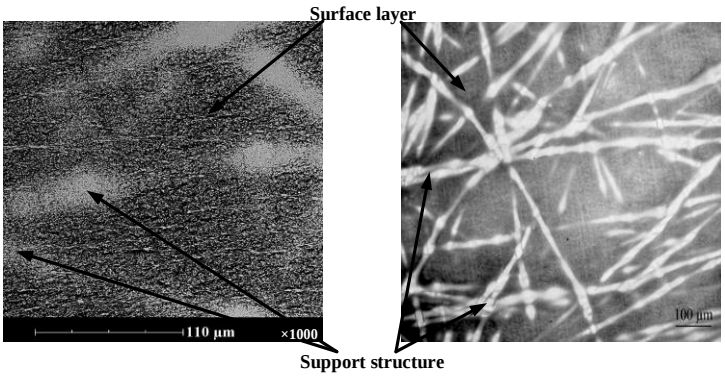

(a) Membrane surface layer and support structure.

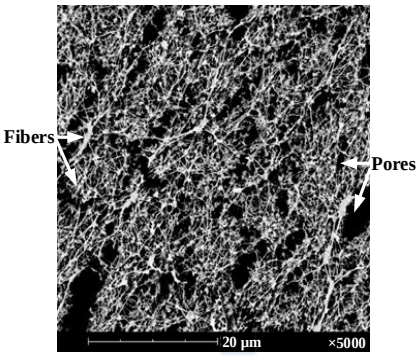

(b) Membrane surface layer.

Figure 4.1. Micrographs of the membrane used in the LAMEE. **Note**. The image on the right hand side of Figure 4.1(**a**) was taken with an optical microscope, whereas the images in Figure 4.1(**b**) and the left hand side of Figure 4.1(**a**) were taken with a scanning electron microscope. The optical microscopy and scanning electron microscopy methods are described in Sections 4.4.2.2 and 4.4.2.3, respectively.

Figure 4.1(**a**) shows that membrane consists of a polytetrafluoroethylene (PTFE) support structure and expanded PTFE surface layer. The support structure provides a strong backing for the membrane, whereas the surface layer is hydrophobic and serves to prevent liquid from permeating through the membrane. A close-up image of the membrane surface is shown in Figure 4.1(**b**), and it comprises of interwoven PTFE fibers and numerous stretched pores. The pores are the areas where moisture diffuses through the membrane.

Experimental tests are performed to dehydrate $MgCl_2$(aq) using a dry air stream. As moisture diffuses through the membrane pores, crystals may likely deposit internally within the membrane pores or externally on the membrane surface (*see* Figure 3.2**b**). The tests are performed for different time intervals that range from 30 minutes to 12 h, and repeated to confirm that the experiments are repeatable. After each test, the membrane is detached from the LAMEE and the LAMEE is thoroughly cleaned with hot distilled water. The membrane is preserved in a desiccator at room temperature (~24 °C) to ensure that crystals that may have formed within the membrane do not absorb moisture from the ambient environment and dissolve. The sections of a membrane that are subsequently analyzed are those that overlay on the holes in the inner pipe of the LAMEE where moisture transfer occurs (*see* Figure 2.2**c**).

4.4.1 Indirect non-invasive parameter methods

The non-invasive methods that are used to delineate the evolution of crystallization fouling consist of indirect non-invasive parameter methods that are estimated from *in situ* experimental measurements. The mathematical equations that are used to calculate moisture transfer flux and resistance have been presented in Chapter 2 (**Eqs. 2.10** and **2.11**) and Chapter 3 (**Eqs. 3.1** – **3.5**).

4.4.2 Invasive methods

Three invasive methods are used to characterize the buildup of fouling deposits on a membrane *ex situ*. The three methods are optical microscopy, scanning electron microscopy (SEM), and energy dispersive X-ray spectroscopy (EDX), and have been widely used to study fouling in several studies (*see* review papers [33],[38]). The implementation of the invasive methods are described in the following sub-sections.

4.4.2.1 Optical microscopy

Optical microscopy involves the use of lenses to magnify transmitted or reflected light from a surface, and has been described as the most direct way to monitor fouling on a membrane [33]. Although optical microscopy instruments are affordable and time-saving, they are limited by their need for a lucid fluid medium [34]. In addition, optical microscopy is typically used in ambient environments which are not conducive for the preservation of hygroscopic crystals that may be deposited in membranes. Notwithstanding, optical microscopy is used here as a preliminary technique to confirm the presence of crystal particles on a fouled membrane.

Fouled membrane samples are imaged with an optical microscope in order to examine the presence of fouling deposits. The fouled membrane samples are extracted from the desiccator where they are stored. Fresh membrane samples are also imaged for the purpose of comparison. The membrane samples are firmly taped to a microscope slide, and examined with a Zeiss AxioPlan microscope. The image processing program of the microscope [110] is used to improve the contrast of the images in order to clarify and intensify the features on the membrane surface. A comparison of the images of fresh and fouled membranes is shown in Figure 4.2.

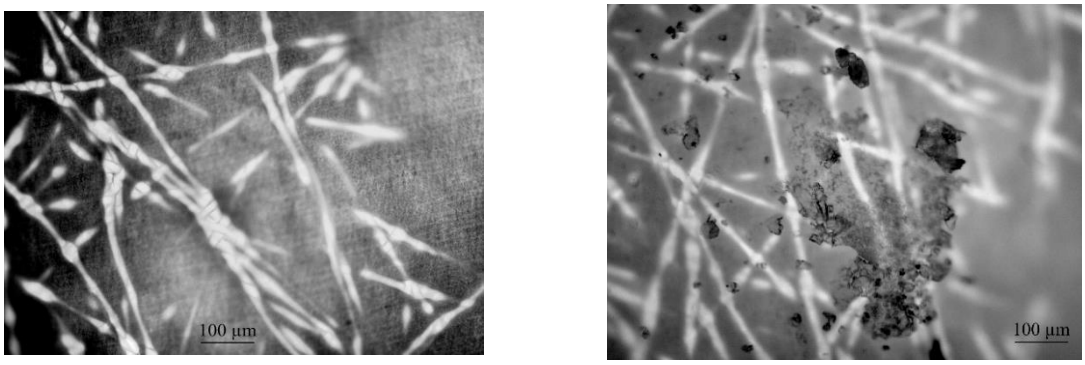

(a) Fresh membrane (b) Fouled membrane

Figure 4.2. Comparison of the surface sections of a (**a**) fresh membrane versus a (**b**) fouled membrane from a 30-minute test at the high fouling rate (RH_{air} = 10% and C_{sol}^{*} = 1.03).

Figure 4.2(**a**) clearly shows the surface layer and support structures of the fresh membrane (*see* Figure 4.1), whereas crystal deposits are clearly visible as dark particles on the fouled membrane image in Figure 4.2(**b**). The images in Figure 4.2(**b**) not only confirm the formation of crystal particles on the membrane surface, but also demonstrate that there was such a rapid and severe fouling that the crystals formed a cake structure within a 30-minute period.

4.4.2.2 Scanning electron microscopy (SEM)

SEM is used to depict the morphological changes in the development of crystallization fouling in membranes. SEM is a widely used surface characterization technique, which involves the bombardment of a surface with powerful electrons and subsequent detection/image reconstruction of the reflected or scattered electrons with electro-magnetic lenses [33]. SEM does not require the preparation of very thin samples like in transmission electron microscopy, and can typically achieve a resolution of 1 – 10 nm which exceeds the limit of optical microscopy techniques [111]. However, polymer membranes need to be coated with a conductive metal before SEM analysis, in order to increase the conductivity of the membrane surface and image resolution [33],[38].

Before SEM imaging is performed, a preserved membrane is extracted from the desiccator and several sections of the membrane sample are dissected, mounted on stubs and coated with a thin film of gold using an Edwards S150B gold sputter coater. SEM imaging is mostly done using a Phenom G2 Pure desktop scanning electron microscope with a resolution of 30 nm. However, the shape of full-grown crystals on fouled membranes are imaged using a Hitachi SU8010 field emission scanning electron microscope which can achieve a resolution of 1.0 – 1.3 nm.

For each test performed, several sections of a membrane are analyzed with the scanning electron microscope to assess the similarity of the crystal deposits. Figure 4.3 shows some SEM images of different sections of fouled membranes.

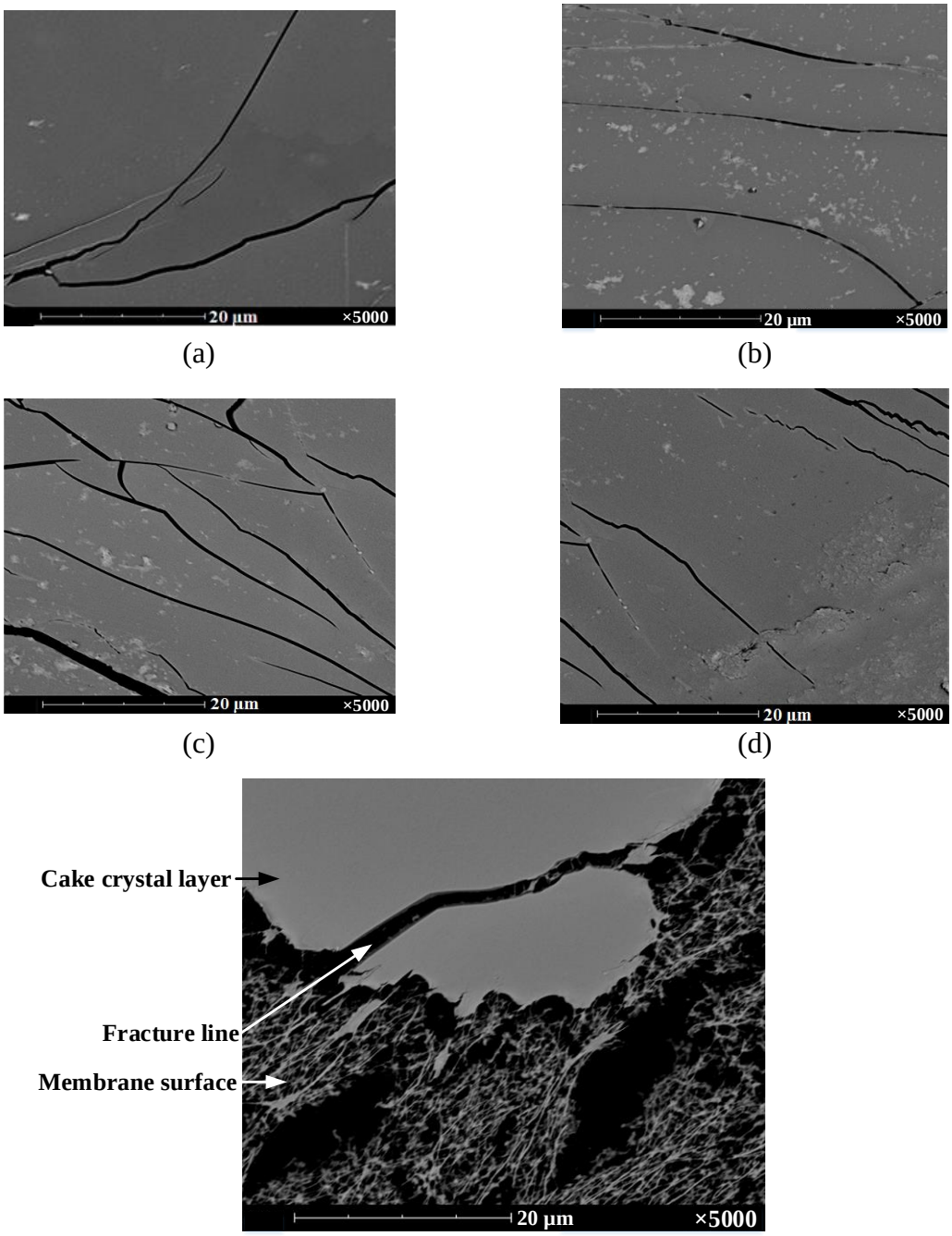

Figure 4.3. SEM micrographs of the surface sections of membranes after 2-h tests performed at the high fouling rate (RH_{air} = 10% and C_{sol}^{*} = 1.03). **Note**. Images from a first test at different locations of the membrane are shown in (**a**) and (**b**), while those from repeated tests are shown in (**c**), (**d**) and (**e**).

Figure 4.3 shows that the crystals appear in the form of cake layers on the membrane surface. In addition, it can also be observed that the cake layers are fractured. The images from different sections of the membranes in Figure 4.3 confirm that the structure of the crystal particles is consistent across various sections of a membrane from repeated tests. Similar findings are also obtained for repeated tests at other operating conditions and time intervals.

4.4.2.3 Energy dispersive X-ray spectroscopy (EDX)

EDX involves the use of a semi-conductor component to analyze the electro-magnetic energy reflected from a substance in order to determine the atomic composition of the substance [38],[111]. EDX machines are typically used in conjunction with scanning electron microscopes or transmission electron microscopes [38], and are effective for identifying the elemental composition of fouling deposits on membranes [38],[67].

An Oxford Instruments X-Max^N 50 mm^2 EDX machine is used in combination with a Hitachi SU6600 field emission scanning electron microscope to analyze the composition of deposits on a fouled membrane sample. The EDX method is hereby used to qualitatively verify the composition of crystals observed in the SEM images of fouled membranes rather than to quantify the composition of crystal deposits.

4.5 RESULTS AND DISCUSSION

In this section, the two indirect non-invasive parameter methods and three invasive methods presented in Sections 4.4.1 and 4.4.2, respectively, are used to address the objectives of this chapter (*i.e.* delineate the development of crystallization fouling in membranes and characterize fouling deposits on membranes).

4.5.1 Evolution of fouling

4.5.1.1 Indirect non-invasive parameter methods (moisture transfer flux and resistance)

Figure 4.4 depicts the evolution of fouling at two operating conditions of high and low fouling rates.

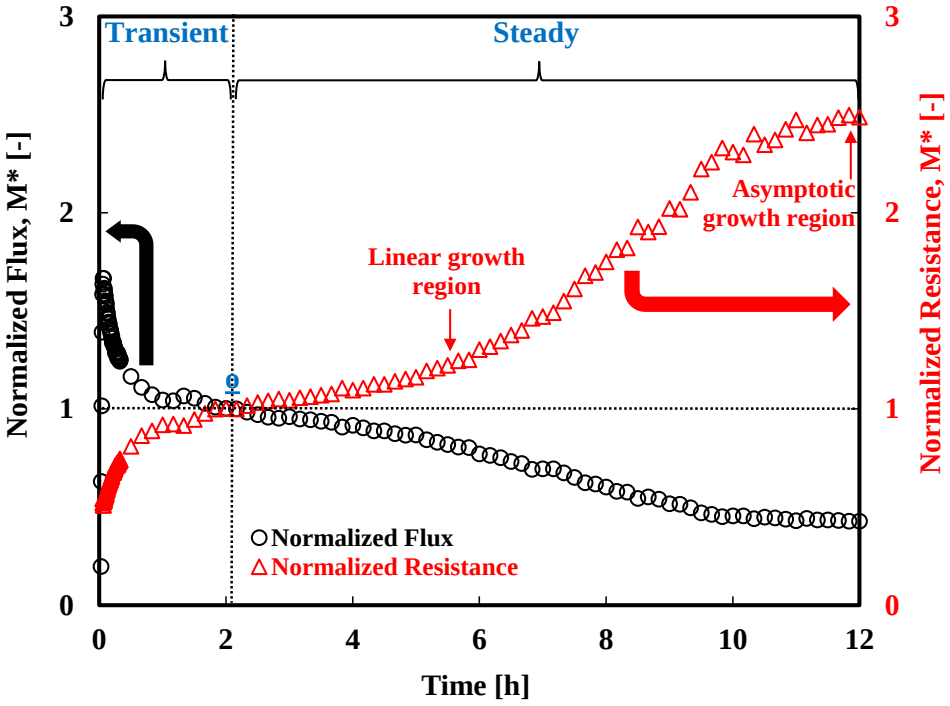

(a)

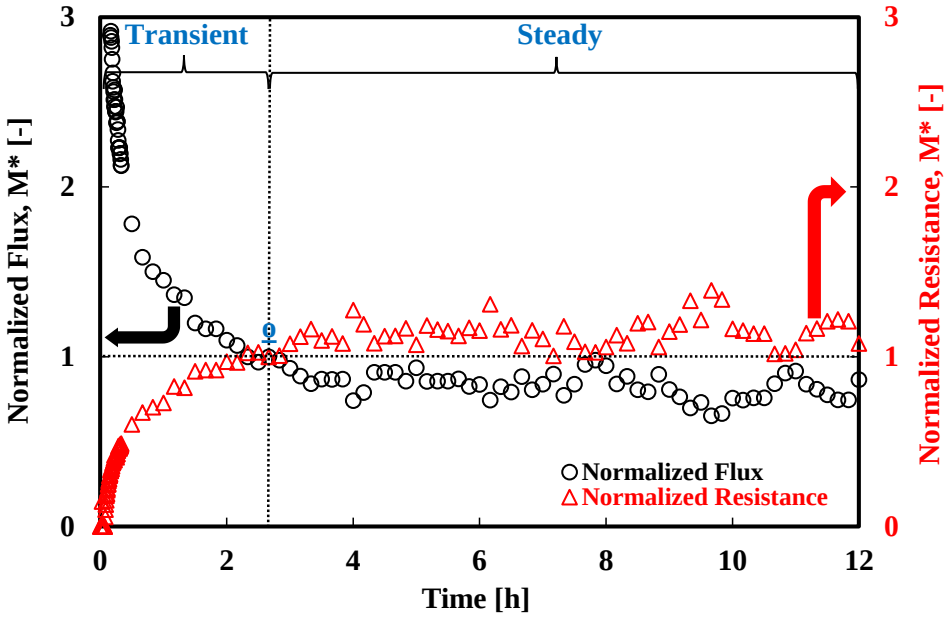

(b)

Figure 4.4. Evolution of crystallization fouling in membranes using moisture transfer flux and resistance for tests at the (**a**) high (RH_{air} = 10% and C_{sol}^{*} = 1.03) and (**b**) low (RH_{air} = 30% and C_{sol}^{*} = 1.0) fouling rates. **Note**. The start of the steady-state period of the tests, defined as when the boundary conditions of the solution at the solution-membrane interface are constant, is indicated by point (**o**).

Figure 4.4(**a**) clearly shows that the development of crystallization fouling in membranes in the test with the high fouling rate results in a rapid decay in the moisture transfer flux and corresponding increase in the moisture transfer resistance. In addition, the results in Figure 4.4(**a**) provide insight into the possible existence of the mechanisms of deposition and removal of crystals from the membrane surface during the test. The trends in Figure 4.4(**a**) have been previously described comprehensively in Section 3.5.1.3.

Figure 4.4(**b**) shows that there is a 19% decrease in moisture transfer flux and 14% increase in moisture transfer resistance during the test with the low fouling rate. The slight changes in moisture transfer flux and resistance during the test suggests that is a minimal buildup of deposits on the membrane surface. The intermittent rise and fall in moisture transfer flux and resistance is caused by periodic changes in the relative humidity of air supplied to the LAMEE.

4.5.1.2 Invasive method (SEM)

Figure 4.5 shows the SEM micrographs of membranes for tests performed at different intervals.

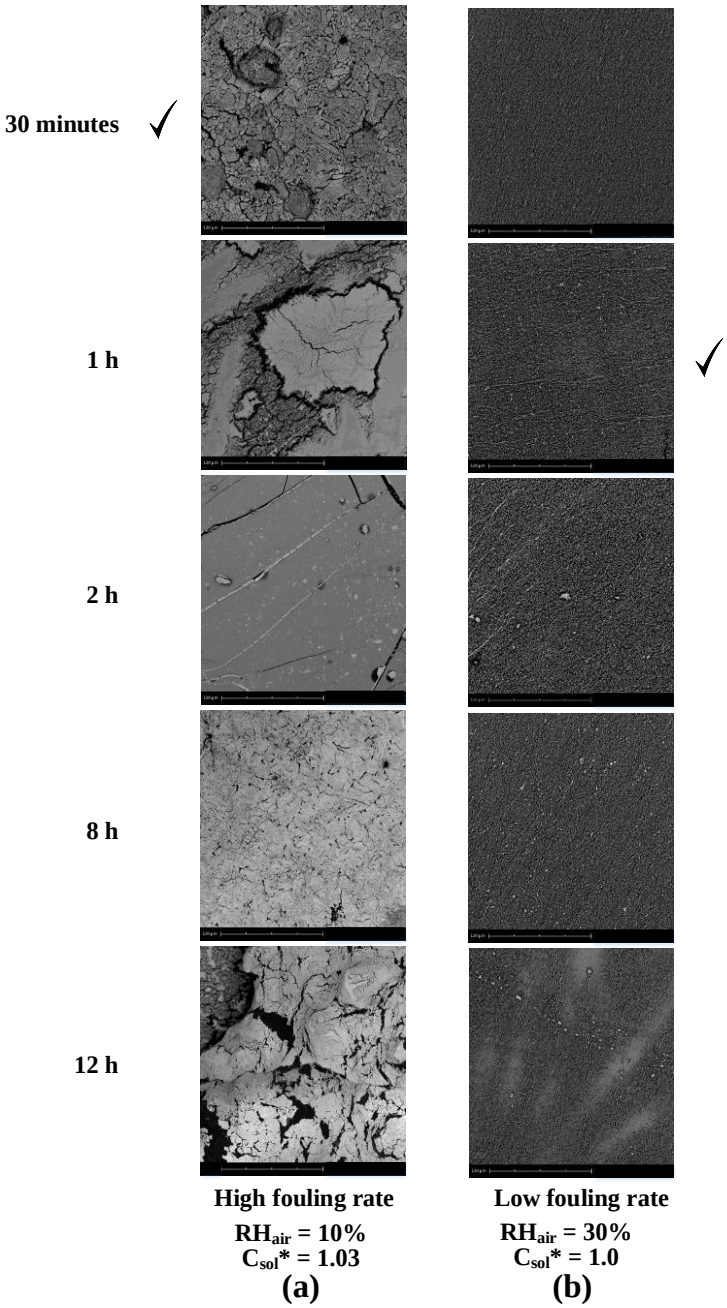

Figure 4.5. Evolution of crystallization fouling in membranes using the SEM method for tests performed at the (**a**) high (RH_{air} = 10% and C_{sol}^{*} = 1.03) and (**b**) low (RH_{air} = 30% and C_{sol}^{*} = 1.0) fouling rates. N**ote**. The time that crystals are first observed on a membrane is indicated by a check mark that is adjacent to the corresponding image. All the images are taken at a magnification of 1000 and the scale bars are 120 µm in length.

The SEM micrographs in Figure 4.5 depict the evolution of crystallization fouling in membranes, and the structural changes in the crystal deposits are described in the following paragraphs.

For the test in Figure 4.5(**a**), coarse loosely-structured rock-like crystal particles are observed within the first 30 minutes of the test, possibly due to the supersaturation of the bulk solution coupled with a high rate of moisture transfer through the membrane. As confirmed by the direct non-invasive method (*i.e.* digital microscopy) which detects the onset of fouling at 25 minutes, the high supersaturation of the bulk solution coupled with a high moisture rate possibly initiated the swift seeding of crystals during the test (*see* Figure 3.9**a**). At 1 h, several crystals are agglomerated into cake formations which can be seen on the membrane. In addition, the crystals metamorphose into smooth and fractured cake layers at the 2nd h (*see* Figure 4.3). The continuous dehydration of $MgCl_2$(aq) in the test likely led to the drying of the crystals, which resulted in crack formations and fragmentation of the cake layer within 2 – 12 h.

For the test in Figure 4.5(**b**), crystal particles are not observed on the membrane surface within the first 30 minutes. The slow development of minute crystals is first seen at 1 h, and this is confirmed by the direct non-invasive method (*i.e.* digital microscopy) which also detects the onset of fouling at 1 h (*see* Figure 3.9**b**). Thereafter, there is negligible change in the structure or distribution of the particles even at 12 h. Within 1 – 12 h of the test in Figure 4.5(**b**), the crystals remain mostly small and speckled which suggests that there is a very low rate of crystal deposition on the membrane surface rather than the agglomeration of large-size crystals or development of cake layers.

The morphological transformation in the crystal particles on the membrane surface for the test with the high fouling rate (Figure 4.5**a**) is more significant than that for the test with the low fouling rate (Figure 4.5**b**). External fouling is the governing mechanism that is observed in the tests at the high and low fouling rates. The SEM method is unable to confirm if crystals are deposited within the pores of fouled membranes (*i.e.* internal fouling) because the electron beam of the scanning electron microscope physically melts the ePTFE fibers of the membrane when the imaging magnification is significantly increased.

4.5.2 Characterization of fouling deposits (SEM, EDX)

The elemental composition of deposit formations on fouled membranes is analyzed in order to confirm if the deposits are made up of $MgCl_2 \cdot 6H_2O$ crystals. The deposits are first assessed with SEM to visualize the shape of a fully-grown crystal on a layer of agglomerated deposits (Figure 4.6), and are subsequently analyzed using SEM and EDX (Figure 4.7).

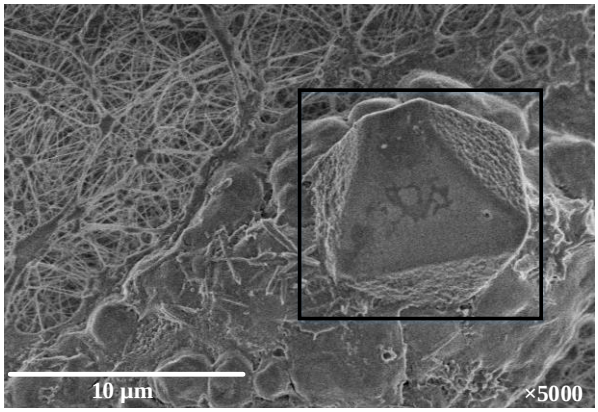

Figure 4.6. SEM micrograph of a crystal on a membrane after a 12-h test at the high fouling rate (RH_{air} = 10% and C_{sol}^{*} = 1.03). **Note**. A square is used to highlight a fully-grown crystal.

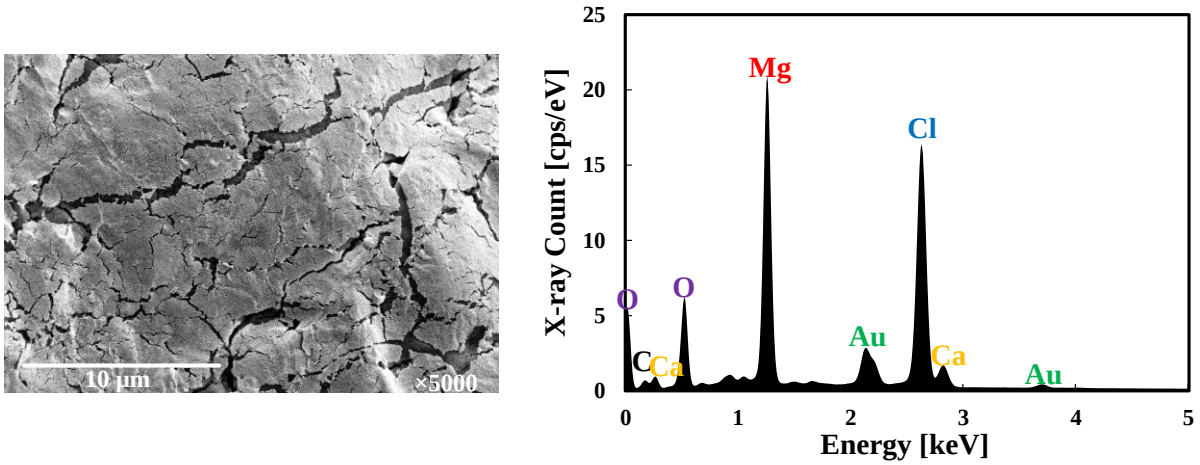

(a) SEM micrograph (b) EDX profile

Figure 4.7. The (**a**) SEM micrograph and (**b**) corresponding EDX map profile of a membrane after a 12-h test at the high fouling rate (RH_{air} = 10% and C_{sol}^{*} = 1.03). **Note**. The map profile in (**b**) corresponds to the area of the micrograph in (**a**).

Figure 4.6 clearly depicts the octahedral shape of a $MgCl_2 \cdot 6H_2O$ crystal, which is consistent with what is reported in the literature [112]. On the other hand, Figure 4.7 depicts a section of a fouled

membrane that completely overlays a perforated hole in the inner pipe (tube) of the LAMEE (*see* Figure 2.2**c**). The SEM image in Figure 4.7(**a**) shows a cake layer on the membrane, whereas the EDX plot in Figure 4.7(**b**) shows the elemental constituents of the cake layer. Expectedly, the highest peaks in Figure 4.7(**b**) correspond to Mg and Cl elements from $MgCl_2$. The O element in H_2O is detected, but H is not detected because EDX is incapable of detecting hydrogen [113],[114]. The presence of Au is detected because of the sputter coating of the membrane surface with gold. A low peak of C exists most likely because the membrane surface layer is made of carbon polymer chains, whereas the low peaks of Ca may be attributed to the presence of trace quantities of $CaCO_3$ in H_2O(aq).

A membrane section that overlays on the boundary between a perforated hole and impermeable pipe of the LAMEE is analyzed with SEM-EDX and the results are presented in Figure 4.8.

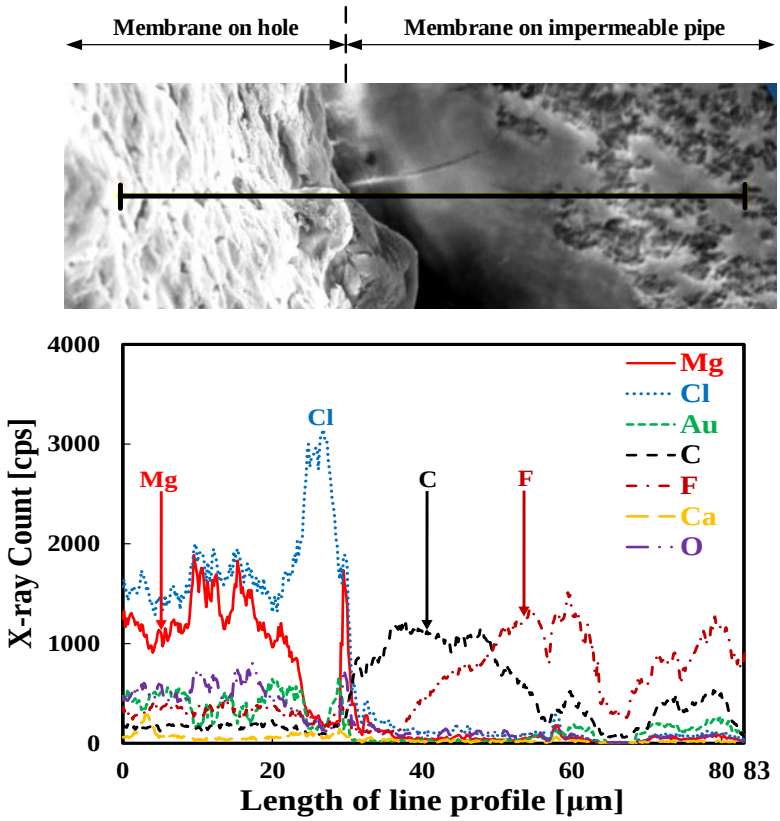

Figure 4.8. SEM image and EDX analysis of a membrane section that partially overlays on a perforated hole in the inner pipe of the LAMEE. **Note**. The results in Figure 4.8 are for a 12-h test at the high fouling rate (RH_{air} = 10% and C_{sol}^{*} = 1.03). The line in the SEM micrograph corresponds to the length scale (0 – 83 µm) in the EDX line profile.

Figure 4.8 highlights the fact that the region of the membrane that overlays on a perforated hole (*i.e.* with a high moisture transfer rate) exhibits a greater buildup of crystal deposits (Mg and Cl elements) than the membrane section outside the hole with a reduced moisture transfer rate (F and C elements). This finding confirms the hypothesis that crystallization fouling will likely occur in the regions of the membrane with high moisture transfer rates. Furthermore, there is a spike in the peaks of Mg and Cl elements at ~30 µm, because of the substantial increase in the amount of crystal deposits at the interface between the membrane covering the hole and impermeable pipe.

The SEM micrograph of the membrane in Figure 4.8 shows that the accumulation of the fouling layer increases from right to left (*i.e.* 83 to 0 µm), and the distribution of fouling is likewise confirmed in the EDX line profile. The membrane surface with less fouling (30 – 83 µm) expectedly shows the prominence of F and C elements, which are the major elements of the membrane surface layer that is made of polytetrafluorethylene $(C_2F_4)_n$. However, the F and C peaks drastically drop as the fouling layer accumulates within the region of 0 – 30 µm, because the membrane is covered with $MgCl_2 \cdot 6H_2O$ crystals and EDX only detects the composition of elements on a surface. On the other hand, the Mg, Cl and O elements do not feature within 30 – 83 µm but visibly increase in the region of 0 – 30 µm, where there is a significant buildup of crystal deposits.

4.5.3 Comparison of methods

A comparison of the characteristics of the non-invasive and invasive methods presented in the thesis is given in Table 4.1.

Table 4.1. Comparison of the non-invasive and invasive methods presented in the thesis.

Factors		Non-invasive methods			Invasive methods		
		Indirect parameter	**Indirect analysis**	**Digital microscopy**	**Optical microscopy**	**SEM**	**EDX**
Practical application	Non-invasive operation	+ +	+ +	+	–	–	–
	Online/*in situ* monitoring	+	+ +	+	–	–	–
	Financial affordability	+ +	+ +	–	–	– –	–
	Space footprint constraints	+ +	+ +	–	–	– –	–
	Installation and maintenance	+ +	+	–	–	– –	–
	Sample preparation	+ +	+ +	+ +	–	– –	– –
Operational features	Direct detection	–	– –	+	+ +	+ +	+
	Sampling rate	+ +	+ +	–	– –	– –	– –
	Calibration requirement	–	– –	–	+ +	+ +	+
	Computational demands	–	– –	–	+	+	+
Foulant analysis	Morphology	– –	– –	+	+	+ +	– –
	Topology	– –	– –	–	–	+	– –
	Spatial resolution	– –	– –	+	+	+ +	–
	Composition	– –	– –	– –	– –	– –	+ +

Note. + = Positive characteristic; + + = Very positive characteristic; – = negative characteristic; – – = Very negative characteristic. The indirect non-invasive parameter methods refer to moisture transfer flux and resistance, and the indirect non-invasive analysis methods refer to the uncertainty, statistical and slope methods.

Table 4.1 shows that the major strength of the non-invasive methods is in their real-world applicability to detect and monitor fouling in operating exchangers, whereas the invasive methods are better suited to characterize fouling deposits. In addition, a comparison of the operating features of the non-invasive and invasive methods indicates that the non-invasive methods have an almost unlimited sampling rate but have a greater demand for data processing, whereas there is a practical limitation in the sampling rate of the invasive methods. Sampling rate refers to the frequency in which data can be collected and analyzed to detect fouling.

4.6 CONCLUSION

This chapter presents the implementation of non-invasive and invasive methods to characterize the evolution of crystallization fouling in membranes that are fouled with $MgCl_2$(aq) at two operating conditions of high and low fouling rates. The non-invasive methods, which consist of two indirect non-invasive parameter methods, are used to examine the growth of fouling by monitoring moisture transfer flux and resistance *in situ*, whereas the invasive methods are used to identify the development of fouling by characterizing the morphology and composition foulants on membranes *ex situ*. The major findings from the chapter are outlined as follows:

1. Scanning electron microscopy (SEM) images of membranes show that few crystal particles are deposited on membranes in the test with the low fouling rate, whereas cake crystal formations are observed in the test with the high fouling rate. In addition, the SEM image of a crystal deposit on a membrane confirms that the deposit is $MgCl_2 \cdot 6H_2O$.
2. Energy dispersive X-ray spectroscopy (EDX) analysis indicates that the crystal deposits on membranes compose of mainly Mg, Cl and O elements.
3. The SEM–EDX results indicate that fouling occurs in the sections of a membrane with high moisture transfer rates, which confirms the hypothesis presented in Chapter 2.

CHAPTER 5

SUMMARY, CONCLUSIONS, CONTRIBUTIONS AND FUTURE WORK

The main goal of this thesis is to detect the existence and onset of crystallization fouling in a liquid-to-air membrane energy exchanger (LAMEE) through the development, calibration and application of indirect non-invasive analysis methods. Furthermore, the operating conditions that are likely to result in crystallization fouling in LAMEEs are identified, and the evolution of crystallization fouling in membranes is delineated. This chapter presents a summary of the research, the main conclusions and contributions of the thesis, and potential areas for future research.

5.1 SUMMARY AND CONCLUSIONS

In this thesis, the methods that are used to detect fouling are classified into invasive and non-invasive methods. Three invasive methods (*i.e.* optical microscopy, scanning electron microscopy, and energy dispersive X-ray spectroscopy) are used to characterize fouling deposits on membranes. The non-invasive methods are divided into direct and indirect methods. Direct non-invasive methods can be used to non-invasively and directly detect fouling. In the thesis, a direct non-invasive method (*i.e.* digital microscopy) is used to directly detect the onset of fouling. On the other hand, indirect non-invasive analysis methods can be used to non-invasively and indirectly detect fouling by analyzing measurements of indirect non-invasive parameters. In the thesis, three indirect non-invasive analysis methods (*i.e.* uncertainty, statistical and slope methods) are used to detect fouling by analyzing two indirect non-invasive parameters (*i.e.* moisture transfer flux and resistance). The invasive and non-invasive methods are used to address the two main research gaps which have been identified from the literature, which are the lack of (i) development and calibration of indirect non-invasive analysis methods to detect the onset of fouling, and (ii) comprehensive characterization of crystallization fouling in LAMEEs.

5.1.1 Objective 1: Develop non-invasive methods to detect crystallization fouling in LAMEEs

A test facility that is developed to study crystallization fouling in LAMEEs is presented in the thesis, including the uncertainty analysis and mass and energy balances. Furthermore, three indirect non-invasive analysis methods (uncertainty, statistical and slope methods) are developed to detect the onset of crystallization fouling in the LAMEE by evaluating measurements of two indirect non-invasive parameters (moisture transfer flux and resistance). A direct non-invasive method is used to determine the onset of fouling in the LAMEE by observing the initiation of crystallization fouling in membranes using a digital microscope.

Finally, the three indirect non-invasive analysis methods are calibrated using the results from the direct non-invasive method as a benchmark. The calibrated methods are subsequently applied to detect the onset of fouling in the LAMEE. The principal conclusions related to this objective are:

- Out of the three indirect non-invasive analysis methods, the slope method detects the start of crystallization fouling in the LAMEE at the earliest, and is closely followed by the statistical method. The uncertainty method is the least sensitive method and is the least to detect fouling.
- Digital microscopy, which is a direct non-invasive method, is the most sensitive method to detect the onset of crystallization fouling in LAMEEs. Digital microscopy can detect the start of fouling at an earlier time than the indirect non-invasive analysis methods by a factor of three to eight.
- The calibrated indirect non-invasive analysis methods can effectively detect the onset of fouling in the LAMEE (within ±5 minutes of the digital microscopy method), when they are applied to the same operating condition as the calibration. However, substantial discrepancies of up to 30 minutes are observed when the calibrated methods are applied to detect fouling at operating conditions that are different from the conditions used for the calibration.

5.1.2 Objective 2: Identify operating conditions that result in crystallization fouling in LAMEEs

A hypothesis that states that crystallization fouling in the LAMEE can be reduced by reducing the rate of moisture transfer through the membrane is tested. The hypothesis is tested by using three indirect non-invasive analysis methods to compare fouling at different moisture transfer fluxes created by different operating conditions and membranes. Two invasive methods are also used to test the hypothesis, by assessing the distribution of fouling deposits on a membrane surface using scanning electron microscopy (SEM) and energy dispersive X-ray spectroscopy (EDX). The main conclusions related to this objective are:

- The rate of crystallization fouling in the LAMEE is dependent on two key parameters: solution concentration (degree of supersaturation of the desiccant solution) and relative humidity of air.
- The membrane with a lower vapor diffusion resistance (VDR) produces a higher moisture transfer flux, which initiates crystallization fouling earlier in the LAMEE and increases the fouling rate than the membrane with higher VDR. Furthermore, the asymptotic moisture transfer flux and resistance of the LAMEE is identical for both membranes with high and low VDRs. This implies that the use of a better membrane (*i.e.* lower VDR) may not positively affect the performance of the LAMEE once fouling is initiated.
- Crystallization fouling mostly occurs in the regions of a membrane with high moisture transfer rates.

5.1.3 Objective 3: Identify the evolution of crystallization fouling in membranes

The evolution and mechanisms of crystallization fouling in membranes are studied at two operating conditions (high and low fouling rates) using non-invasive and invasive methods. The regimes of crystallization fouling are identified by non-invasively monitoring the changes in moisture transfer flux and resistance. Two invasive methods (*i.e.* optical microscopy and SEM) are used to identify the morphology of the fouling deposits as a function of time. Furthermore, an invasive method (EDX) is used to identify the constituent elements of the fouling deposits. The principal conclusions related to this objective are:

- Crystallization fouling develops in the LAMEE initially at a linear rate, and gradually approaches an asymptotic limit over time. In a 12-h test at the high fouling rate, crystallization fouling is observed to reach an asymptotic point at 11 h.
- SEM micrographs of fouled membranes show that there is a substantial deposition of crystal particles on membranes in the test with the high fouling rate, whereas few crystals are deposited on membranes in the test with the low fouling rate.
- The fouling deposits are confirmed to be $MgCl_2 \cdot 6H_2O$ crystals, because the (i) SEM images show the octahedral shape of the crystals, and (ii) EDX profiles indicate that the crystal deposits consist of primarily Mg, Cl and O elements.

5.2 CONTRIBUTIONS

This thesis provides the following original contributions to the scientific literature.

5.2.1 Development and calibration of indirect non-invasive analysis methods to detect fouling in a LAMEE

- A major contribution of this thesis is the development of indirect non-invasive analysis methods that can be used to detect the onset of fouling in a LAMEE. The methods have several advantages including (i) a high sensitivity to rapidly detect the start of fouling, (ii) capacity to monitor fouling in real-time, and (iii) adaptability to other process measurements. The methods are useful for practical applications and offer potential energy and economic savings, because they can detect fouling early in an exchanger before losses arise from the accumulation of deposits.
- The indirect non-invasive analysis methods are also calibrated with a direct non-invasive method. The calibration technique implemented in the thesis uses a benchmark that is based on a non-invasive method (digital microscopy) that is applied to directly detect the start of fouling, rather than a design parameter or arbitrary set-point.

5.2.2 Operating conditions that result in crystallization fouling in LAMEEs

- The operating conditions that can result in crystallization fouling are investigated in the thesis by identifying the influence of two key parameters on crystallization fouling in a LAMEE. This analysis has not been performed for membrane exchangers used for heating, ventilating and air-conditioning (HVAC) applications. Manufacturers of LAMEEs can use

the results of this thesis to set operational constraints on the identified parameters in order to minimize the likelihood of crystallization fouling during the operation of the LAMEE.

- The impact of moisture transfer rate on crystallization fouling in a LAMEE is assessed and quantified in this thesis. This constitutes a major finding and contribution to the literature, because the fact that a high moisture transfer flux through the membrane can increase crystallization fouling in the LAMEE had not been previously established. This contribution highlights the fact that an optimization may be needed in the design of LAMEEs in order to maximize the long-term moisture transfer rate and reduce the possibility of fouling.
- The impact of membrane resistance on crystallization fouling in a LAMEE is assessed and quantified. The thesis demonstrates that the performance of a LAMEE is the same when fouling reaches an asymptotic stage, regardless of the vapor diffusion resistance of the membrane. Consequently, the technical and economic investment in high-quality membranes may not lead to LAMEEs with a higher long-term performance if fouling is not quickly detected and controlled.

5.2.3 Evolution of crystallization fouling in membranes

- The evolution and mechanisms of crystallization fouling in membranes are identified in this thesis. This is an important contribution from this thesis because previous studies have not used both non-invasive and invasive methods to identify the evolution and mechanisms of crystallization fouling in membranes that are exposed to the operating conditions found in LAMEEs and typical liquid desiccant HVAC systems.
- The growth regimes of crystallization fouling in LAMEEs are identified, and shown to be consistent with what has been observed in heat exchangers by previous researchers.

5.2.4 Characterization of crystal deposits on fouled membranes

- None of the previous studies on fouling in membrane exchangers for HVAC applications analyzed the composition of deposit formations on fouled membranes. However, the morphology and elemental composition of crystal deposits on a fouled membrane are analyzed in this thesis. Furthermore, the characterization of the spatial morphology and composition of fouling deposits reinforces the contribution that a higher rate of moisture transfer through membranes increases the tendency for crystallization fouling in LAMEEs.

5.3 FUTURE WORK

The following areas are recommended for future research based on the work in this thesis.

5.3.1 Sensitivity studies on fouling

The experiments in this thesis were performed at conditions that would be extreme in operating conditions for LAMEEs in HVAC systems in order to accelerate the fouling tests. Therefore, additional sensitivity studies are recommended and outlined as follows:

- It is recommended to assess the effect of temperature on crystallization fouling in LAMEEs, by performing experiments at less extreme conditions for both the air stream and liquid desiccant solution. This will provide insight into the effect of temperature on both the moisture transfer rate and kinetics of crystallization fouling in the LAMEE.
- The experiments performed in this thesis involved the use of $MgCl_2$(aq). In subsequent studies, it is recommended to carry out a systematic assessment of the impact of other commonly used desiccant solutions (*e.g.* LiCl(aq), $CaCl_2$(aq)) on crystallization fouling in LAMEEs.
- In this thesis, a stagnant liquid desiccant solution was used in the LAMEE. However, the solution is a flowing fluid stream in LAMEEs. It is suggested to assess the impact of a flowing desiccant solution at different flow rates on crystallization fouling in operating LAMEEs. This can provide insight into the dominant mechanisms (diffusion or reaction-controlled) of crystallization fouling at different solution velocities. Furthermore, the effect of shear stresses at different solution velocities on the removal of crystallization fouling in the LAMEE can be evaluated.

5.3.2 Investigation of long-term fouling

- The experiments reported in this thesis were limited to 12 h. However, short-term fouling tests do not provide comprehensive insight into the growth and dynamics of crystallization fouling in operating LAMEEs. Consequently, it is suggested to study the effect of crystallization fouling on the performance of LAMEEs over a longer period of time at less extreme temperature and humidity conditions. The testing of the long-term effect of crystallization fouling on the LAMEE can provide insight into the (i) effect of ageing on fouling deposits, (ii) impact of changing conditions on crystallization fouling in the

LAMEE, and (iii) service life of a LAMEE when crystallization fouling occurs in the membrane.

5.3.3 Prevention and cleaning of fouling

- In this thesis, it was established that crystallization fouling in the LAMEE can be controlled by reducing the rate of moisture transfer through the membrane. It is suggested to assess other techniques that can be used to prevent crystallization fouling in LAMEEs, such as the addition of inhibitors to liquid desiccants and modification of the surface properties of membranes.
- It is recommended to evaluate the effectiveness of different cleaning techniques (such as backwashing or chemical cleaning) for the removal of crystal deposits from the membranes fouled in LAMEEs.

5.3.4 Modeling of fouling

An experimental approach was exclusively used to study fouling in this thesis. Modeling was not pursued because the data set was limited. To develop a model, a wider range of experimental tests is needed which is outside the scope of the thesis. The following task is therefore recommended for future work:

- It is suggested to test the LAMEE under a wider range of operating conditions as outlined in Section 5.3.1. Afterwards, an empirical model (such as the Kern-Seaton model [32]) can be used to fit the experimental measurements, in order to identify the mechanisms of fouling and predict crystallization fouling in the LAMEE at different operating conditions.

REFERENCES

[1] Shah, R. K.; Sekulić, D. P. Fouling and Corrosion. In *Fundamentals of Heat Exchanger Design*; John Wiley & Sons, Inc.: Hoboken, NJ, 2003; pp 863–905.

[2] Field, R. Fundamentals of Fouling. In *Membrane Technology*; Peinemann, K.-V., Ed.; Wiley-VCH Verlag GmbH & Co. KGaA: Weinheim, Germany, 2010; Vol. 4, pp 1–23.

[3] Assis, B. C. G.; Lemos, J. C.; Liporace, F. S.; Oliveira, S. G.; Queiroz, E. M.; Pessoa, F. L. P.; Costa, A. L. H. Dynamic optimization of the flow rate distribution in heat exchanger networks for fouling mitigation. *Industrial & Engineering Chemistry Research* 2015, *54* (25), 6497–6507.

[4] Shirazi, S.; Lin, C.-J.; Chen, D. Inorganic fouling of pressure-driven membrane processes – A critical review. *Desalination* 2010, *250* (1), 236–248.

[5] Guo, W.; Ngo, H.-H.; Li, J. A mini-review on membrane fouling. *Bioresource Technology* 2012, *122*, 27–34.

[6] Müller-Steinhagen, H.; Malayeri, M. R.; Watkinson, A. P. Heat exchanger fouling: Environmental impacts. *Heat Transfer Engineering* 2009, *30* (10–11), 773–776.

[7] Zhao, X.; Chen, X. D. A Critical Review of Basic Crystallography to Salt Crystallization Fouling in Heat Exchangers. *Heat Transfer Engineering* 2012, *34* (8–9), 719–732.

[8] The World Bank Group. GNI, PPP (current international $) - Canada http://data.worldbank.org/indicator/NY.GNP.MKTP.PP.CD?locations=CA (accessed Aug 3, 2017).

[9] The World Bank Group. GNI, PPP (current international $) - United States http://data.worldbank.org/indicator/NY.GNP.MKTP.PP.CD?locations=US (accessed Aug 8, 2017).

[10] Pérez-Lombard, L.; Ortiz, J.; Pout, C. A review on buildings energy consumption information. *Energy and Buildings* 2008, *40* (3), 394–398.

[11] Levermore, G. J. A review of the IPCC Assessment Report Four, Part 1: The IPCC process and greenhouse gas emission trends from buildings worldwide. *Building Services Engineering Research and Technology* 2008, *29* (4), 349–361.

[12] Isaac, M.; van Vuuren, D. P. Modeling global residential sector energy demand for heating and air conditioning in the context of climate change. *Energy Policy* 2009, *37* (2), 507–521.

[13] Yu, B. F.; Hu, Z. B.; Liu, M.; Yang, H. L.; Kong, Q. X.; Liu, Y. H. Review of research on air-conditioning systems and indoor air quality control for human health. *International Journal of Refrigeration* 2009, *32* (1), 3–20.

[14] Shen, C.; Cirone, C.; Jacobi, A. M.; Wang, X. Fouling of enhanced tubes for condensers used in cooling tower systems: A literature review. *Applied Thermal Engineering* 2015, *79*, 74–87.

[15] Qureshi, B. A.; Zubair, S. M. The impact of fouling on performance evaluation of evaporative coolers and condensers. *International Journal of Energy Research* 2005, *29* (14), 1313–1330.

[16] Inamdar, H.; Groll, E. A.; Weibel, J. A.; Garimella, S. Prediction of air-side particulate fouling of HVAC&R heat exchangers. *Applied Thermal Engineering* 2016, *104*, 720–733.

[17] Zdaniuk, G. J.; Chamra, L. M.; Mago, P. J. A survey of cooling tower water quality for condenser tube fouling potential. *Proceedings of the Institution of Mechanical Engineers, Part A: Journal of Power and Energy* 2008, *222* (1), 111–122.

[18] Shen, C.; Cirone, C.; Wang, X. Uncertainty analysis: Design of a fouling test device for the liquid-to-refrigerant heat exchangers. *Applied Thermal Engineering* 2015, *85*, 148–159.

[19] Yang, L.; Braun, J. E.; Groll, E. A. The impact of evaporator fouling and filtration on the performance of packaged air conditioners. *International Journal of Refrigeration* 2007, *30* (3), 506–514.

[20] Veronica, D. A. Detecting cooling coil fouling automatically – Part 1: A novel concept. *HVAC and R Research* 2010, *16* (4), 413–433.

[21] Pak, B. C.; Groll, E. A.; Braun, J. E. Impact of fouling and cleaning on plate fin and spine fin heat exchanger performance. *ASHRAE Transactions* 2005, *111* (1), 496–504.

[22] Wright, S.; Andrews, G.; Sabir, H. A review of heat exchanger fouling in the context of aircraft air-conditioning systems, and the potential for electrostatic filtering. *Applied Thermal Engineering* 2009, *29* (13), 2596–2609.

[23] Cremaschi, L.; Wu, X. Effect of Fouling on the Thermal Performance of Condensers and on the Water Consumption in Cooling Tower Systems. *Heat Transfer Engineering* 2015, *36* (7–8), 663–675.

[24] Cremaschi, L.; Barve, A.; Wu, X. Effect of condensation temperature and water quality on fouling of brazed-plate heat exchangers. *ASHRAE Transactions* 2012, *118* (1), 1086–1100.

[25] Charles, N. T.; Johnson, D. W. The occurrence and characterization of fouling during membrane evaporative cooling. *Journal of Membrane Science* 2008, *319* (1–2), 44–53.

[26] Crawford, R.; da Silva, A. K. Experimental testing of a passive, evaporation-based roof cooling system. *Energy and Buildings* 2014, *71*, 12–19.

[27] Engarnevis, A.; Huizing, R.; Green, S.; Rogak, S. Particulate fouling assessment in membrane based air-to-air energy exchangers. *Energy and Buildings* 2017, *150*, 477–487.

[28] Woods, J. Membrane processes for heating, ventilation, and air conditioning. *Renewable and Sustainable Energy Reviews* 2014, *33*, 290–304.

[29] Ge, G.; Abdel-Salam, M. R. H.; Besant, R. W.; Simonson, C. J. Research and applications of liquid-to-air membrane energy exchangers in building HVAC systems at University of Saskatchewan: A review. *Renewable and Sustainable Energy Reviews* 2013, *26*, 464–479.

[30] Abdel-Salam, M. R. H.; Ge, G.; Fauchoux, M.; Besant, R. W.; Simonson, C. J. State-of-the-art in liquid-to-air membrane energy exchangers (LAMEEs): A comprehensive review. *Renewable and Sustainable Energy Reviews* 2014, *39*, 700–728.

[31] Abdel-Salam, M. R. H.; Fauchoux, M.; Ge, G.; Besant, R. W.; Simonson, C. J. Expected energy and economic benefits, and environmental impacts for liquid-to-air membrane energy exchangers (LAMEEs) in HVAC systems: A review. *Applied Energy* 2014, *127*, 202–218.

[32] Müller-Steinhagen, H. Heat transfer fouling: 50 years after the Kern and Seaton model. *Heat Transfer Engineering* 2011, *32* (1), 1–13.

[33] Suwal, S.; Doyen, A.; Bazinet, L. Characterization of protein, peptide and amino acid fouling on ion-exchange and filtration membranes: Review of current and recently developed methods. *Journal of Membrane Science* 2015, *496*, 267–283.

[34] Li, X.; Mo, Y.; Li, J.; Guo, W.; Ngo, H. H. In-situ monitoring techniques for membrane fouling and local filtration characteristics in hollow fiber membrane processes: A critical review. *Journal of Membrane Science* 2017, *528*, 187–200.

[35] Wallhäußer, E.; Hussein, M. A.; Becker, T. Detection methods of fouling in heat exchangers in the food industry. *Food Control* 2012, *27* (1), 1–10.

[36] Gryta, M. Water desalination using membrane distillation with acidic stabilization of scaling layer thickness. *Desalination* 2015, *365*, 160–166.

[37] Feng, B.; Fang, Z.; Hou, J.; Ma, X.; Huang, Y.; Huang, L. Effects of heavy metal wastewater on the anoxic/aerobic-membrane bioreactor bioprocess and membrane fouling. *Bioresource Technology* 2013, *142*, 32–38.

[38] Tijing, L. D.; Woo, Y. C.; Choi, J.-S.; Lee, S.; Kim, S.-H.; Shon, H. K. Fouling and its control in membrane distillation – A review. *Journal of Membrane Science* 2015, *475*, 215–244.

[39] Zarebska, A.; Nieto, D.; Christensen, K.; Norddahl, B. Ammonia recovery from agricultural wastes by membrane distillation: Fouling characterization and mechanism. *Water Research* 2014, *56*, 1–10.

[40] Zhao, Z.-P.; Xu, L.; Shang, X.; Chen, K. Water regeneration from human urine by vacuum membrane distillation and analysis of membrane fouling characteristics. *Separation and Purification Technology* 2013, *118*, 369–376.

[41] Naidu, G.; Jeong, S.; Vigneswaran, S.; Hwang, T.-M.; Choi, Y.-J.; Kim, S.-H. A review on fouling of membrane distillation. *Desalination and Water Treatment* 2015, *57* (22), 10052–10076.

[42] Warsinger, D. M.; Swaminathan, J.; Guillen-Burrieza, E.; Arafat, H. A.; Lienhard V, J. H. Scaling and fouling in membrane distillation for desalination applications: A review. *Desalination* 2015, *356*, 294–313.

[43] Sanmartino, J. A.; Khayet, M.; García-Payo, M. C.; El Bakouri, H.; Riaza, A. Desalination and concentration of saline aqueous solutions up to supersaturation by air gap membrane distillation and crystallization fouling. *Desalination* 2016, *393*, 39–51.

[44] Shi, X.; Tal, G.; Hankins, N. P.; Gitis, V. Fouling and cleaning of ultrafiltration membranes: A review. *Journal of Water Process Engineering* 2014, *1*, 121–138.

[45] Antony, A.; Low, J. H.; Gray, S.; Childress, A. E.; Le-Clech, P.; Leslie, G. Scale formation and control in high pressure membrane water treatment systems: A review. *Journal of Membrane Science* 2011, *383* (1–2), 1–16.

[46] Gryta, M. Fouling in direct contact membrane distillation process. *Journal of Membrane Science* 2008, *325* (1), 383–394.

[47] Gudmundsson, O.; Palsson, O.; Palsson, H.; Lalot, S. Online fouling detection of domestic hot water heat exchangers. *Heat Transfer Engineering* 2016, *37* (15), 1231–1241.

[48] Young, A.; Venditti, S.; Berrueco, C.; Yang, M.; Waters, A.; Davies, H.; Hill, S.; Millan, M.; Crittenden, B. Characterization of crude oils and their fouling deposits using a batch stirred cell system. *Heat Transfer Engineering* 2011, *32* (3–4), 216–227.

[49] Jonsson, G. R.; Lalot, S.; Palsson, O. P.; Desmet, B. Use of extended Kalman filtering in detecting fouling in heat exchangers. *International Journal of Heat and Mass Transfer* 2007, *50* (13–14), 2643–2655.

[50] Ge, J.; Peng, Y.; Li, Z.; Chen, P.; Wang, S. Membrane fouling and wetting in a DCMD process for RO brine concentration. *Desalination* 2014, *344*, 97–107.

[51] Wallhäußer, E.; Hussein, W. B.; Hussein, M. A.; Hinrichs, J.; Becker, T. Detection of dairy fouling: Combining ultrasonic measurements and classification methods. *Engineering in Life Sciences* 2013, *13* (3), 292–301.

[52] Wallhäußer, E.; Sayed, A.; Nöbel, S.; Hussein, M. A.; Hinrichs, J.; Becker, T. Determination of cleaning end of dairy protein fouling using an online system combining ultrasonic and classification methods. *Food and Bioprocess Technology* 2014, *7* (2), 506–515.

[53] Virtanen, T.; Reinikainen, S.-P.; Kögler, M.; Mänttäri, M.; Viitala, T.; Kallioinen, M. Real-time fouling monitoring with Raman spectroscopy. *Journal of Membrane Science* 2017, *525*, 312–319.

[54] Tun, C. M.; Fane, A. G.; Matheickal, J. T.; Sheikholeslami, R. Membrane distillation crystallization of concentrated salts – flux and crystal formation. *Journal of Membrane Science* 2005, *257* (1–2), 144–155.

[55] Tachtatzis, C.; Sheridan, R.; Michie, C.; Atkinson, R. C.; Cleary, A.; Dziewierz, J.; Andonovic, I.; Briggs, N. E. B.; Florence, A. J.; Sefcik, J. Image-based monitoring for early detection of fouling in crystallisation processes. *Chemical Engineering Science* 2015, *133* (8), 82–90.

[56] Lalot, S.; Desmet, B. The lock-in technique applied to heat exchangers: A semi-analytical approach and its application to fouling detection. *Applied Thermal Engineering* 2017, *114*, 154–162.

[57] Andrade Becheleni, E. M.; Borba, R. P.; Seckler, M. M.; Ferreira Rocha, S. D. Water recovery from saline streams produced by electrodialysis. *Environmental Technology* 2015, *36* (3), 386–394.

[58] Wang, L.; Li, B.; Gao, X.; Wang, Q.; Lu, J.; Wang, Y.; Wang, S. Study of membrane fouling in cross-flow vacuum membrane distillation. *Separation and Purification Technology* 2014, *122*, 133–143.

[59] Ho, J. S.; Sim, L. N.; Webster, R. D.; Viswanath, B.; Coster, H. G. L.; Fane, A. G. Monitoring fouling behavior of reverse osmosis membranes using electrical impedance spectroscopy: A field trial study. *Desalination* 2017, *407*, 75–84.

[60] Kimura, K.; Ogyu, R.; Miyoshi, T.; Watanabe, Y. Transition of major components in irreversible fouling of MBRs treating municipal wastewater. *Separation and Purification Technology* 2015, *142*, 326–331.

[61] Tuladhar, T. R.; Paterson, W. R.; Macleod, N.; Wilson, D. I. Development of a novel non-contact proximity gauge for thickness measurement of soft deposits and its application in fouling studies. *The Canadian Journal of Chemical Engineering* 2000, *78* (5), 935–947.

[62] Wang, S.; Wilson, D. I. Zero-discharge fluid-dynamic gauging for studying the swelling of soft solid layers. *Industrial & Engineering Chemistry Research* 2015, *54* (32), 7859–7870.

[63] Zan, C.; Shi, L.; Yang, W.; Ma, X. Evolution of composite fouling on a vertical stainless steel surface caused by treated sewage. *Frontiers of Energy and Power Engineering in China* 2010, *4* (2), 171–180.

[64] Lyster, E.; Kim, M.; Au, J.; Cohen, Y. A method for evaluating antiscalant retardation of crystal nucleation and growth on RO membranes. *Journal of Membrane Science* 2010, *364* (1), 122–131.

[65] Bartman, A. R.; Lyster, E.; Rallo, R.; Christofides, P. D.; Cohen, Y. Mineral scale monitoring for reverse osmosis desalination via real-time membrane surface image analysis. *Desalination* 2011, *273* (1), 64–71.

[66] Phattaranawik, J.; Fane, A. G.; Wong, F. S. Novel membrane-based sensor for online membrane integrity monitoring. *Journal of Membrane Science* 2008, *323* (1), 113–124.

[67] Thompson, J.; Rahardianto, A.; Kim, S.; Bilal, M.; Breckenridge, R.; Cohen, Y. Real-time direct detection of silica scaling on RO membranes. *Journal of Membrane Science* 2017, *528*, 346–358.

[68] Lalot, S.; Pálsson, H. Detection of fouling in a cross-flow heat exchanger using a neural network based technique. *International Journal of Thermal Sciences* 2010, *49* (4), 675–679.

[69] Pääkkönen, T. M.; Riihimäki, M.; Simonson, C. J.; Muurinen, E.; Keiski, R. L. Crystallization fouling of $CaCO_3$ – Analysis of experimental thermal resistance and its uncertainty. *International Journal of Heat and Mass Transfer* 2012, *55* (23–24), 6927–6937.

[70] Wallhäußer, E.; Hussein, W. B.; Hussein, M. A.; Hinrichs, J.; Becker, T. M. On the usage of acoustic properties combined with an artificial neural network – A new approach of determining presence of dairy fouling. *Journal of Food Engineering* 2011, *103* (4), 449–456.

[71] Xu, X.; Li, J.; Li, H.; Cai, Y.; Cao, Y.; He, B.; Zhang, Y. Non-invasive monitoring of fouling in hollow fiber membrane via UTDR. *Journal of Membrane Science* 2009, *326* (1), 103–110.

[72] Graf von der Schulenburg, D. A.; Vrouwenvelder, J. S.; Creber, S. A.; van Loosdrecht, M. C. M.; Johns, M. L. Nuclear magnetic resonance microscopy studies of membrane biofouling. *Journal of Membrane Science* 2008, *323* (1), 37–44.

[73] Gao, Y.; Haavisto, S.; Li, W.; Tang, C. Y.; Salmela, J.; Fane, A. G. Novel approach to characterizing the growth of a fouling layer during membrane filtration via optical coherence tomography. *Environmental Science & Technology* 2014, *48* (24), 14273–14281.

[74] Epstein, N. Thinking about heat transfer fouling: A 5 x 5 matrix. *Heat Transfer Engineering* 1983, *4* (1), 43–56.

[75] Jain, S.; Bansal, P. K. Performance analysis of liquid desiccant dehumidification systems. *International Journal of Refrigeration* 2007, *30* (5), 861–872.

[76] Mei, L.; Dai, Y. J. A technical review on use of liquid-desiccant dehumidification for air-conditioning application. *Renewable and Sustainable Energy Reviews* 2008, *12* (3), 662–689.

[77] Lowenstein, A. Review of liquid desiccant technology for HVAC applications. *HVAC and R Research* 2008, *14* (6), 819–839.

[78] Jain, S.; Dhar, P. L.; Kaushik, S. C. Experimental studies on the dehumidifier and regenerator of a liquid desiccant cooling system. *Applied Thermal Engineering* 2000, *20* (3), 253–267.

[79] Geddert, T.; Augustin, W.; Scholl, S. Induction time in crystallization fouling on heat transfer surfaces. *Chemical Engineering & Technology* 2011, *34* (8), 1303–1310.

[80] Srisurichan, S.; Jiraratananon, R.; Fane, A. G. Mass transfer mechanisms and transport resistances in direct contact membrane distillation process. *Journal of Membrane Science* 2006, *277* (1–2), 186–194.

[81] Bott, T. R. Aspects of crystallization fouling. *Experimental Thermal and Fluid Science* 1997, *14* (4), 356–360.

[82] Walker, P.; Sheikholeslami, R. Assessment of the effect of velocity and residence time in $CaSO_4$ precipitating flow reaction. *Chemical Engineering Science* 2003, *58* (16), 3807–3816.

[83] Mullin, J. W. *Crystallization*, fourth ed.; Reed Educational and Professional Publishing Ltd: Oxford, England, 2001.

[84] Bansal, B.; Chen, X. D.; Müller-Steinhagen, H. Analysis of "classical" deposition rate law for crystallisation fouling. *Chemical Engineering and Processing: Process Intensification* 2008, *47* (8), 1201–1210.

[85] Bott, T. R. Crystallisation and Scale Formation. In *Fouling of Heat Exchangers*, first ed.; Elsevier Science: Amsterdam, Netherlands, 1995; pp 97–103.

[86] Beriault, D. A. Run-around membrane energy exchanger prototype 4 design and laboratory testing, MSc Thesis, University of Saskatchewan: Saskatoon, SK, 2011.

[87] Namvar, R.; Pyra, D.; Ge, G.; Simonson, C. J.; Besant, R. W. Transient characteristics of a liquid-to-air membrane energy exchanger (LAMEE) experimental data with correlations. *International Journal of Heat and Mass Transfer* 2012, *55* (23–24), 6682–6694.

[88] Zaytsev, I. D.; Aseyev, G. G. *Properties of Aqueous Solutions of Electrolytes*; CRC Press: Boca Raton, FL, 1992.

[89] Hart Scientific. *9105/9107 Dry-well Calibrator User's Guide*; Utah, 2002.

[90] Thunder Scientific® Corporation. Model 1200 Mini "Two-Pressure" Humidity Generator http://www.thunderscientific.com/humidity_equipment/model_1200.html (accessed Mar 21, 2017).

[91] MKS Instruments Inc. *MKS Instruction Manual: Type 258C/1258C/2258C Mass Flow Meters Type 1259C/2259C Mass Flow Controllers*; Technical Report No. 111858-P1 REV A, Andover, MA, 1990.

[92] Abdel-Salam, M. R. H.; Besant, R. W.; Simonson, C. J. Design and testing of a novel 3-fluid liquid-to-air membrane energy exchanger (3-fluid LAMEE). *International Journal of Heat and Mass Transfer* 2016, *92*, 312–329.

[93] ASME/ANSI. *Performance Test Code 19.1 Test Uncertainty: Instruments and Apparatus*; New York, NY, 1998.

[94] Figliola, R. S.; Beasley, D. E. *Theory and Design for Mechanical Measurements*, fourth ed.; John Wiley & Sons, Inc.: Hoboken, NJ, 2006.

[95] Iskra, C. R. Convective mass transfer between a hydrodynamically developed airflow and liquid water with and without a vapor permeable membrane, MSc Thesis, University of Saskatchewan, 2007.

[96] Stamatis, D. H. *Essential Statistical Concepts for the Quality Professional*, first ed.; CRC Press: Boca Raton, FL, 2012.

[97] Ge, G.; Mahmood, G. I.; Moghaddam, D. G.; Simonson, C. J.; Besant, R. W.; Hanson, S.; Erb, B.; Gibson, P. W. Material properties and measurements for semi-permeable membranes used in energy exchangers. *Journal of Membrane Science* 2014, *453*, 328–336.

[98] Ge, G.; Ghadiri Moghaddam, D.; Abdel-Salam, A. H.; Besant, R. W.; Simonson, C. J. Comparison of experimental data and a model for heat and mass transfer performance of a liquid-to-air membrane energy exchanger (LAMEE) when used for air dehumidification and salt solution regeneration. *International Journal of Heat and Mass Transfer* 2014, *68*, 119–131.

[99] Abdel-Salam, A. H.; Simonson, C. J. State-of-the-art in liquid desiccant air conditioning equipment and systems. *Renewable and Sustainable Energy Reviews* 2016, *58*, 1152–1183.

[100] Mayer, M.; Bucko, J.; Benzinger, W.; Dittmeyer, R.; Augustin, W.; Scholl, S. Crystallization fouling in experimental micro heat exchangers – Optical and thermal investigations. *Experimental Heat Transfer* 2013, *26* (5), 487–502.

[101] National Institute of Health. ImageJ: Image Processing and Analysis in Java https://imagej.nih.gov/ij/ (accessed Aug 18, 2017).

[102] Wang, J.; Zamani, F.; Cahyadi, A.; Toh, J. Y.; Yang, S.; Wu, B.; Liu, Y.; Fane, A. G.; Chew, J. W. Correlating the hydrodynamics of fluidized granular activated carbon (GAC) with membrane-fouling mitigation. *Journal of Membrane Science* 2016, *510*, 38–49.

[103] Abdelrasoul, A.; Doan, H.; Lohi, A.; Cheng, C.-H. Modelling development for ultrafiltration membrane fouling of heterogeneous membranes with non-uniform pore size. *Canadian Journal of Chemical Engineering* 2014, *92* (11), 1926–1938.

[104] Schindelin, J.; Rueden, C. T.; Hiner, M. C.; Eliceiri, K. W. The ImageJ ecosystem: An open platform for biomedical image analysis. *Molecular Reproduction and Development* 2015, *82* (7–8), 518–529.

[105] Ferreira, T.; Rasband, W. ImageJ User Guide IJ 1.46r https://imagej.nih.gov/ij/docs/guide/ (accessed Aug 19, 2017).

[106] Tian, L.; Chen, X. D.; Yang, Q. P.; Chen, J. C.; Shi, L.; Li, Q. Effect of calcium ions on the evolution of biofouling by Bacillus subtilis in plate heat exchangers simulating the heat pump system used with treated sewage in the 2008 Olympic Village. *Colloids and Surfaces B: Biointerfaces* 2012, *94*, 309–316.

[107] Sioutopoulos, D. C.; Karabelas, A. J. Evolution of organic gel fouling resistance in constant pressure and constant flux dead-end ultrafiltration: Differences and similarities. *Journal of Membrane Science* 2016, *511*, 265–277.

[108] Li, W.; Liu, X.; Wang, Y.-N.; Chong, T. H.; Tang, C. Y.; Fane, A. G. Analyzing the evolution of membrane fouling via a novel method based on 3D optical coherence tomography imaging. *Environmental Science & Technology* 2016, *50* (13), 6930–6939.

[109] Xu, Q.; Ye, Y.; Chen, V.; Wen, X. Evaluation of fouling formation and evolution on hollow fibre membrane: Effects of ageing and chemical exposure on biofoulant. *Water Research* 2015, *68*, 182–193.

[110] ZEISS Germany. ZEN 2 Core: Imaging Software for Connected Microscopy in Material Laboratories https://www.zeiss.com/microscopy/int/products/microscope-software/zen-2-core.html (accessed Aug 19, 2017).

[111] Egerton, R. F. *Physical Principles of Electron Microscopy: An Introduction to TEM, SEM, and AEM*, second ed.; Springer International Publishing Switzerland: Edmonton, Canada, 2016.

[112] Agron, P. A.; Busing, W. R. Magnesium dichloride hexahydrate, $MgCl_2.6H_2O$, by neutron diffraction. *Acta Crystallographica Section C* 1985, *41* (1), 8–10.

[113] Song, Y.; Shan, D.; Chen, R.; Zhang, F.; Han, E.-H. Formation mechanism of phosphate conversion film on Mg–8.8Li alloy. *Corrosion Science* 2009, *51* (1), 62–69.

[114] Hristovski, K.; Westerhoff, P.; Crittenden, J. An approach for evaluating nanomaterials for use as packed bed adsorber media: A case study of arsenate removal by titanate nanofibers. *Journal of Hazardous Materials* 2008, *156* (1), 604–611.

[115] Lide, D. R, Ed. *CRC Handbook of Chemistry and Physics*, eighty seventh ed.; Taylor and Francis: Boca Raton, FL, 2006.

APPENDIX A

COPYRIGHT PERMISSIONS

The copyright permissions for the published and co-authored manuscripts documented in this thesis are presented in Appendix A. For all manuscripts that are included in a thesis, the College of Graduate and Postdoctoral Studies (CGPS) requires a written request from the publisher, *i.e.* copyright holder (for published manuscripts) and from co-author(s) (for unpublished manuscripts).

The permission for using the published manuscript in this thesis is documented in Section A.1, and the permission for using the unpublished manuscripts are documented in Sections A.2 and A.3.

A.1 PERMISSION FOR MANUSCRIPT USED IN CHAPTER 2

The manuscript included in Chapter 2 is accepted and published online by Elsevier. Elsevier permits authors to include a portion or all of their publications in a thesis without the need to obtain permission. The photograph shown below is copied from the website of Elsevier.

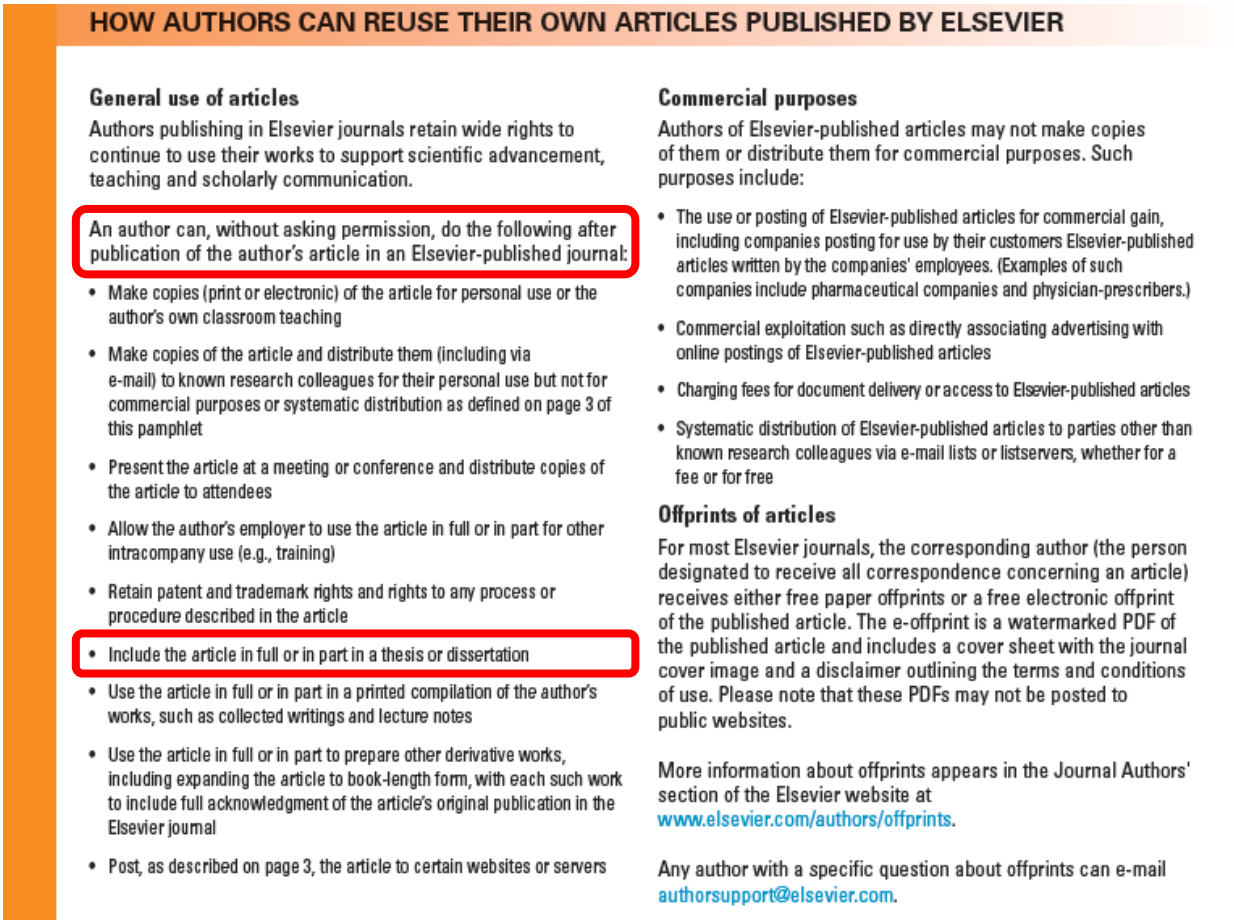

HOW AUTHORS CAN REUSE THEIR OWN ARTICLES PUBLISHED BY ELSEVIER

General use of articles

Authors publishing in Elsevier journals retain wide rights to continue to use their works to support scientific advancement, teaching and scholarly communication.

An author can, without asking permission, do the following after publication of the author's article in an Elsevier-published journal:

- Make copies (print or electronic) of the article for personal use or the author's own classroom teaching
- Make copies of the article and distribute them (including via e-mail) to known research colleagues for their personal use but not for commercial purposes or systematic distribution as defined on page 3 of this pamphlet
- Present the article at a meeting or conference and distribute copies of the article to attendees
- Allow the author's employer to use the article in full or in part for other intracompany use (e.g., training)
- Retain patent and trademark rights and rights to any process or procedure described in the article
- Include the article in full or in part in a thesis or dissertation
- Use the article in full or in part in a printed compilation of the author's works, such as collected writings and lecture notes
- Use the article in full or in part to prepare other derivative works, including expanding the article to book-length form, with each such work to include full acknowledgment of the article's original publication in the Elsevier journal
- Post, as described on page 3, the article to certain websites or servers

Commercial purposes

Authors of Elsevier-published articles may not make copies of them or distribute them for commercial purposes. Such purposes include:

- The use or posting of Elsevier-published articles for commercial gain, including companies posting for use by their customers Elsevier-published articles written by the companies' employees. (Examples of such companies include pharmaceutical companies and physician-prescribers.)
- Commercial exploitation such as directly associating advertising with online postings of Elsevier-published articles
- Charging fees for document delivery or access to Elsevier-published articles
- Systematic distribution of Elsevier-published articles to parties other than known research colleagues via e-mail lists or listservers, whether for a fee or for free

Offprints of articles

For most Elsevier journals, the corresponding author (the person designated to receive all correspondence concerning an article) receives either free paper offprints or a free electronic offprint of the published article. The e-offprint is a watermarked PDF of the published article and includes a cover sheet with the journal cover image and a disclaimer outlining the terms and conditions of use. Please note that these PDFs may not be posted to public websites.

More information about offprints appears in the Journal Authors' section of the Elsevier website at www.elsevier.com/authors/offprints.

Any author with a specific question about offprints can e-mail authorsupport@elsevier.com.

Source: https://libraryconnect.elsevier.com/sites/default/files/lcp0404.pdf

(accessed November 2, 2017)

A.2 PERMISSION FOR MANUSCRIPT USED IN CHAPTER 3

The manuscript included in Chapter 3 is unpublished; therefore, a copyright permission is requested and obtained from the co-author of the paper (Prof. Carey J. Simonson).

Copyright Permission Request Form

I am presently preparing a manuscript titled "Development of non-invasive methods to detect the onset of crystallization fouling in a liquid-to-air membrane energy exchanger" to be published as the third chapter of my Ph.D. thesis and submitted to the Department of Mechanical Engineering at the University of Saskatchewan. The author that contributes towards the finishing of this manuscript is Carey J. Simonson.

I hereby request for permission to use the contents of this manuscript in my Ph.D. thesis and all successive revisions that may be prepared at the University of Saskatchewan. Please, kindly confirm your agreement by signing below.

Yours faithfully,
Adesola O. Olufade
November 4, 2017

Permission granted by: Carey J. Simonson
Signature:
Date:

A.3 PERMISSION FOR MANUSCRIPT USED IN CHAPTER 4

The manuscript included in Chapter 4 is unpublished; therefore, a copyright permission is requested and obtained from the co-author of the paper (Prof. Carey J. Simonson).

Copyright Permission Request Form

I am presently preparing a manuscript titled "Characterization of the evolution of crystallization fouling in membranes using non-invasive and invasive methods" to be published as the fourth chapter of my Ph.D. thesis and submitted to the Department of Mechanical Engineering at the University of Saskatchewan. The author that contributes towards the finishing of this manuscript is Carey J. Simonson.

I hereby request for permission to use the contents of this manuscript in my Ph.D. thesis and all successive revisions that may be prepared at the University of Saskatchewan. Please, kindly confirm your agreement by signing below.

Yours faithfully,
Adesola O. Olufade
November 4, 2017

Permission granted by: Carey J. Simonson
Signature:
Date:

APPENDIX B

MAGNESSIUM CHLORIDE SATURATION CONCENTRATION

The saturation concentration of $MgCl_2$(aq) is formulated based on a curve-fitting of the data provided in Ref. [115], and is given by

$$C_{sol,sat} = 0.01\left(A_1 T_{sol}^3 + A_2 T_{sol}^2 + A_3 T_{sol} + A_4\right), \qquad \text{(B.1)}$$

where A_1, A_2, A_3 and A_4 are coefficients with the following values:

$A_1 = 0.0000094$,

$A_2 = -0.00109879$,

$A_3 = 0.09923483$,

$A_4 = 33.95942937$.